國立臺灣大學工學院應用力學研究所

碩士論文

Graduate Institute of Applied Mechanics

College of Engineering

National Taiwan University

Master Thesis

下肢輔助外骨骼的控制系統的研發

Development of a control system of a walking-assistive device on
lower limb

黃胤禎

Yin-Chen Huang

指導教授：張培仁 博士

施文彬 博士

Advisor: Pei-Zen Chang, Ph.D.

Wen-Pin Shih, Ph.D.

中華民國 106 年 6 月

June, 2017

國立臺灣大學碩士學位論文
口試委員會審定書

下肢輔助外骨骼的控制系統的研發

Development of a control system of a walking-assistive device on lower limb

本論文係黃胤禎君（學號：R04543004）在國立臺灣大學應用力學研究所完成之碩士學位論文，於民國 106 年 6 月 16 日承下列考試委員審查通過及口試及格，特此證明

口試委員：

張培仁 _張培仁_　施文彬 _施文彬_

（指導教授）

徐瑋勵 _徐瑋勵_

劉建豪 _劉建豪_

施博仁 _施博仁_

蔡燿全 _蔡燿全_

所　　長　王立昇 _王立昇_

誌謝

　　我的研究生涯是從大一開始的，此研究的完成首先要感謝海大的栽培。感謝領我入門的傅群超老師以及淬鍊我的林資榕老師與許進成老師。還有吳忠恕老師與沈志忠老師幫助我打好數學底子，以及海洋的各位先進：江信、智凱、宜良、霖銘、憶萱、岳修、宗益、博榕、岳庭、庠幃、穎昌、冠鈞、延償、祥倫、耀輿。

　　還記得大四推甄太晚找老師，差點找不到老師，感謝張培仁老師願意破例給我面試機會並錄取了我，並讓我借掛在黃榮山老師名下一陣子，甚至還讓我有機會可以跟從施文彬老師做研究，碩士生活同時在 433 與 107-2 度過與學習，實在非常感謝得到如此珍貴的機會，跟實驗室大夥一起度過的日子是非常難能可貴的，不論是聖誕派對還是團咪或一起吃飯與修課的日子，我都很珍惜與你們的緣分。如在應力所遇到的海洋熟悉夥伴：運承、薰儀、郁涵、政宏、博倫、亭如、博惟。修課認識的張正憲老師、趙聖德老師、翁宗賢老師、胡文聰老師、郭茂坤老師、李雨老師、丁建均老師、楊士進老師、林沛群老師、峰懷、飛鴻、立秉、瑞儀、華儒、宥君、其妙、彥霖、翊涵、冠叡、順成、芷含、久庠、欣潔、盈志、凡妮、雅君、漢門、顯佑、冠尹、大衛、華宇、偉聖、書諭、星宏、育村、治緯、俊昇。應力所職員的許小姐、邱技士、黃技士、翁技士、廖技士。北微的林博、陳小姐、安盛、泓儒與指導我使用儀器與微機電製程的各位。實驗室的明華、尚軒、紹安、恒嘉、小畢、富程、恆昇、威廷、曼地、鐸儒、彥安、元玠、柏瑄、承俊、品淳、彥廷、瑞鴻、紹傑、品蓉、淳樸、家銘、承佑、世傳、瑋杰、星宇、歆儒、善謙、泳辰、家倫、建彰、美芳、建君、仁傑、泓緯、葉廷、福臨、恩暄、宇軒、紹增、崔策、奕達、鈺傑、衛斯理父子、王煜、士倫、俊雄、昇勳、冠緯、浩祥、銘揚、一弘、孟緯、澤剛、品樺、晉毅、國安、俞齊、期宇、淳右、則翔。

　　能完成這篇論文，我要特別感謝最重要的指導教授張培仁老師、施文彬老師，以及如同指導教授般重要的劉建豪老師、胡毓忠老師、李尉彰老師、施博仁老師、徐瑋勵老師與蔡耀全老師。我最後要感謝最重要的家人，尤其是老爸老媽老哥老妹老弟，對我的支持與鼓勵，謝謝大家。

<div style="text-align: right">

學生　黃胤禎　鞠躬

</div>

i

中文摘要

　　本研究擬研發「運用腦波控制之行走輔具平台」，旨在分析人的腦波，並使人在意念階段即可控制行走輔具，來達到更加直觀的輔助行動體驗。近幾年社會有趨向高齡化的現象發生，造成復健行走或不良於行等問題日益明顯， 如何利用輔具平台來降低醫療支出，儼然成為非常重要的研究課題。且由於意外受傷或自然老化造成所謂的看護問題，會使得社會經濟出現停滯不前，競爭力下降與勞力失衡等問題。綜上所述，受傷復健、行走輔助是一門十分重要的課題。

　　欲發展一人體輔具平台以減少上述問題所造成的社會經濟負擔，本研究欲從意念控制著手，為了要達到可靠的腦波訊號量測，腦電儀必須先經過校正；故提出與真實人體皮膚性質相似的人工仿體進行腦電儀的校正工作。腦波訊號是微弱的，為了能克服雜訊的干擾，將進行動態振動測試來去除走路所造成之晃動雜訊以強化腦波訊號，並進行搜尋人體想要走路的意念特徵之演算法開發。接著為確保使用者確實想進行走路的行為以及為帶給使用者最理想的行走輔助，本研究將進行下肢生物力學的走路模型建構，分析人體走路時之運動情形。最後，結合走路意念、下肢力學模型以及馬達三種模式之自動控制，完成「運用腦波控制之行走輔具平台」。

關鍵字： 人工皮膚仿體、腦波、生物力學、輔具、外骨骼

ABSTRACT
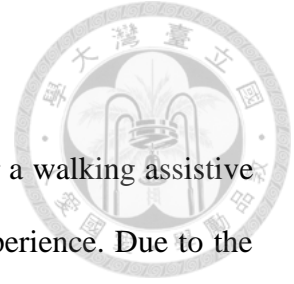
This research attempts to develop a brain-controlled system for a walking assistive device in the hope to provide more intuitive walking assistance experience. Due to the rapid growth of aging population, efficient and effective rehabilitation or walking assistance has become highly demanded. How to use assistive device to reduce medical expenses has also become a very important research issue. Care problems caused by accidental injury or natural aging can lead to stagnation in social economy, declining competitiveness, labor imbalances and so on. As above, an effective device to facilitate injury rehabilitation and walking is to be developed.

To develop an assistive device for human beings for reducing social economy loading, we intend to start from the mind control. To implement reliable brain signal measuring, EEG device must be calibrated first. We propose a calibration phantom, whose electrical and mechanical properties are similar to those of real human skin. To overcome the low signal-to-noise ratio of the EEG, a dynamic vibration test is carried out to characterize the noise caused by human walking. We also develop an algorithm to identify the intension of human walking. Based on a lower limb biomechanics model, three modes of a motor automatic control system are used to drive the walking assistant device.

Keywords： Artificial phantom, EEG, biomechanics, assistive devices, exoskeleton, control

SYMBOL TABLE

θ_a	Actual rotated angle
θ_h	Human noise
θ_c	Angle command
θ_e	Angle error
$C(z)$	Position controller
$G_{\theta V}(z)$	Mode 1 plant
k_p	Proportional gain
k_I	Integral gain
k_D	Derivative gain
T_I	Integral time constant
T_D	Derivative time constant
T	Sampling period
J , $J_{effective}$	System equivalent moment of inertia
J_{rotor}	Rotor moment of inertia
J_{gear}	Gearbox moment of inertia
$J_{coupling}$	Coupling moment of inertia
N	Gear ratio
J_{load}	Exoskeleton one leg moment of inertia
k_t	Motor torque constant

k_b	Motor back electromotive voltage constant
R	Motor winding resistance
L	Motor winding inductance
τ	Motor driven torque
i	Motor armature current
V_b	Motor back electromotive voltage
θ	Angular position in time domain
Θ	Angular position in a or z domain
$\dot{\theta},\ \omega$	Angular speed
$\ddot{\theta},\ \dot{\omega}$	Angular acceleration
v	Voltage in time domain
V	Voltage in s or z domain
ω_n	System natural frequency
ξ	System damping ratio
a	Mode 1 first level sorting constant one
b	Mode 1 first level sorting constant two
p_1	Mode 1 second level sorting constant one
p_2	Mode 1 second level sorting constant two
p_3	Mode 1 second level sorting constant three
c_1	Mode 1 third level sorting constant one
c_2	Mode 1 third level sorting constant two
$G_{\omega V}(z)$	Mode 2 plant
c	Mode 2 sorting constant one

v

d	Mode 2 sorting constant two
V_e	Voltage error
$G_{IV}(z)$	Mode 3 plant
k_u	Critical gain
T_u	Critical period
B	System equivalent damper

CONTENTS

LIST OF FIGURES

LIST OF TABLES

Chapter 1   Introduction

1.1   Background and motivation

Since the Berkeley Lower Extremity Exoskeleton (BLEEX) [1] was proposed, the exoskeleton research has become a trend around world. An exoskeleton is designed for strengthening normal human's behavior. On the other hand, helping weak human to become normal is also a way to strengthen human ability. We focus on lower limb assistance as a mission to allow people to enjoy the freedom of walking. Lower limb problem may happen on human who suffers from serious injury such as car crash or falling. It would also happen on human whose muscle degrades due to aging. The fact that people with degraded muscles are reluctant to exercise makes the lower limb problem even worse. Accordingly, exoskeleton is aimed to modify and to facilitate human locomotion in a strengthened manner.

1.2   Literature review

1.2.1   Skin phantom calibration

The challenge of EEG capturing is that brain signal is weak. How to make reliable measurement is a difficult problem. For resolving this problem, we should make a testing platform, which is repeatable for testing EEG measurement. Using human subject to test EEG recoding has problem that human would not easy to show repeatable brain signal. In addition, using large human subjects to test EEG can be costly. On the other hand, artificial skin phantom can be a reusable test platform. Phantom testing on EEG is promising [2].

1

In general, artificial skin phantoms can be categorized into two groups, the physical skin phantom and the tissue-engineered skin model. The former is designed to analogize the practical physical condition of a human skin during in vitro experiments, and the latter focuses on the biological relevance of a human skin [3]. Various phantoms of this physical type have been developed for analogizing the mechanical or electrical properties of real human skin. For instance, a gelatin-based model was developed to analogize the mechanical conditions of human skin under reentry shots [4] while a silicone-based model doped with graphite was proposed to analogize the electrical conditions of a human skin [5].

The physical skin phantoms are suitable for our design because we focus on the physical properties of a human skin for the applications of EEG testing and calibration. The goal of this research is to develop an artificial skin phantom with mechanical and electrical properties of the phantom are close to those of real human skins. The morphology of the phantom is also similar to that of a real human skin. In addition, the artificial skin phantom is prepared for testing EEG device to calibrate noise.
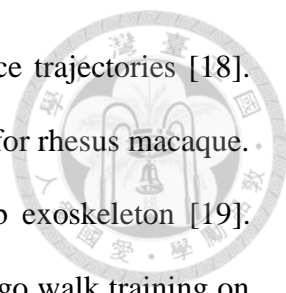
1.2.2 Overview of walking assist device

Many lower limb exoskeletons have been proposed to assist human walking. Sankai et al. develop hybrid assistive limb-5 (HAL-5) to aid human whose muscle degenerated. HAL-5 have two main control system. One is measuring EMG to know whether human want to walk or not. The other is storing walking patterns for individual user [6]. Long et al. used active disturbance rejection control strategy to track human gait trajectory on a lower limb exoskeleton made of carbon fiber for rehabilitation. They also used an extended-state observer to estimate and then suppress the disturbance by applying a control action [7]. Ollinger et al. developed an admittance control model to

2

estimate the human-assistive effect on Honda stride management assist (SMA) device. They also discussed robust stability on their control system [8].

Nagarajan et al. establish control strategy on Honda SMA device, which is based on modify the dynamic response of human limbs. By increasing the mechanical admittance, human lower limbs are more responsive to any muscle torque generated by user [9]. Liu et al. construct variable stiffness actuator, which can modulate output stiffness by changing the effective length of a bending bar. Their results show that the controller can achieve the desired performance in reference tracking [10].

Chen et al. designed a portable knee-ankle-foot robot to help stroke patients. They developed control strategies on gait phase and applied appropriate assistive force at corresponding gait phases [11]. Oh et al. propose various assistive control. Detecting walking motion phases by switching control algorithms, system would pick up appropriate control framework to handle plant [12]. Achili et al. proposed a stable adaptive observer. It can be applied to any other nonlinear system of similar dynamics [13]. Giovacchini et al. presented a lightweight carbon fiber active orthosis, whose weight is 4.2 kg, to assist hip rotation. User could walk with this orthosis without feeling hindered [14]. Asbeck et al. proposed a soft exosuit for portable hip assistance. Their soft design would not restrict hip ab- and adduction direction or rotation about leg axis [15]. Ouyang et al. developed a power unit for exoskeleton robot, a compact hydraulic power unit powered by an internal combustion engine (CHPU). The CHPU can provide 1.5 kW hydraulic power and 100 W electric power, which can meet the requirement for exoskeleton robots [16]. Selinger et al. designed myoelectric control, which can adapt the timing and magnitude of electrical power generation for an energy harvesting exoskeleton [17]. Hussain et al. proposed an adaptive seamless assist-as-needed (AAN) control, which is for the robotic gait training. They found that

3

the robotic orthosis is capable of guiding human limbs on reference trajectories [18]. Vouga et al. presented a lower-limb exoskeleton controlled by brain for rhesus macaque. They demonstrated the feasibility of a brain-controlled lower-limb exoskeleton [19]. Zhang et al. presented a rehabilitation exoskeleton, which can undergo walk training on patient's individual walking habit. Their exoskeleton can evaluate patient's rehabilitation status in real time by providing necessary torques on the dyskinetic leg [20]. Jin et al. used adaptive fuzzy sliding mode control on a lower limb exoskeleton. Their wearer feels more comfortable to move the swing leg [21, 22]. Long et al. proposed passive mode and active mode, respectively, on a lower limb rehabilitation exoskeleton for unilateral lower limb movement disorders patient. Exoskeleton in the former case would copy healthy gait trajectory. The latter would modify healthy gait trajectory and help to strengthen the unhealthy limb [23]. Zhu et al. presented an unidirectional variable stiffness hydraulic actuator for loading carrying knee exoskeleton. Their results show that the system has good performance on stiffness regulation and joint torque control [24].

We want to develop a compact walking-assistive device on lower limb. Our exoskeleton should let user feel comfortable as receiving the help form the power unit.

4

Chapter 2   Design of artificial skin phantom

2.1   Real human skin properties

Normal human skin would contain three layers, stratum corneum, epidermis, and dermis. We design our skin phantom by only considering the stratum corneum and epidermis. The reason why we skip dermis is as following. First, the electrical resistivity of the stratum corneum and the epidermis is larger than that of the dermis [25]. Therefore, we can skip the dermis due to its small impedance. Secondly, there are many cells in dermis such as nerves and bloods cells [26]. There is no need to implement EEG calibration circuit with these cells to eliminate static noise. Therefore, we would design a two-layer structure, which includes stratum corneum and epidermis.

We are curious about human sweating situation on EEG calibration. Human sweating may affect the resistivity on EEG electrode. Then we consider sweat pores and sweat ducts structure within our phantom design.

2.2   Selection of Phantom Material

We choose SU-8 photoresist and gelatin as materials for making stratum corneum and epidermis, respectively. Our desired stratum corneum thickness should be 10~40 μm [25]. Our desired epidermis thickness should be 70~100 μm [27]. The resistivity of human skin is a function of frequency, which is 10^7 Ωm in the frequency range from 1Hz to 1kHz and 10^4 Ωm at the frequnecy of 1MHz [25]. The modulus of elasticity of human skin has a larger variation measured by different researchers and a reasonable range is from 100 kPa to 20 MPa [28~30]. The density of the sweat pores is in the range from 200 pics/cm^2 to 700 pics/cm^2, and the diameter of the sweat pores fall in the range from 20 to 50 μm. Values of both density and diameter of sweat pores vary for different

5

parts of human bodies [31]. We choose to simulate palm sweat pore density due to its density is highlest than other parts.

Stratum comeum (SU-8 photoresist)
- 10 to 40 µm
- Seen as insulator

Sweat pores and ducts
(Fabricated by patterning technique)
- 20 to 50 µm
- 200 - 700/cm^2

Epidermis (Gelatin)
- 70 to 100 µm
- 10^7 Ω·m under low f
- 10^4 Ω·m under high f
- Reasonable Young's modulus
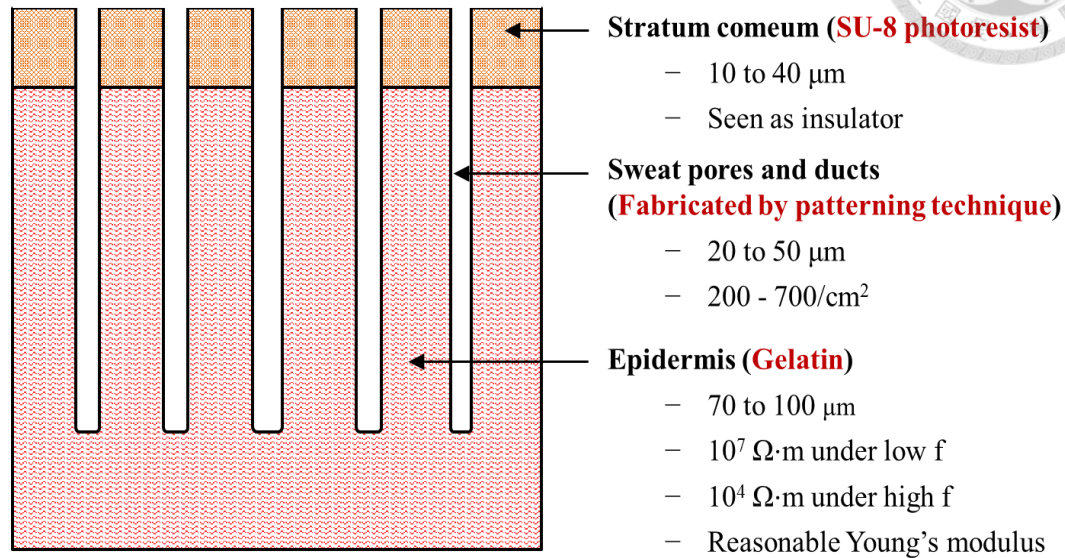
Fig. 2-1　Skin phantom design structure.

SU-8 works as insulators [32] in terms of electrical properties, which is same as stratum corneum properties. The SU-8 film can be fabricated from 10 to 40µm [33], which is analogous to stratum corneum thickness. Due to its photoresist property, the SU-8 can make tiny sweat pore and dense pores density with micromachining technology.

Gelatin is a natural material extracted from skin, tendons, ligaments, or bones of animals. Gelatin powder can be dissolved in hot water to form a film. The hydrogen bonds inside the gelatin solution would make the solidified film elastic, which can analogize the mechanical properties of human skin. In addition, the gelatin electrical properties can be changed by mixing conductive elements such as acetic acid, graphene, or lithium ion, into gelatin solution [34~36]. Hence, gelatin can provide different electrical properties for simulating different human skin conditions.

Chapter 3   Phantom fabrication
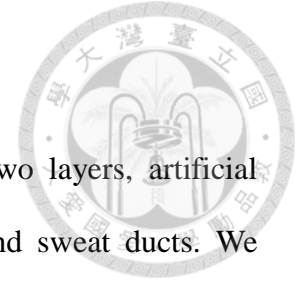
Our skin phantom imitates human skin and thus contains two layers, artificial stratum and artificial epidermis. It also possesses sweat pores and sweat ducts. We choose SU-8 2025 negative type photoresist and gelatin as the phantom materials. These two materials are appropriate to simulate real human skin and are easy to make sweat pores and sweat ducts with microfabrication and laser ablation.

We divide the whole process into three main steps. The first is to make artificial stratum corneum with sweat pores by using micromachining techniques. The second step is to make artificial epidermis with cross-linked gelatin. At this step, we combine stratum corneum and epidermis together. Finally, we will use laser ablation technique to make sweat ducts.

3.1   Artificial stratum corneum with sweat pores

Microfabrication process includes many steps such as electron beam evaporation, spin coating, photolithography and wet etching. Some steps, especially spin coating, require good adhesion of negative photoresist on the substrate. In this work, polished 4-inch oxidized silicon wafer is used as the substrate.

The wafer-cleaning process is depicted in Fig. 3-1. First, the silicon wafer is immersed in isopropyl alcohol (IPA) under sonication to remove macro particles. Then the silicon wafer is rinsed with de-ionized (DI) water. We use heated solution of sulfuric acid and hydrogen peroxide to remove possible polymer residues and then rinse the wafer with DI water again. The wafer is then dried by using air gun, followed by baking at 120ºC for 3 minutes.
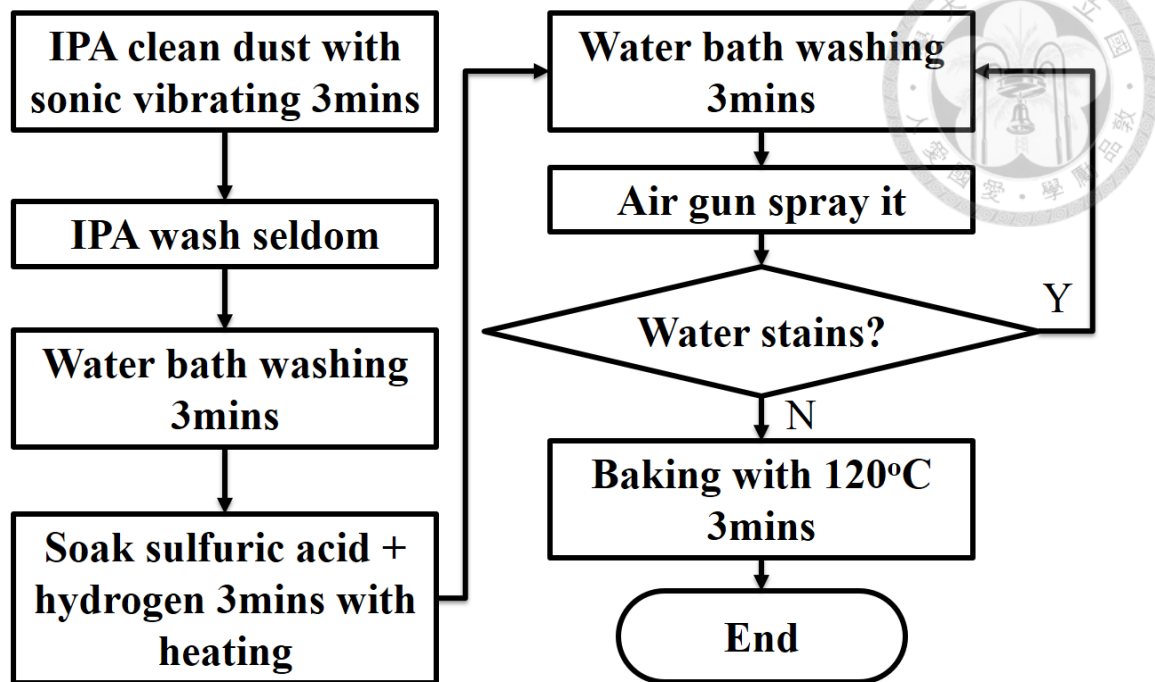
Fig. 3-1   Flow chart for cleaning wafer.

The process to fabricate artificial stratum corneum is depicted in Figs. 3-2 and 3-3, respectively. Firstly, a chromium adhesion layer of 10 nm in thickness is deposited on the cleaned substrate by using electron beam evaporation. Then, the copper sacrificial layer of 100 nm in thickness is deposited by using the electron beam evaporation. A layer of SU-8 2025 is spin-coated on the copper layer. The spin rate is firstly kept at 500 rpm for 250 sec and then ramped up to 3000 rpm that is maintained for 300 sec. The obtained SU-8 thickness is 25 μm. It is baked at 65°C for 6 minutes and then at 95°C for 12 minutes later.

(a) Deposition   (b) Spin coating   (c) Exposure

(d) Wet etching   (e) Deposition

■ Substrate   ▨ Copper   ■ SU-8 2025   □ Ferric Chloride
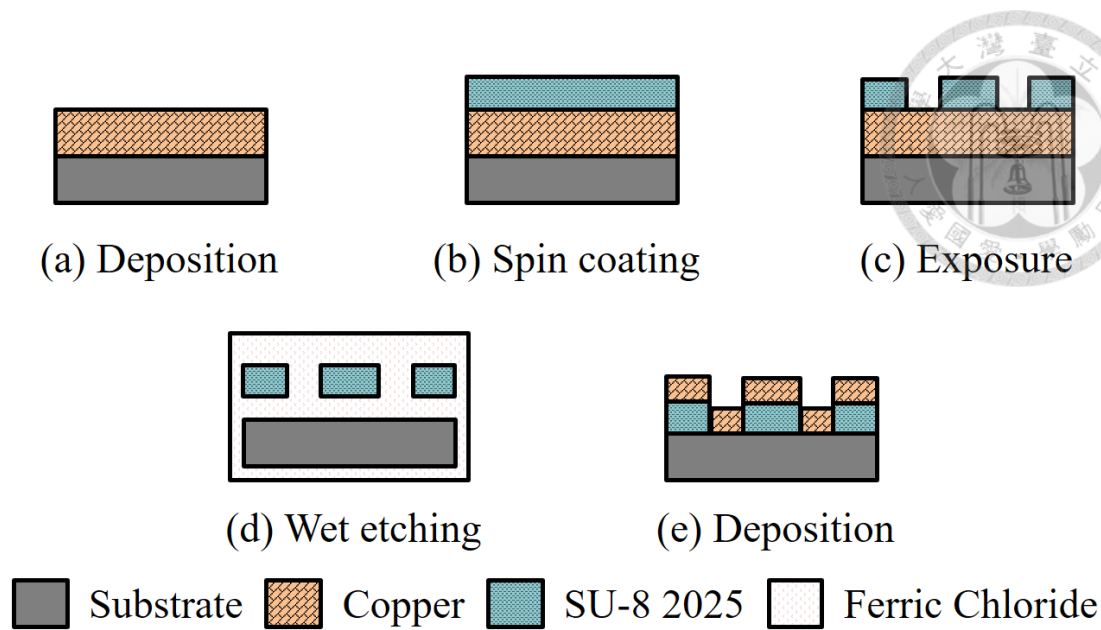
Fig. 3-2　Schematic of SU-8 thin film.
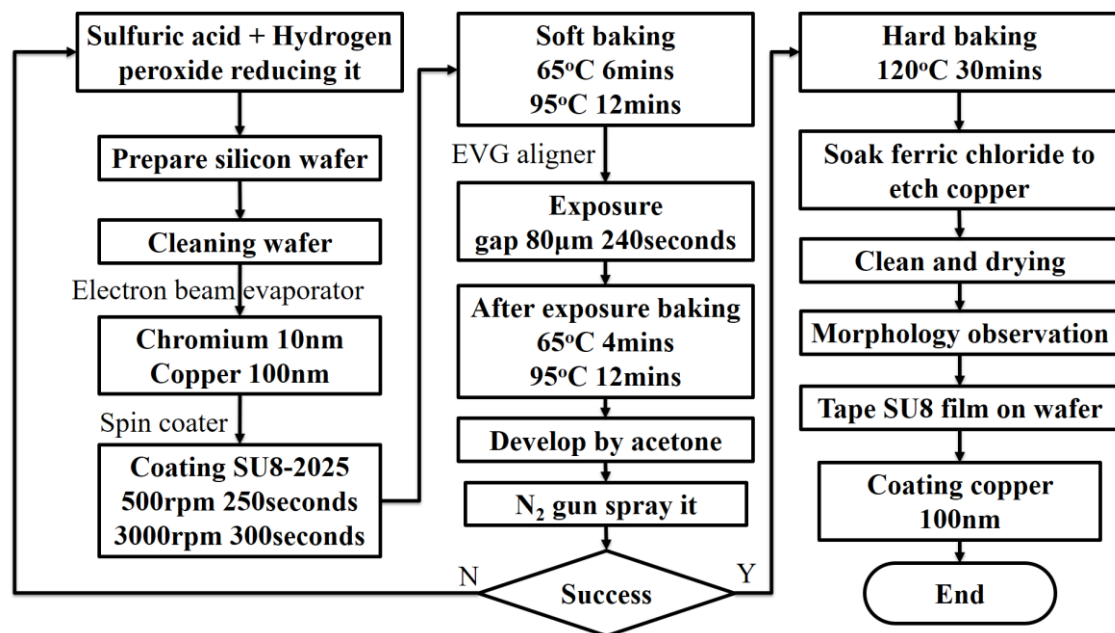
Fig. 3-3　Flow chart for SU-8 thin film.

Following the datasheet of SU-8 [33], soft baking should be conducted after spin coating. As shown in Fig. 3-4, the soft bake was conducted on hot plate at 65°C for 6 minutes and then 95°C for 12 minutes. Then, the wafer is cooled down at room temperature.

9

Fig. 3-4　Soft baking process.

Photolithography process is the main step to pattern sweat pore onto SU-8 2025. We use the mask shown in Fig. 3-5. The mask has opaque dot patterns, which define the sweat pores, as the portion (a) in figure. The dot diameter and density is 20 μm and 620 dots/cm^2, respectively. The mask is separated into 4 parts by two 1 mm-wide straight lines, as the portion (b) in figure. This design allows etchant remove the sacrificial layer quickly [37].
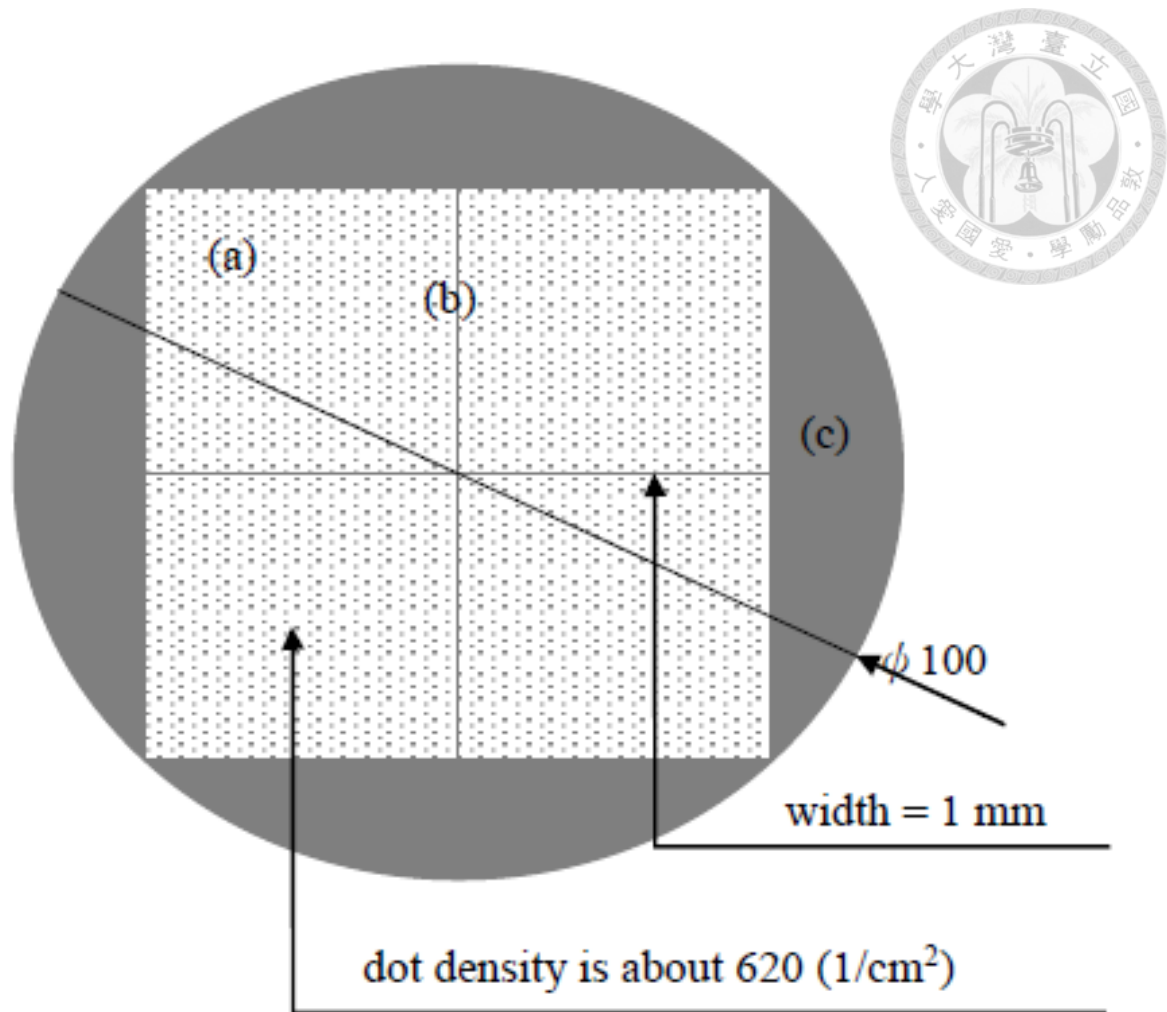
Fig. 3-5　Sweat pore design on 4-inch wafer.

We use EVG 620 top-side mask aligner to exposure SU-8. We choose soft contact with 80 μm gap between the mask and wafer. The exposure energy and time are 10.7 mW/cm^2 and 240 seconds, respectively. The post-exposure bake is conducted at 65°C for 4 minutes and then 95°C 12 minutes. It eliminates the standing wave effect of the exposure light.

We choose acetone as the developer. The under-exposed SU-8 (60 sec) causes poor adhesion of the film on the substrate. Therefore, wrinkles are observed after development in acetone, as shown in Fig. 3-6. The wrinkled SU-8 is not suitable for making the skin phantom. It can be removed by etching out the underneath copper using the solution of sulfuric acid and hydrogen peroxide.

11

Fig. 3-6   SU-8 fail thin film.

For longer exposure time such as 120 sec, the SU-8 thin film becomes very brittle after development. Drying the film using air gun would break the film into many fragments. Therefore, we exploit the high volatility of acetone and allow the wafer to dry out spontaneously after development. After development, the hard baking was conducted in oven at 120°C for 30 minutes. The fabricated SU-8 film with sweat pores is shown in Fig. 3-7.
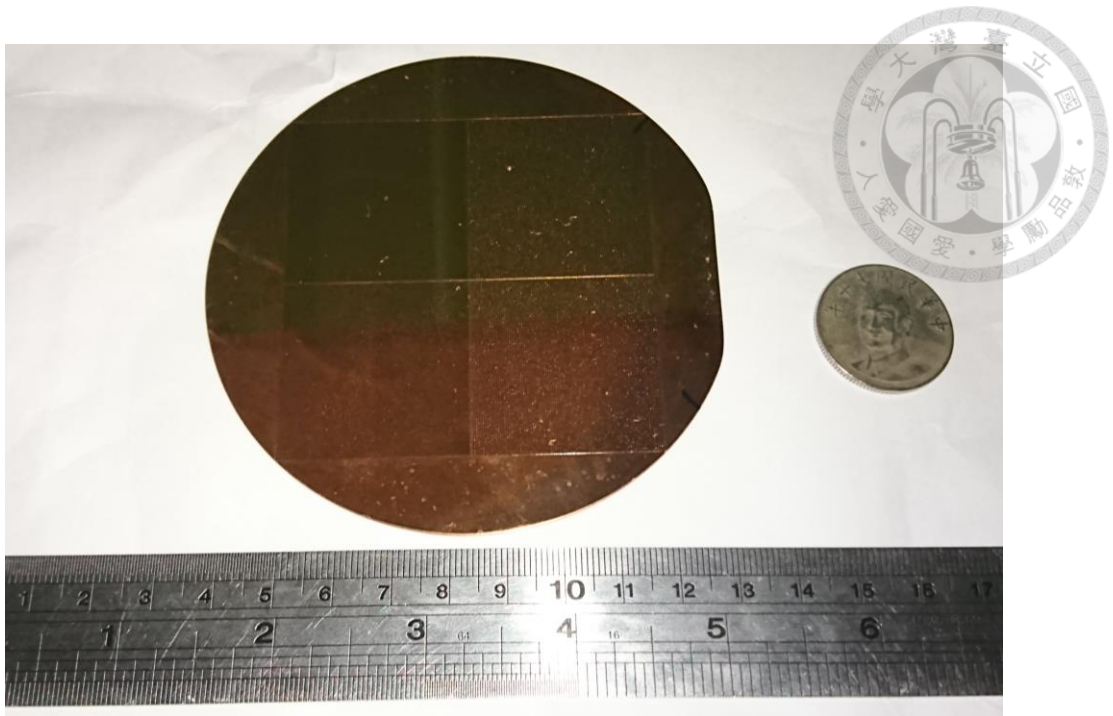
Fig. 3-7　Fabricated SU-8 films with sweat pores.
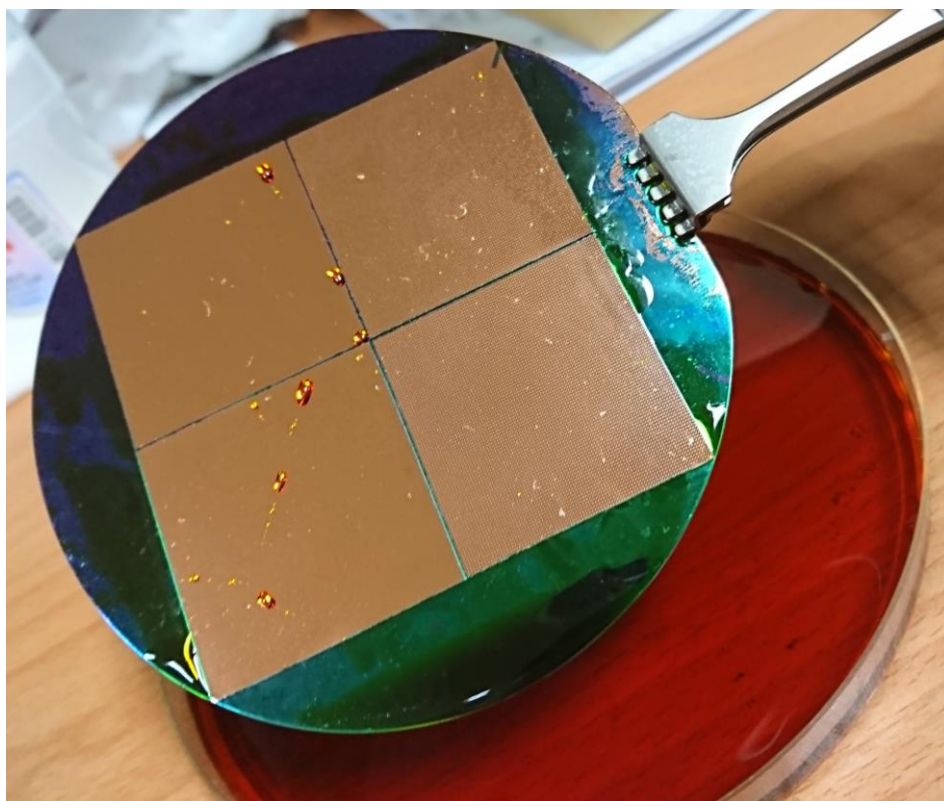
Fig. 3-8　Wet etching process to remove the copper sacrificial layer.

Fig. 3-9　Fabricated artificial stratum corneum.

Ferric chloride solution is used to remove the copper sacrificial layer, as shown in Fig. 3-8. The fabricated artificial stratum corneum is shown in Fig. 3-9. We also make an SU-8 thin film without sweat pores for comparison. The flow chart is shown in Fig. 3-10.
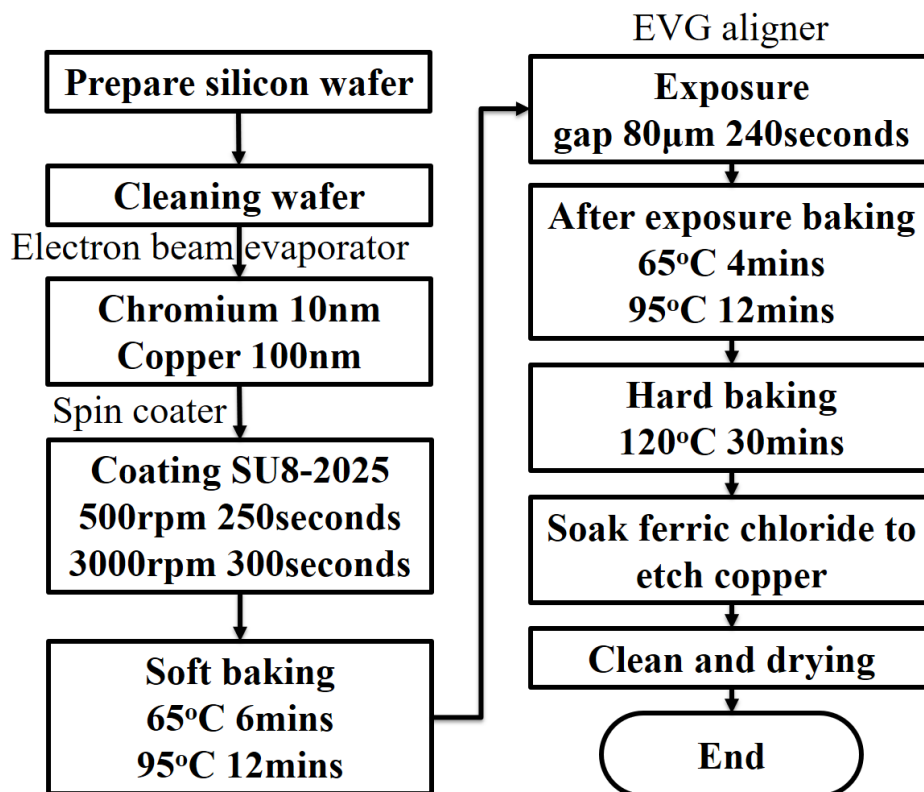
Fig. 3-10 Flow chart for fabricated SU-8 thin film without sweat pores.

14

3.2　Combination of stratum corneum and epidermis

```
┌─────────────────────┐        ┌─────────────────────┐
│ Weigh 0.75g gelatin │        │ Add glutaraldehyde  │
│      powder         │        │ 50μl for crosslinking│
└─────────────────────┘        └─────────────────────┘
           │                              │
┌─────────────────────┐        ┌─────────────────────┐
│ Weigh appropriate   │        │     Stir evenly     │
│  sodium chloride    │        └─────────────────────┘
└─────────────────────┘                   │
           │                   ┌─────────────────────┐
┌─────────────────────┐        │ Pouring solution into│
│ Put them together   │        │ appropriate container│
│   into beaker       │        └─────────────────────┘
└─────────────────────┘                   │
           │                   ┌─────────────────────┐
┌─────────────────────┐        │ Placing copper-     │
│ Pouring 20ml DI     │        │ covered SU8 film    │
│     water           │        └─────────────────────┘
└─────────────────────┘                   │
  Hot plate│              ┌─────────────────────┐
┌─────────────────────┐        │ Waiting for gelatin │
│ Heating 70°C        │        │  solidification     │
│ Stir evenly         │        └─────────────────────┘
└─────────────────────┘                   │
           │                   ┌─────────────────────┐
┌─────────────────────┐        │        End          │
│ Cool down by water  │        └─────────────────────┘
│     bath            │
└─────────────────────┘
```
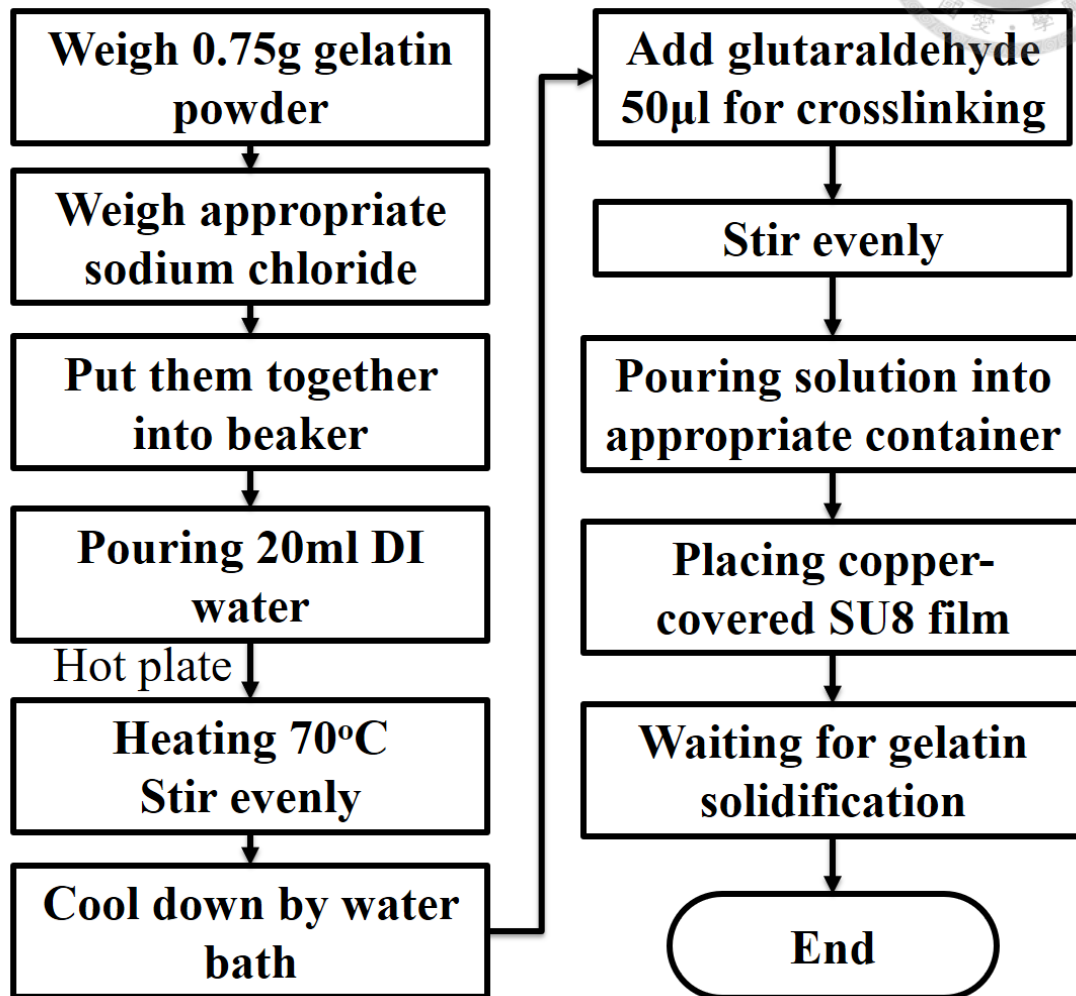
Fig. 3-11 Flow chart for gelatin film.

The process to assemble artificial stratum corneum and epidermis is shown in Fig. 3-11. First, we make gelatin-based epidermis. In process, we mix gelatin powder with sodium chloride to make the salt content of 0 %, 0.5 % and 1.4 %, respectively of total weight. The corresponding salt weight is 0, 0.1, and 0.3 g, respectively. Modulating salt content is to simulate different human skin conditions. The mixed powers are dissolved in 20 mL DI water at 70°C, as shown in Fig. 3-12.

15

Fig. 3-12 Heat and stir gelatin solution.

After cooling down the mixture, we gently add 50 μL glutaraldehyde by using pipet. Glutaraldehyde can help gelatin particle to form crosslinks. It should be noted that glutaraldehyde has cytotoxicity [38]. We then stir the solution until the glutaraldehyde is well mixed. To mold gelatin into a film as artificial epidermis, we pour the solution into an appropriate container. The container height should be perfectly horizontal so that our

16

epidermis can have uniform thickness. We then put copper-coated stratum corneum onto the gelatin and let the gelatin solution naturally dry out.

We found that higher salt content makes softer artificial epidermis. The reason is that salt particle would obstruct gelatin particle from crosslinking. We can apply UV light exposure to enhance gelatin crosslinking for increasing the Young's modulus of the artificial epidermis.

3.3 Fabricating artificial sweat ducts
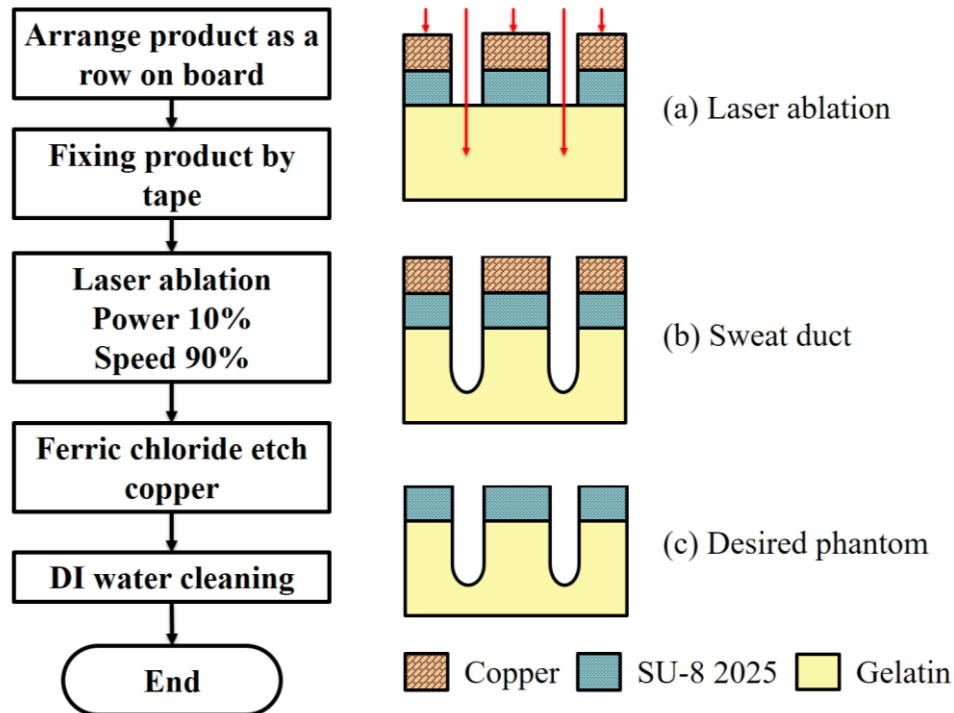
Fig. 3-13 Flow chart and schematic for completing phantom.

The process of make sweat ducts in the phantom is shown in Fig. 3-13. We use M-360 laser cutting machine as our laser ablation platform. The laser power of M-360 is set at 10%. Because there is copper coating on the stratum corneum to absorb laser power, only the gelatin exposed by the SU-8 opening will be ablated. After making the sweat ducts, we remove the top copper mask by using chloride solution.

Chapter 4   Phantom properties test

4.1   Morphology tests

The morphology test is to verify the phantom thickness and the sweat pore size. To imitate normal human skin, the phantom thickness should be close to 100 μm. The diameter of the fabricated sweat pores should be close to 20 μm.

We use the μ229 thin film measurement instrument, from Sylvac, to determine the phantom thickness, as shown in Fig. 4-1. The results are listed in Table 4-1. Their standard deviations, with the salt content form low to high, are 14, 7 and 14.4 μm, respectively.

Fig. 4-1   Phantom thickness measurement.

Table 4-1 Averaged film thickness.

Phantom salt content (%)	Average thickness (μm)
0	142
0.5	137
1.4	153

We use optical microscopy (OM) to characterize the density and diameter of the fabricated sweat pores. We use low magnification to check the sweat array, as shown in Fig. 4-2. The center-to-center distance adjacent sweat pores is 400 μm. There are 25 sweat pores in the field size of 4 mm^2. Therefore, the obtained sweat pore density is 625 pores/cm^2, close to that on human palm. Under large magnification of the microscope, it is confirmed that the diameter of the fabricated sweat pores is 20 μm. Table 4-2 shows all morphology measuring result and real human skin properties for comparison.
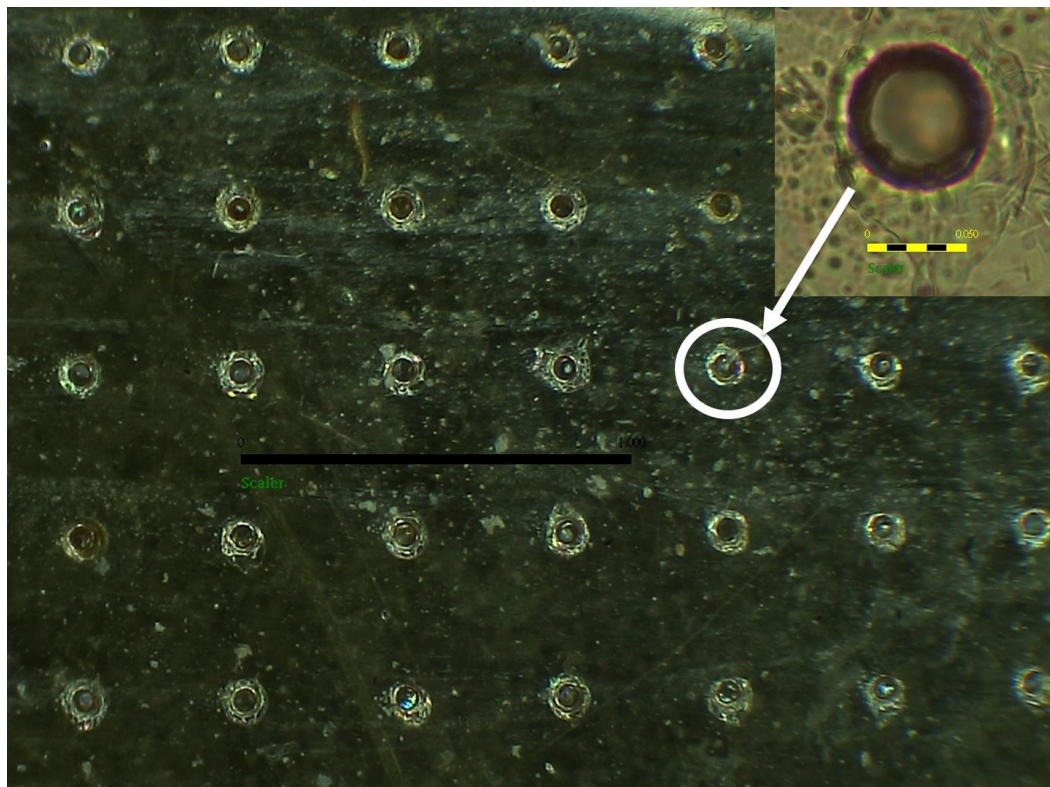
Fig. 4-2　OM sweat pores observation. The inset shows a single sweat pore.

19

Table 4-2 Morphology testing result.

Measurement	Specification [25,31]	Result
Thickness	80~140μm	Average 142μm for no salt
Sweat pore density	200~700 pics/cm^2	Around 625 pics/cm^2
Sweat pore diameter	20~50μm	Around 20μm

4.2   Mechanical tests

We use compression test to measure modulus of elasticity. We choose Kyowa full-scale 50 N load cell to characterize the fabricated phantom. We use precision stage, SHOT204, and load cell to implement stress and strain relation, as shown in Fig. 4-3. In the test, the load cell compresses the phantom at 100 μm/s. The contact radius of the load cell on the phantom is 2 mm. The size of the phantom under test is 10 mm x 5 mm.

The obtained modulus of elasticity of the phantoms of different salt contents is shown in Table 4-3. These results are in good agreement with the test on real human skin [28~30].
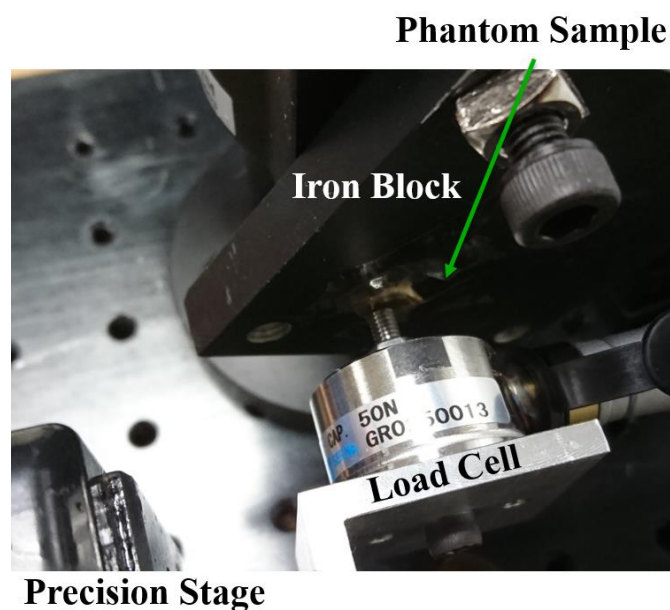
Fig. 4-3   Compression test on phantom.

20

Table 4-3 Modulus of elasticity.

Phantom salt content (%)	Modulus of elasticity (MPa)
0	1.608
0.5	1.135
1.4	1.661

4.3   Electrical tests

The objective to design this phantom is to calibrate static noise from EEG measuring device. This static noise is mainly coming from electrical circuit. To eliminate this electrical noise, we should measure impedance of our phantom. By this measurement, we can constructed impedance circuit with phantom at EEG noise calibration.
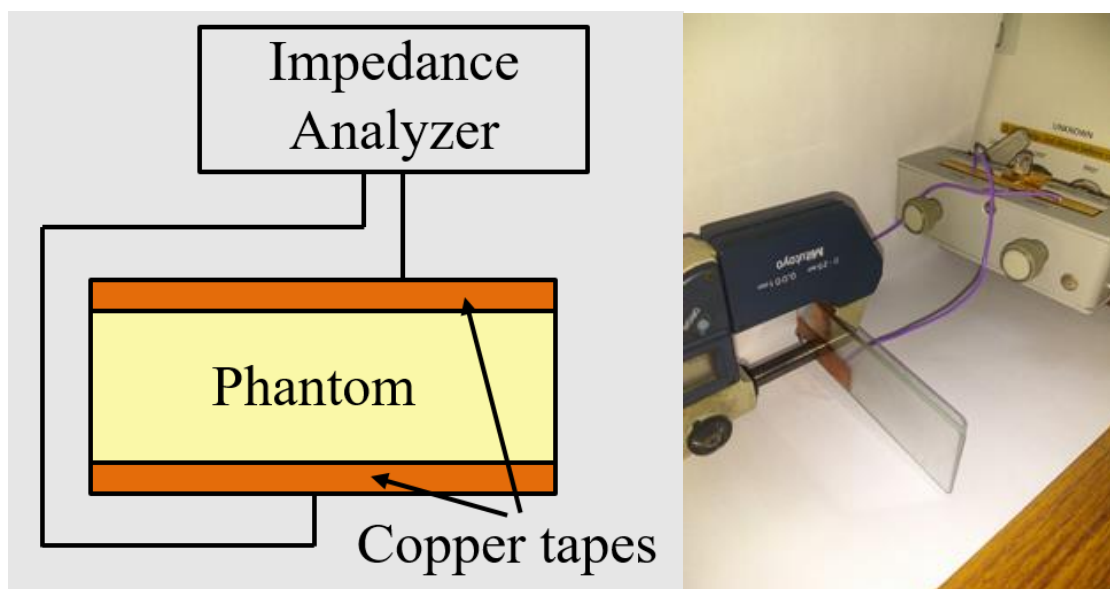
Fig. 4-4   Impedance measurement on phantom.

We test the impedance by using Keysight E4990A, as shown in Fig. 4-4. We found that copper foil tape causes lower contact resistance than copper tape does. The measured impedance is shown in Fig. 4-5. We use resistivity, instead of impedance, to discuss the material properties so that the dimension effect can be ignored. The obtained resistivity is up to 10^7 Ωm at 1~10 kHz and drops to 10^4 Ωm at 1 MHz. By comparing to the literature [25], we can conclude that our skin phantom fit to human skin impedance property at dry condition.
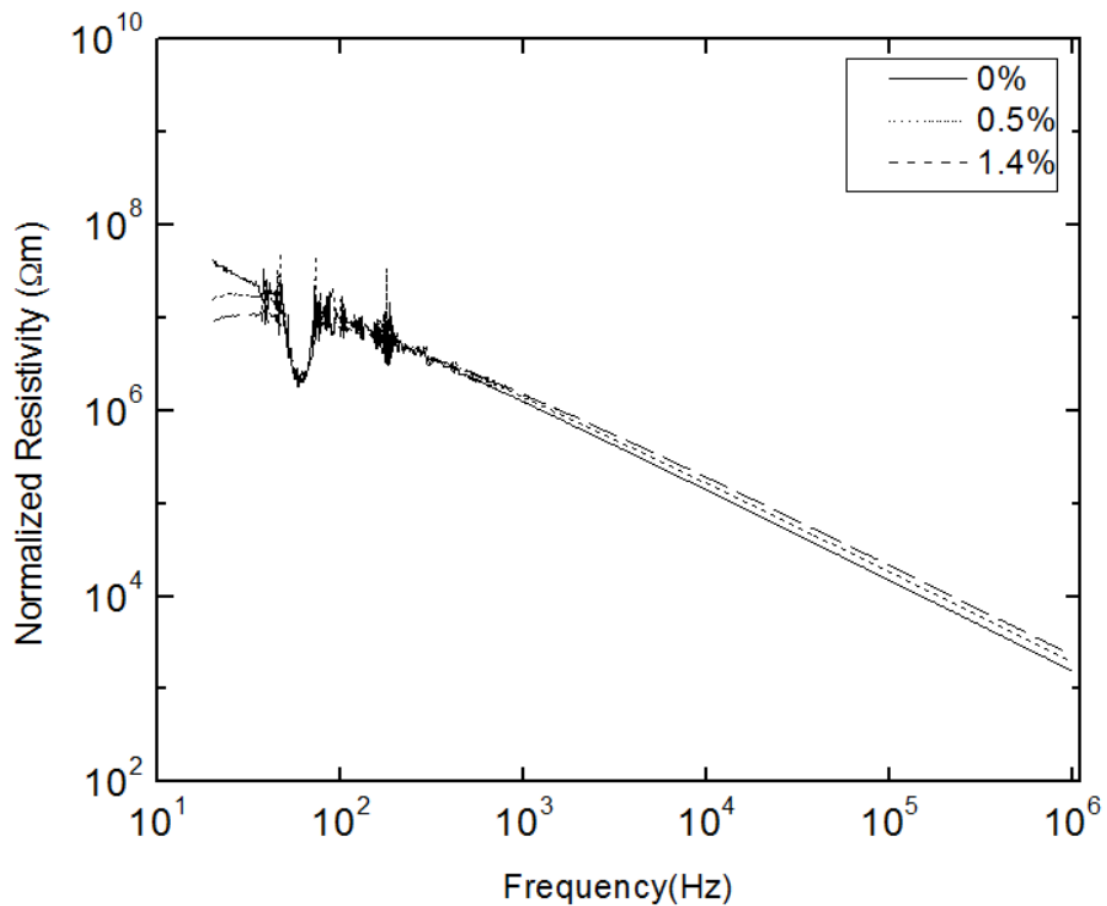
Fig. 4-5   Impedance mesurment on dry condition.

We then soak our samples with phosphate-buffered saline (PBS) to simulate wet condition. To make sure test sample water content, we measure wet sample. The measured impedance in wet condition is shown in Fig. 4-6. The wet phantoms are more conductive than real human skin. This is because the human skin has cell membranes

22

that impede water flow and thus the electron transports. Based on equivalent circuit on epidermis [39, 40], we fit our skin phantom dry condition result with parallel resistance and capacitor circuit model with ADS circuit design software. The results are shown in Table 4-4.
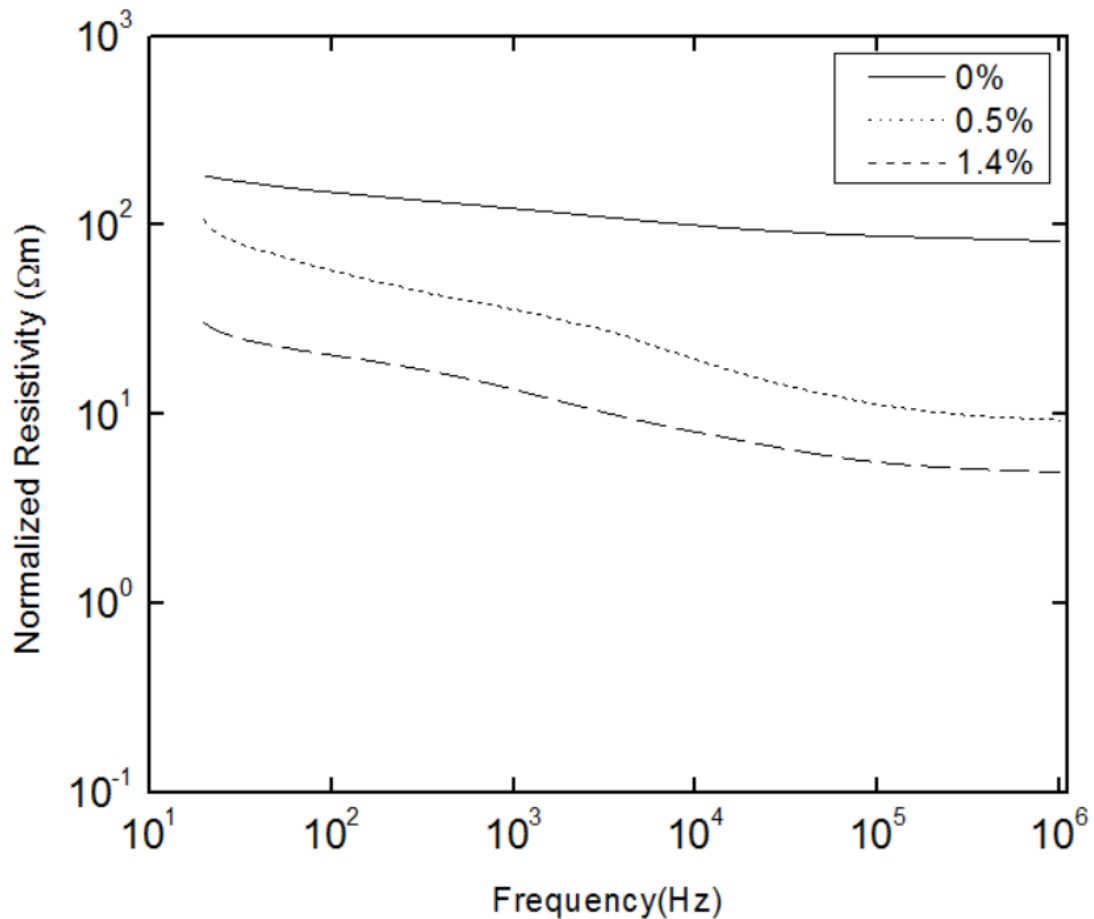
Fig. 4-6   Impedance measurement in wet condition.

Table 4-4   Electrical circuit model fitting dry measuring result.

Salt content (%)	Resistance (MΩ)	Capacitor (pF)
0	97.65	50.8
0.5	31.27	40.5
1.4	17.98	34.5

23

Chapter 5　Structure and control theory

In this chapter, we would introduce structure of our assistive device. Our structure is designed to cover human body from hip to knee. After introducing mechanism, we will introduce the electronics of our system such as motor and its related circuitry. Then we will construct control model based on ESCON module. Different control modes will be compared.
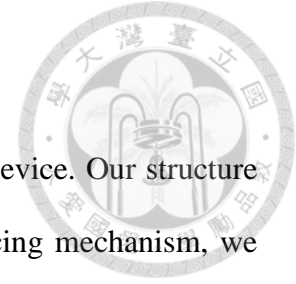
5.1　Exoskeleton mechanism

Our exoskeleton is designed to have two degrees of freedom (DOF) on hip joint, which is the rotation of flexion/extension and adduction/abduction, respectively. We remove one DOF to let pelvic joint perform self-rotation about thigh. This DOF is not the most important part on assist walking, so we simplify this DOF on mechanism design.

For exoskeleton motor axis and back plate axis, there are two axes intersecting at the center of human hip joint. Motor is driving the rotation of flexion/extension. This design would let human motion more comfortable. They would feel exoskeleton like extension of their body. Based on gait cycle, we define human hip and knee angle rotating range. Then we design a cylinder sliding mechanism, which can fix human leg moving range properly.

Fig. 5-1 shows the side view of exoskeleton for right leg and left leg, respectively. Heng-Chia Hsu previously used vector loop method to find actual size of each mechanism part [41]. The black vectors and gray vectors would construct two different vector loops. With these two loops and human joint information within gait cycle, they use kinematics equation to determine all dimensions.

24
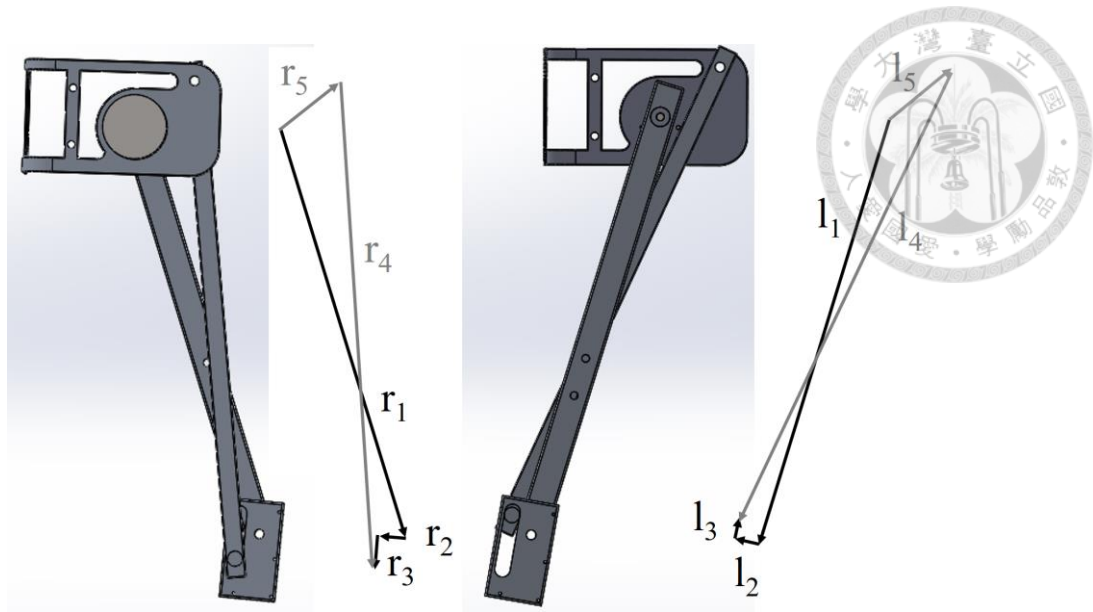
Fig. 5-1   Side view of device: two legs with vector loop.

In Fig. 5-1, the cylinder in the slot moves up and down during walking. We measure the bearing connecting the motor axis and the pin in the slot, as shown in Fig. 5-2. Although the knee can not reach 60° flexion of the human knee joint limit, 50° moving range is sufficient for walk assistance. This fixed cylinder can restrict human thigh rotation. We define this limitation as fall prevention function in our exoskeleton mechanism.
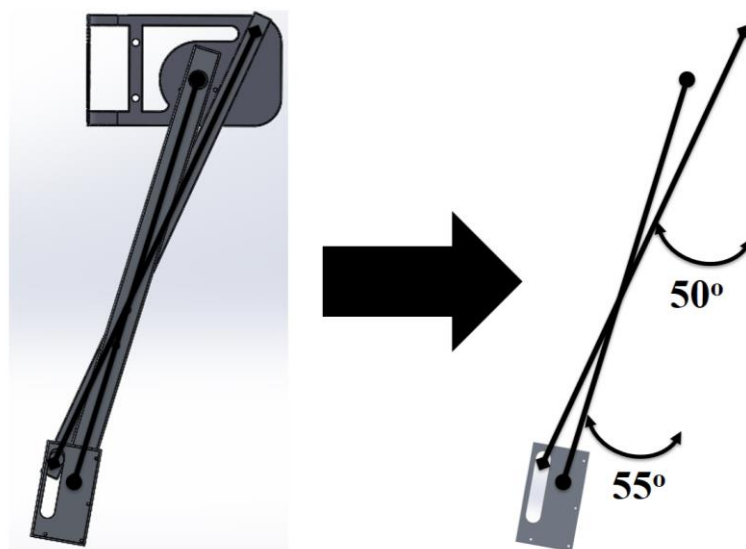
Fig. 5-2   Fall prevention on mechanism moving diagram.

25
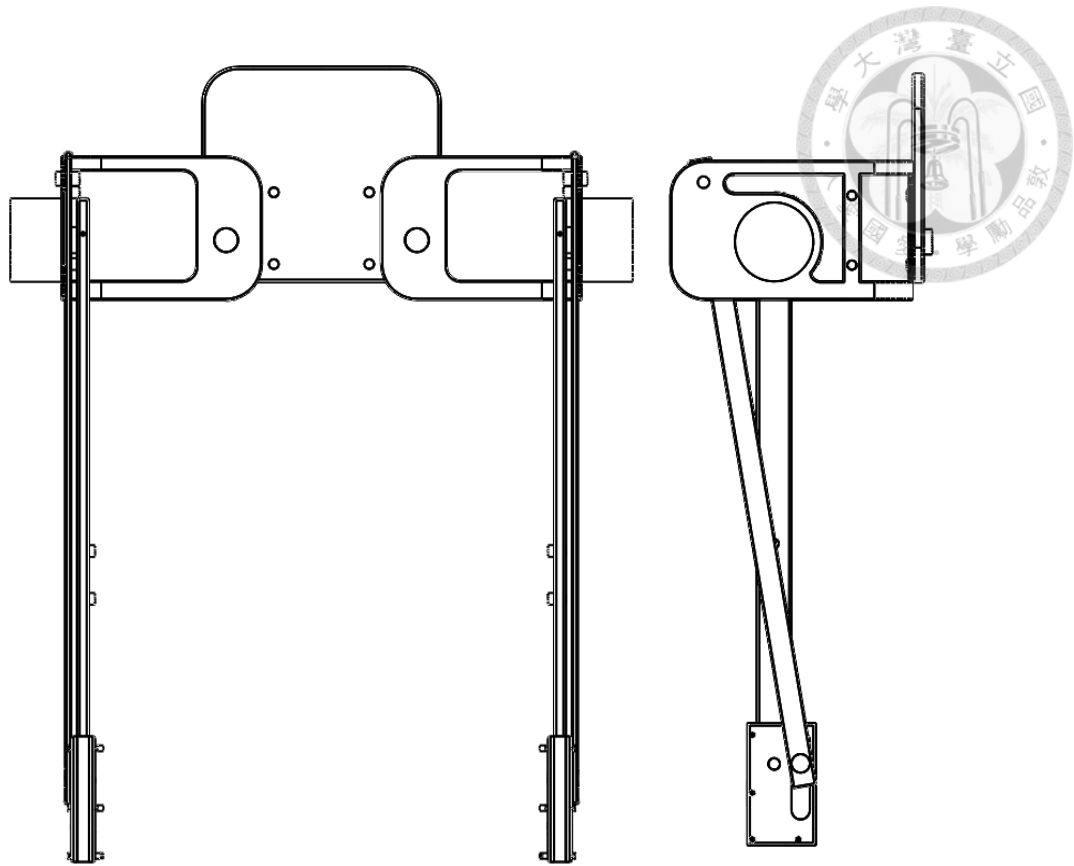
Fig. 5-3   Exoskeleton mechanism. The left inlet is the front view, and the right is the

side view.

The whole exoskeleton mechanism is shown in Fig. 5-3. The weight is 2.3 kg without motor. For user's comfort, we use touch fasteners sticky to fix human knee upper and lower parts. Then we use travel package fixing belt to tie human shoulder and waist with the exoskeleton, to avoid total mechanism fall down from human body.

5.2   Circuit and servo amplifier

5.2.1   Motor chosen

We choose brushless DC motor (BLDC motor) to drive the exoskeleton. BLDC motor is generally used for high positioning accuracy. Its brushless feature can avoid sparks and brush friction loss so that BLDC motor can save energy and pursuit high

efficiency.

The basic concept of BLDC motor is that replacing the carbon brush with electronics in a motor. With the electronics and control for each switch, this non-mechanical contact system can change the direction as carbon brush does. BLDC motor has the following advantages. First, it runs quietly and is suitable in some quiet places such as hospitals and schools. Second, BLDC does not generate any spark and thus can use in some flammable and explosive places. Third, BLDC is more durable because it uses controller instead of the carbon brush.

BLDC motor has three phases and a Hall position sensor so the motor commutation accurate rotor position detection accuracy is not affected by the motor speed. It does not require additional rotor position detection circuit hardware. We install the gearbox to ensure that motor have ability to supply sufficient torque to assist the human body.

5.2.2   Servo amplifier

To drive BLDC motor, we need to know rotor position by Hall sensors. We then need to input correct three phases driving signal and enough power to drive the motor. We choose the BLDC motor, MAXON EC 60 flat [42], with gearbox as our system power unit. Its corresponding servo amplifier is ESCON module 50/5 [42].

To setup the motor, we should prescribe the motor phase. Our motor have already inserted encoder; we should set encoder information in ESCON studio to make sure that the encoder is working. To drive the motor by using ESCON, the digital I/O and analog input can be set as a function to enable or disable motor driving, to accept PWM duty from controller, and to determine the motor driving direction. For capturing data, ESCON can set analog output pin to read motor speed and current data.

ESCON can operate three different modes to control motor. In Mode 1, ESCON

27

acts as a voltage amplifier. ESCON can do IXR compensation in mode 1 and 2. IXR compensation is to stabilize voltage during motor rotation. Parameters of IXR compensation can be chosen as static or dynamic in mode 1. In mode 2, motor speed is controlled in closed loop using feedback from the encoder. In mode 3, motor current is controlled in a closed loop, which is useful for torque control. We compare these three modes control effect for our exoskeleton system. We then choose the proper mode to control the exoskeleton.

5.2.3　Controller circuit

We separate our electrical system into three sub-systems: action system, calibration system; stop system and graphical user interface. The action system is for moving exoskeleton. The calibration system is for calibrating the zero position. The stop system is to help user stop exoskeleton in emergency. Graphical user interface is for user to see actuation angles and calibration state.

When we need to move the exoskeleton, we design a button for user to control. The button delivers signal of "walking". Then National Instrument (NI) Myrio [43] captures the feedback signal of the encoder and calculates PID algorithm. The signal that after PID calculation will pass from NI Myrio to ESCON 50/5 motor driver as PWM signal. Finally, ESCON 50/5 would control MAXON EC60 flat motor to achieve our expected gait cycle. Fig. 5-4 illustrates this process.
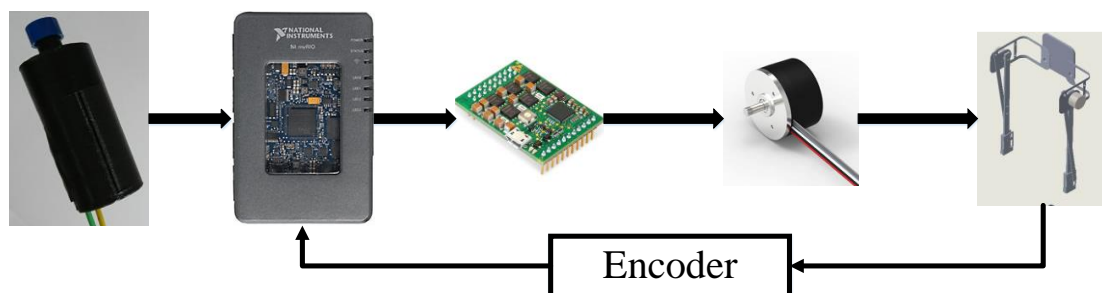
Fig. 5-4　Action system structure.

We also place hall sensor at point B in Fig. 5-5. This component can make program to identify zero rotation, which can provide information to help user stand. This is important as if we lose the real zero position, the encoder signal would be not correct. Producing a wrong signal to the algorithm will make a wrong output signal.
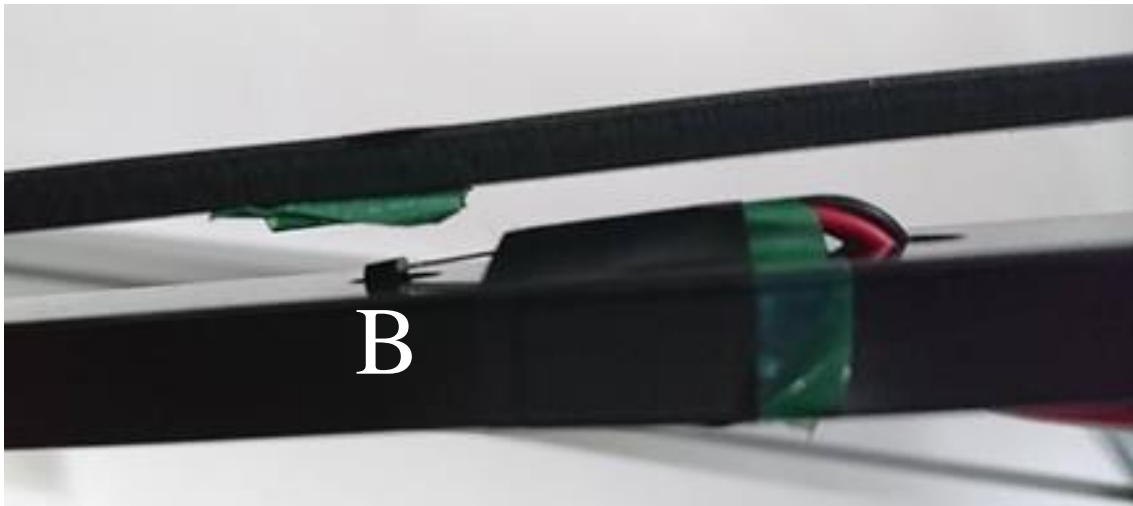
Fig. 5-5   Calibration system.

To avoid motor rotation over the range of gait cycle, we make two limit switches on the sliding boundary, as shown in Fig. 5-6. When stance state occurs, the cylinder will hit limit switch. Then the controller will command the driver to stop motor to prevent user from injury.

Fig. 5-6   Stop system.

29
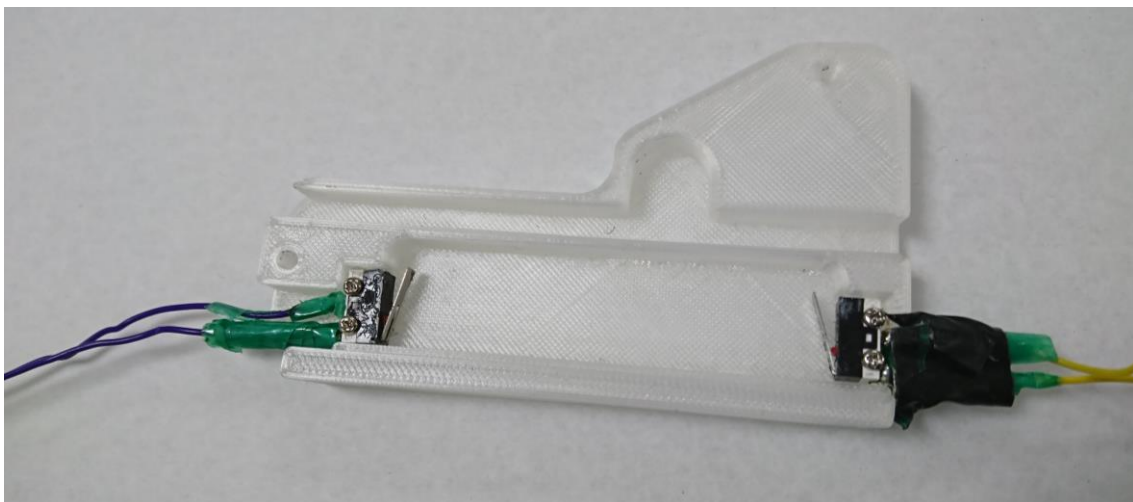
The graphic user interface is shown in Fig. 5-7. With this interface, user can know the motion of the exoskeleton. The information comes from the right and left leg encoder signal. This signal is calculated with gear ratio for correspond to actual angle rotation. There are two lights placed at the upper left side of the interface. One is to tell user whether the limit switch has been triggered. An on light indicates that the corresponding leg reaches the stance state. The other light is to tell user whether the exoskeleton has been calibrated or not. This bulb lighting is a result from Hall sensor signal. When the user is standing, which is zero calibration state as we defined, the Hall sensor is triggered by strong magnetic flux. This is signal for reaching zero state, and the bulb is turned on. There is one button placed at upper right side. By pushing this button, the system will stop for emergency. Motor driving would be disabled for safety consideration. Then program would start to collect data before this button is pushed again. The data such as encoder signal, motor current and motor speed can help us analyze the system failure.

Fig. 5-7   Graphical user interface.

30

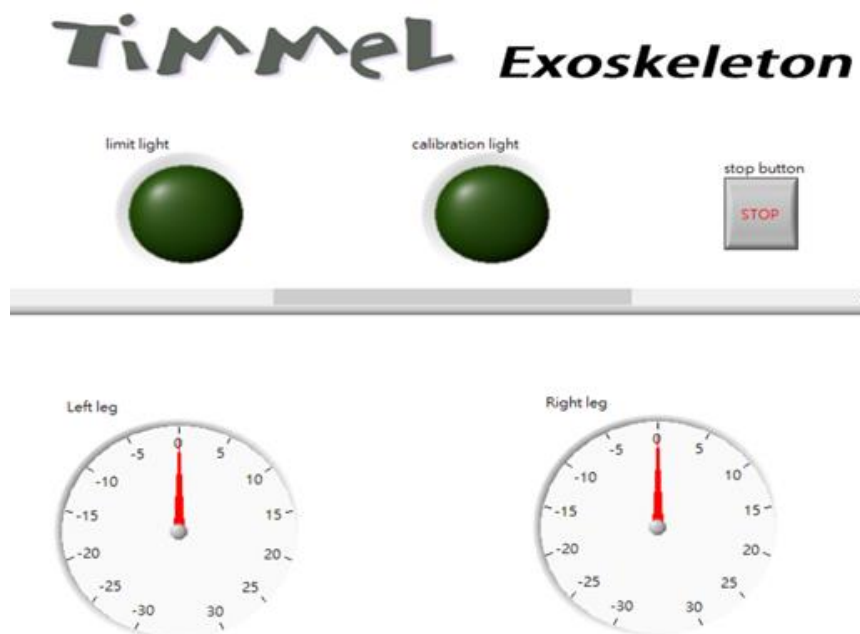## 5.3 Motor position control theory

We consider Shannon sampling theorem for continuous-to-discrete transformation. Our sampling rate is well designed as 1000 Hz. We consider control diagram for angle position as below. The output of this system is the actual rotation angle θ_a, which is disturbed by human noise, θ_h. The control block diagram is shown in Fig. 5-8. By combining human normal gait data as control command, θ_c, with left summing point, we can get the angle error, θ_e, as a controller input.
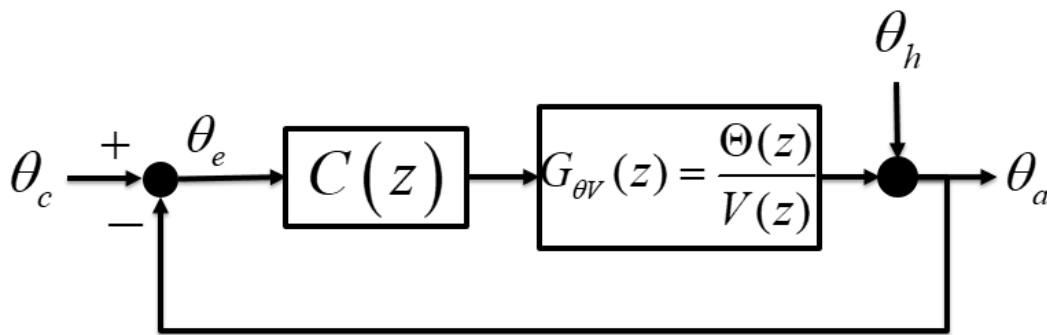
Fig. 5-8   Mode 1 control block diagram.

We use PID controller in this work. This controller has good stability and high reliability. Its structure is easy to implement and understood. A PID controller includes three data feedback processing system, which is proportional, integral and derivative control. Proportional control can enlarge or shrink error to track input signal, which can enlarge system over shoot. Integral control can gradually stack error, which can eliminate steady state error. However, integral control is too slow to handle instant system variation. In contrast, derivative control can estimate error variation in advance. However, derivative control can be easily disturbed by high frequency noise. This disadvantage should be compensated by integral control.

The angle position control model would be easier to have two extra poles than common control system. To stabilize these two characteristics, we use two zeros from

31

PID to handle this problem. The PID controller structure yields the following two equations:

$$C(z) = \frac{V}{\theta_e} = \frac{\left(k_P + k_I T + \frac{k_D}{T}\right)z^2 - \left(k_P + 2\frac{k_D}{T}\right)z + \frac{k_D}{T}}{z^2 - z}$$ (1)

$$C(z) = \frac{V}{\theta_e} = \frac{k_P\left(1 + \frac{T}{T_I} + \frac{T_D}{T}\right)z^2 - k_P\left(1 + 2\frac{T_D}{T}\right)z + \frac{k_p T_D}{T}}{z^2 - z}$$ (2)

Here k_p, k_I and k_D are three gains correspond to each control model. In digital control field, it often uses T_I and T_D to design k_I and k_D with sampling period T. After deriving controller structure, we can derive plant structure. For rotation system, the mass is the moment of inertia. We estimate the system effective moment of inertia as

$$J_{effective} = J_{rotor} + J_{gear} + \frac{1}{N^2}\left(J_{coupling} + J_{load}\right)$$ (3)

We estimated J_{load} with our exoskeleton moving bar and knee part combination on Solid Works software. After obtaining $J_{effective}$, we put a table to sort any known parameters. Some information is from MAXON datasheet [42].

Table 5-1 Known parameters.

Parameter (unit)	Value
k_t (Nm/A)	5.340e-2
k_b (V*s/rad)	5.340e-2
R (Ω)	0.307
L (V*s/A)	1.880e-4
$J_{effective}$ (kg*m^2)	1.303e-4
T (s)	1.000e-3

32

Although the BLDC is a three-phase motor, which means it is composed of three inductance and resistance pairs. We only consider one phase in our motor electrical differential equation because the current would only pass through one phase during motor rotation. After exchanging phases, the current would pass through other inductance and resistance pairs.
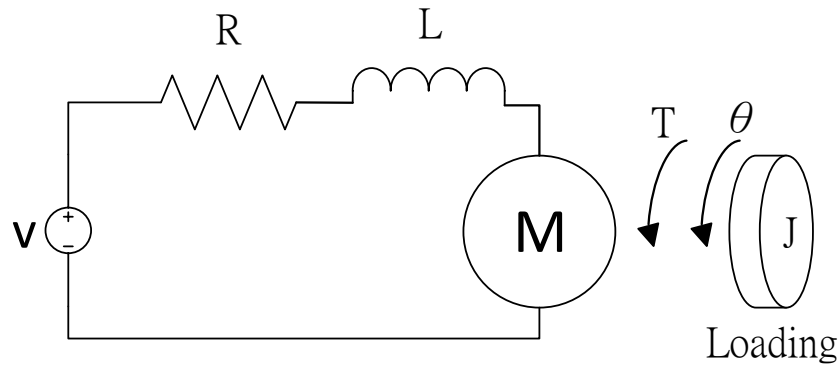
Fig. 5-9   Schematic of system plant.

The transfer function of angle position over voltage for one of phases for BLDC with equivalent circuit shown in Fig. 5-9. Assume that rotor, loading have effective mass moment of inertia J. The motor characteristic are two relations: $\tau = k_t i$ and $V_b = k_b \dot{\theta}$, where k_t is motor torque constant and i is armature current. The other relation shows that back electromotive voltage V_b composition. It is the product of motor speed constant k_b and angular rate $\dot{\theta}$. The free body diagram for rotor in Fig. 5-9 yields

$$J\ddot{\theta} = k_t i \tag{4}$$

where $\ddot{\theta}$ is the angular acceleration, which is considering human noise influence. Analysis of the electric, including the back electromotive voltage $V_b = k_b \dot{\theta}$, leads to

33

$$v = L\frac{di}{dt} + Ri + k_b\dot{\theta} \tag{5}$$

By applying current, $i = \frac{J}{k_t}\frac{d^2\theta}{dt^2}$, into equation (5) gives

$$v = \frac{JL}{k_t}\frac{d^3\theta}{dt^3} + \frac{JR}{k_t}\frac{d^2\theta}{dt^2} + k_b\frac{d\theta}{dt} \tag{6}$$

The Laplace transform of equation (6) is

$$V(s) = \left(\frac{JL}{k_t}s^3 + \frac{JR}{k_t}s^2 + k_b s\right)\Theta(s) \tag{7}$$

which can be rewritten as

$$\frac{k_t}{JL}V(s) = \left(s^3 + \frac{R}{L}s^2 + \frac{k_b k_t}{JL}s\right)\Theta(s) \tag{8}$$

In control theory, standard mass damper spring system (MCK system) has second order differential equation. Its transfer function standard form is

$$\frac{\omega_n^2}{s^2 + 2\xi\omega_n s + \omega_n^2} \tag{9}$$

In this standard form, there are two characteristic properties, which are natural frequency (ω_n) and damping ratio (ξ). These two properties play an important role in system response. Although variable of equation (8) has third order term, these properties still can be used because of our system has constants for common MCK system problem. In our case, these two properties can be written as:

$$\omega_n = \sqrt{\frac{k_b k_t}{JL}} \tag{10}$$

$$\xi = \frac{R}{2\omega_n L} = \frac{R}{2}\sqrt{\frac{J}{k_b k_t L}} \tag{11}$$

Value of natural frequency and damping ratio in our system is 341rad/s and 2.393.

34

Sorting equation (8) with two characteristic properties, the transfer function for the motor is readily found to be

$$G_{\theta V}(s) = \frac{\Theta(s)}{V(s)} = \frac{1}{k_b} \frac{\omega_n^2}{s^3 + 2\xi\omega_n s^2 + \omega_n^2 s} \tag{12}$$

This transfer function is used in continuous domain. Unless we use operational amplifier circuit to control exoskeleton power unit directly, we should consider transfer function in discrete domain for digital controller such as computer or micro controller. To discretize the transfer function for angle position over voltage, we must understand zero order hold, which is a common way in digital-to-analog conversion. Zero order hold is a mathematical model of the practical signal reconstruction. That is, it describes the effect of converting a discrete-time signal to a continuous-time signal by holding each sample value for one sample interval. To get this mathematical model, we constructed two-step functions. One is normal step function, and the other is step function with one sample interval delay. After subtracting these two functions, we get a constant within one sample interval, which means discrete signal in pre sample interval is held to present sample interval. As a result,

$$\frac{1 - e^{-sT}}{s} = \frac{1}{s} - \frac{e^{-sT}}{s} \tag{13}$$

To obtain discrete transfer function, which is so called z domain transfer function, we should consider new system dynamics (NSD), which is the multiplication of zero order hold (equation (13)) and continuous transfer function (equation (12)).

$$NSD\left(\frac{\Theta(s)}{V(s)}\right) = \frac{1 - e^{-sT}}{k_b} \frac{\omega_n^2}{s^4 + 2\xi\omega_n s^3 + \omega_n^2 s^2} \tag{14}$$

There is a useful transformation matching table between time domain, s domain, which is continuous frequency domain, and z domain, which is digital domain [44]. To use this

35

table for quickly getting transformation equation representation on z domain, we must do partial fraction expansion with continuous transfer function as

$$NSD\left(\frac{\Theta(s)}{V(s)}\right) = \frac{1-e^{-sT}}{k_b}\left(\frac{1}{s^2} - \frac{2\xi}{\omega_n s} + \frac{\frac{2\xi}{\omega_n}s + 4\xi^2 - 1}{s^2 + 2\xi\omega_n s + \omega_n^2}\right) \quad (15)$$

The first and second terms can be directly transformed from s domain into z domain by applying transformation table. For the last term, it is difficult to transform because our parameter on the damping ratio is over one, which implies an over-damping system. There is only under-damping system for table, and its component has $\sqrt{1-\xi^2}$ term. If we directly substitute s domain last term into transform pair, it would show imaginary term in our transfer function, which is difficult to programmable of our transfer function for control root locus design. Fortunately, this useful table also can match time domain transform to z domain transformation pair. Therefore, we can do inverse transform with last term of partial fraction expansion on s domain transfer function.

$$L^{-1}\left(\frac{\frac{2\xi}{\omega_n}s + 4\xi^2 - 1}{s^2 + 2\xi\omega_n s + \omega_n^2}\right) = ae^{\left(\sqrt{\xi^2-1}-\xi\right)\omega_n t} + be^{-\left(\sqrt{\xi^2-1}+\xi\right)\omega_n t} \quad (16)$$

where

$$a = \frac{2\xi^2 + 2\xi\sqrt{\xi^2-1}-1}{2\sqrt{\xi^2-1}\omega_n} \quad (17)$$

$$b = -\frac{2\xi^2 - 2\xi\sqrt{\xi^2-1}-1}{2\sqrt{\xi^2-1}\omega_n} \quad (18)$$

Transferring the above time domain equation into z domain gives

$$Z\left[NSD\left(\frac{\Theta(z)}{V(z)}\right)\right] = \frac{z-1}{k_b z}\left(\frac{Tz}{(z-1)^2} - \frac{2\xi}{\omega_n}\frac{z}{z-1} + \frac{az}{z-e^{\left(\sqrt{\xi^2-1}-\xi\right)\omega_n T}} + \frac{bz}{z-e^{-\left(\sqrt{\xi^2-1}+\xi\right)\omega_n T}}\right) \quad (19)$$

Therefore, we found that the final simplified reduction of fractions to a common

36

denominator form of denominator has three poles. We define these three poles as

$$p_1 = 1 \tag{20}$$

$$p_2 = e^{\left(\sqrt{\xi^2-1}-\xi\right)\omega_n T} \tag{21}$$

$$p_3 = e^{-\left(\sqrt{\xi^2-1}+\xi\right)\omega_n T} \tag{22}$$

After reduction of fractions to a common denominator, we can get

$$G_{\theta V}(z) = \frac{1}{k_b \omega_n}\left(\frac{1}{(z-p_1)(z-p_2)(z-p_3)}\right) * \begin{bmatrix} \omega_n T(z-p_2)(z-p_3) - 2\xi(z-p_1)(z-p_2)(z-p_3) \\ +a(z-p_1)^2\omega_n(z-p_3) + b(z-p_1)^2\omega_n(z-p_2) \end{bmatrix} \tag{23}$$

Then we can sort each z polynomial term on numerator. After sorting with simple linear combination, we can get the discrete transfer function on rotated angle over voltage, $G_{\theta V}$, as

$$G_{\theta V}(z) = \frac{1}{k_b \omega_n}\left(\frac{1}{z^3 - (p_1+p_2+p_3)z^2 + (e^{-2\xi\omega_n T}+p_2+p_3)z - e^{-2\xi\omega_n T}}\right) *$$
$$\begin{bmatrix} (\omega_n T - 2\xi + b\omega_n p_3 + a\omega_n p_2)z^2 \\ +(2\xi(p_1 - e^{-2\xi\omega_n T}) + c_1 p_3 + c_2 p_2)z \\ +e^{-2\xi\omega_n T}(\omega_n T + 2\xi) - a\omega_n p_3 - b\omega_n p_2 \end{bmatrix} \tag{24}$$

where

$$c_1 = \frac{2\xi^2 - \omega_n T\sqrt{\xi^2-1} - 1}{\sqrt{\xi^2-1}} \tag{25}$$

$$c_2 = -\frac{2\xi^2 + \omega_n T\sqrt{\xi^2-1} - 1}{\sqrt{\xi^2-1}} \tag{26}$$

We have already known all coefficients for above equation by parametric Table 5-1 as previous described. Substituting these known parameters into equation (24) yields

$$G_{\theta V}(z) = \frac{\Theta(z)}{V(z)} = \frac{3.742e-5z^2 + 1.234e-4z + 2.490e-5}{z^3 - 2.422z^2 + 1.864z - 0.442} \tag{27}$$

37

5.4   Position and speed control theory

In ESCON module mode 2, ESCON would perform speed control inside. It uses PI controller because the speed plant would decrease one critical stability pole at s equal zero. Then we do not need to use the extra zero from derivative control to cancel this probability causing unstable term.
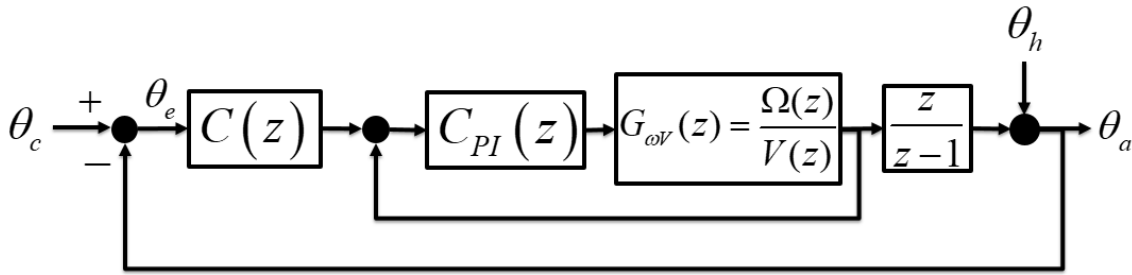

Fig. 5-10 Mode 2 control block diagram.

The motor characteristics are $\tau = k_t i$ and $V_b = k_b \omega$. The free body diagram of rotor in Fig. 5-9 yields

$$J\dot{\omega} = k_t i \tag{28}$$

where $\dot{\omega}$ is angular acceleration. Analysis of the electric, including the back electromotive voltage, $V_b = k_b \omega$, gives

$$v = L\frac{di}{dt} + Ri + k_b \omega \tag{29}$$

Applying current as $i = \dfrac{J}{k_t}\dfrac{d\omega}{dt}$ leads to

$$v = \frac{JL}{k_t}\frac{d^2\omega}{dt^2} + \frac{JR}{k_t}\frac{d\omega}{dt} + k_b \omega \tag{30}$$

The Laplace transform of equation (30) is

38

$$V(s) = \left(\frac{JL}{k_t} s^2 + \frac{JR}{k_t} s + k_b \right) \Omega(s) \tag{31}$$

It can then be rewritten as

$$\frac{k_t}{JL} V(s) = \left(s^2 + \frac{R}{L} s + \frac{k_b k_t}{JL} \right) \Omega(s) \tag{32}$$

The transfer function for the motor is readily found to be

$$G_{\omega V}(s) = \frac{\Omega(s)}{V(s)} = \frac{1}{k_b} \frac{\omega_n^2}{s^2 + 2\xi\omega_n s + \omega_n^2} \tag{33}$$

The discrete transfer function, which is so called z domain transfer function, is the multiplication of zero order hold (equation (13)) and continuous transfer function (equation (33)):

$$NSD\left(\frac{\Omega(s)}{V(s)} \right) = \frac{1 - e^{-sT}}{k_b} \frac{\omega_n^2}{s^3 + 2\xi\omega_n s^2 + \omega_n^2 s} \tag{34}$$

There is a useful transformation matching table between time domain, s domain, which is continuous frequency domain, and z domain, which is digital domain [44]. To use this table for quickly getting transformation equation representation on z domain, we must do partial fraction expansion with continuous transfer function as

$$\frac{1 - e^{-sT}}{k_b} \left(\frac{1}{s} - \frac{s + 2\xi\omega_n}{s^2 + 2\xi\omega_n s + \omega_n^2} \right) \tag{35}$$

We conducted inverse transform with last term of partial fraction expansion on s domain transfer function and obtain

$$L^{-1}\left(-\frac{s + 2\xi\omega_n}{s^2 + 2\xi\omega_n s + \omega_n^2} \right) = \frac{-\left(\sqrt{\xi^2 - 1} + \xi \right) e^{\left(\sqrt{\xi^2 - 1} - \xi \right)\omega_n t} + \left(\xi - \sqrt{\xi^2 - 1} \right) e^{-\left(\sqrt{\xi^2 - 1} + \xi \right)\omega_n t}}{2\sqrt{\xi^2 - 1}} \tag{36}$$

where

39

$$c = \frac{-\sqrt{\xi^2 - 1} - \xi}{2\sqrt{\xi^2 - 1}} \tag{37}$$

$$d = \frac{\xi - \sqrt{\xi^2 - 1}}{2\sqrt{\xi^2 - 1}} \tag{38}$$

And

$$c + d = -1 \tag{39}$$

Therefore,

$$Z\left[NSD\left(\frac{\Omega(z)}{V(z)} \right) \right] = \frac{z-1}{k_b z}\left(\frac{z}{z-1} + \frac{cz}{z - e^{\left(\sqrt{\xi^2-1}-\xi\right)\omega_n T}} + \frac{dz}{z - e^{-\left(\sqrt{\xi^2-1}+\xi\right)\omega_n T}} \right) \tag{40}$$

After reduction of fractions to a common denominator, we can get the form as:

$$\frac{1}{k_b}\left(\frac{\left(z - e^{\left(\sqrt{\xi^2-1}-\xi\right)\omega_n T}\right)\left(z - e^{-\left(\sqrt{\xi^2-1}+\xi\right)\omega_n T}\right) + c(z-1)\left(z - e^{-\left(\sqrt{\xi^2-1}+\xi\right)\omega_n T}\right) + d(z-1)\left(z - e^{\left(\sqrt{\xi^2-1}-\xi\right)\omega_n T}\right)}{z^2 - \left(e^{\left(\sqrt{\xi^2-1}-\xi\right)\omega_n T} + e^{-\left(\sqrt{\xi^2-1}+\xi\right)\omega_n T}\right)z + e^{-2\xi\omega_n T}} \right) \tag{41}$$

Then we can sort each z polynomial term on numerator. After sorting with simple linear combination and poles at mode 1, we can get the discrete transfer function on angular speed over voltage (i.e. $G_{\omega V}$) as equation (42) shown.

$$\frac{1}{k_b}\left(\frac{(1 + cp_2 + dp_3)z + cp_3 + dp_2 + p_2 p_3}{z^2 - (p_2 + p_3)z + p_2 p_3} \right) \tag{42}$$

Where p_2 and p_3 are same two poles at mode 1. By applying Table 5-1, $G_{\omega V}$ becomes

$$G_{\omega V}(z) = \frac{\Omega(z)}{V(z)} = \frac{0.211z + 0.161}{z^2 - 1.422z + 0.442} \tag{43}$$

5.5 Position and current control theory

In ESCON module mode 3, ESCON would perform current control inside. It use PI controller because the current plant would decrease one critical stability pole at s equal zero. Then we do not need to use extra zero from derivative control to cancel this probability causing unstable term.
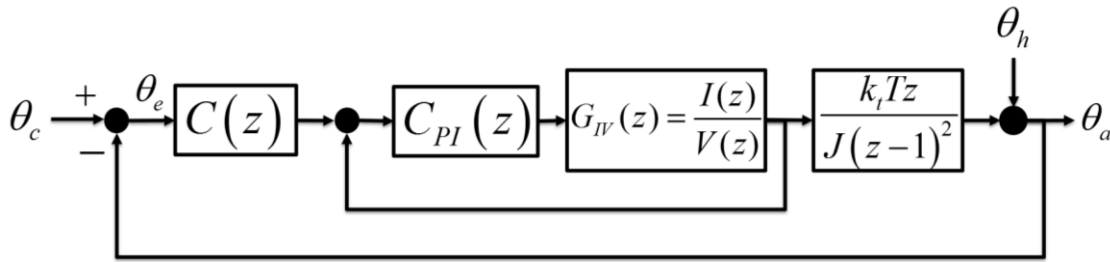

Fig. 5-11 Mode 3 control block diagram.

Again,

$$Js\Omega(s) = k_t I(s) \tag{44}$$

Analysis of the electric, including the back electromotive voltage $V_b = k_b \omega$, gives

$$V(s) = (Ls + R)I(s) + k_b\Omega(s) \tag{45}$$

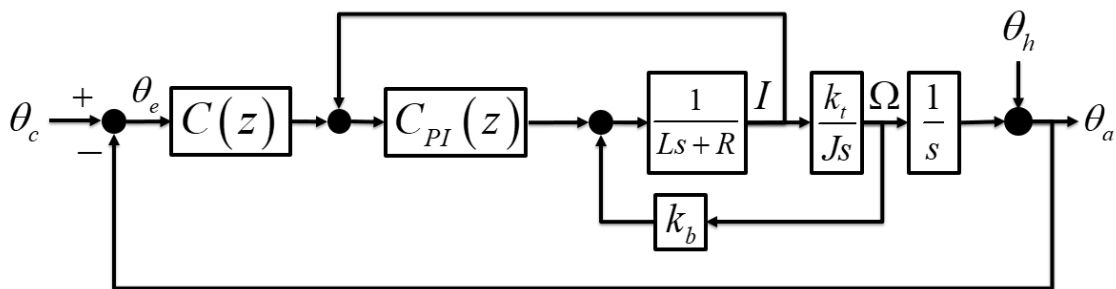The corresponding signal flow in control block diagram is shown in Fig. 5-12.

Fig. 5-12 Signal flow deviation for physical concept.

We simplify $\dfrac{k_t}{Js}$ with current feedback path. For pre-stage of this term, it should multiple this gain. For post stage of this term, it should divide this gain. Then we can

41

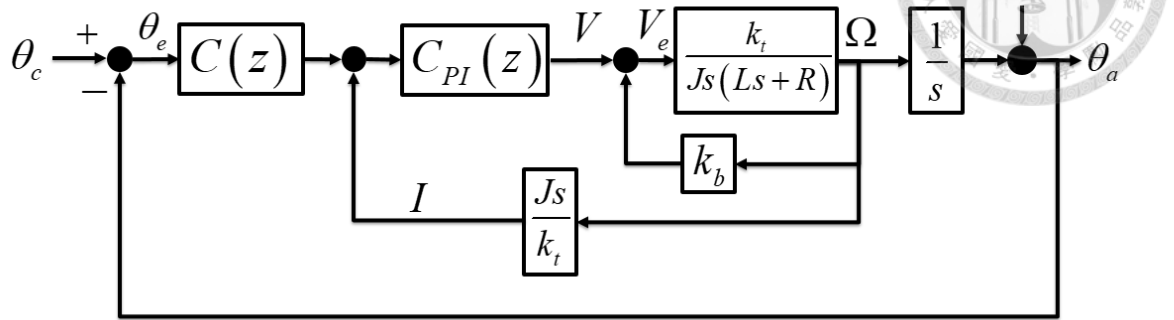obtain diagram in Fig. 5-13.

Fig. 5-13 Simplified signal flow.

We simplify closed loop path to open loop path, so we can get lower number of loop in total control block diagram. Therefore,

$$V_e = V - k_b \Omega \tag{46}$$

For plant output and input relation,

$$\Omega = \frac{k_t}{Js(Ls+R)} V_e \tag{47}$$

Then,

$$\Omega \left(1 + \frac{k_b k_t}{Js(Ls+R)} \right) = \frac{k_t}{Js(Ls+R)} V \tag{48}$$

$$\frac{\Omega}{V} = \frac{k_t}{Js(Ls+R) + k_b k_t} \tag{49}$$
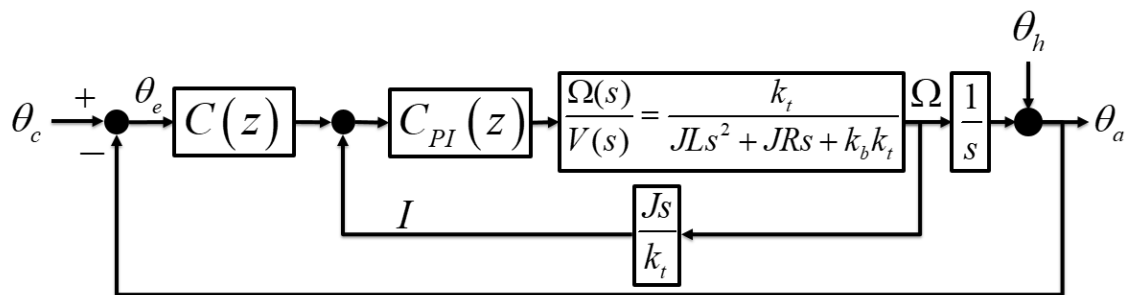
Sorting equation (49), we can get the diagram in Fig. 5-14.

Fig. 5-14 Second simplified signal flow.

42

In this standard form, there are two characteristic properties, which are natural frequency (ω_n) and damping ratio (ξ). These two properties play an important role in system response. In our case, these two properties can be written as equation (10) and (11). Sorting equation (49) with two characteristic properties, the transfer function can be established.
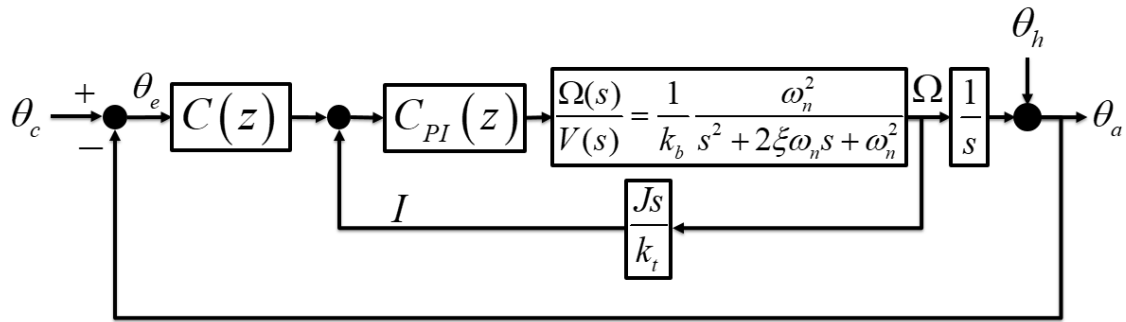

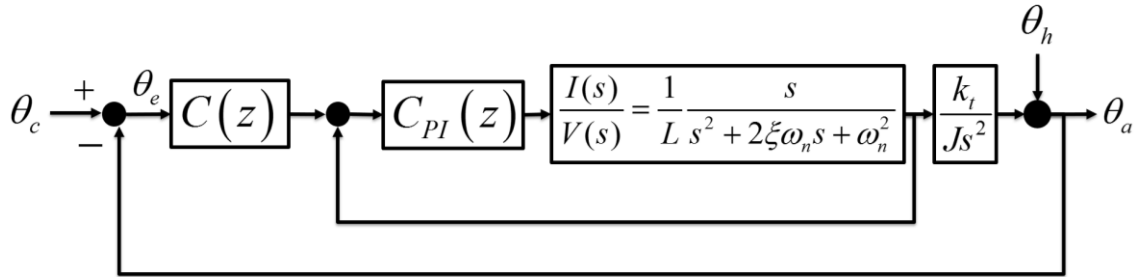Fig. 5-15 Third simplify signal flow.

Fig. 5-16 Complete signal flow.

To find the transfer function of current over voltage for one of phases for BLDC with equivalent circuit shown in Fig. 5-9, we have effective inertia J. The motor characteristics are $\tau = k_t i$ and $V_b = k_b \omega$. From the free body diagram for rotor in Fig. 5-9,

$$J\omega = k_t \int i\, dt \tag{50}$$

Analysis of the electric circuit, including the back electromotive voltage, $V_b = k_b \omega$, gives

43

$$v = L\frac{di}{dt} + Ri + k_b\omega \tag{51}$$

Substituting current a $\omega = \int\frac{k_t i}{J}dt$ into equation (51) gives

$$v = L\frac{di}{dt} + Ri + \frac{k_b k_t}{J}\int i\,dt \tag{52}$$

The Laplace transform of equation (52) is

$$V(s) = \left(Ls + R + \frac{k_b k_t}{Js}\right)I(s) \tag{53}$$

that can be rewritten as

$$\frac{s}{L}V(s) = \left(s^2 + \frac{R}{L}s + \frac{k_b k_t}{JL}\right)I(s) \tag{54}$$

Sorting equation (54) with two characteristic properties, the transfer function for the motor is readily found to be:

$$G_{IV}(s) = \frac{I(s)}{V(s)} = \frac{1}{L}\frac{s}{s^2 + 2\xi\omega_n s + \omega_n^2} \tag{55}$$

We use similar way to get discrete transfer function as below.

$$G_{IV}(z) = \frac{p_2 - p_3}{2\sqrt{\xi^2 - 1}\omega_n L}\frac{z - 1}{z^2 - (p_2 + p_3)z + p_2 p_3} \tag{56}$$

Where p_2 and p_3 are same two poles at mode 1. By applying Table 5-1, equation (56) becomes

$$G_{IV}(z) = \frac{I(z)}{V(z)} = \frac{1.809z - 1.809}{z^2 - 1.422z + 0.442} \tag{57}$$

44

Chapter 6 Exoskeleton control system design

6.1 Gait test and command statement

A normal gait cycle can mainly divide into two phase. First phase is stance phase, which is first 60%. Within this phase, target leg would touch ground and sweeping from positive max angle value to negative max angle value, then the leg would prepare to swing. There are five sections happen within this phase. Target leg would sweep from positive max angle value to zero value within first section to third section. Therefore, third section is called as mid-stance. Target leg would sweep to negative max angle value in fourth section and preparing to swing leg in fifth section. Second phase is swing phase, which is last 40%. Within this phase, target leg would sweep to positive max angle value in air. There are three sections happen within this phase. These three sections is called as initial, mid and terminal swing respectively.

We use normal adult gait data from the literature [45]. We pick hip rotation as our angular rotation command. The original gait data has one hundred elements within a gait cycle. We reduce it into eight points in this work. Human average walking speed is one gait cycle per second. If we want to track one hundred command very well, we should design settling time for each command below 0.01 second. System response will be high overshoot. The controller would pull back moving bar to pursuit high accurate position control. However, human body would keep go through forward despite of body mass inertia based on Newton's first law, which would become the barrier for controller pulling moving bar back. The controller will give higher PWM duty to pull bar, making user uncomfortable. To assist human smoothly, we choose eight main gait cycle sections and their neighbor data as total twenty-nine command for whole gait cycle.
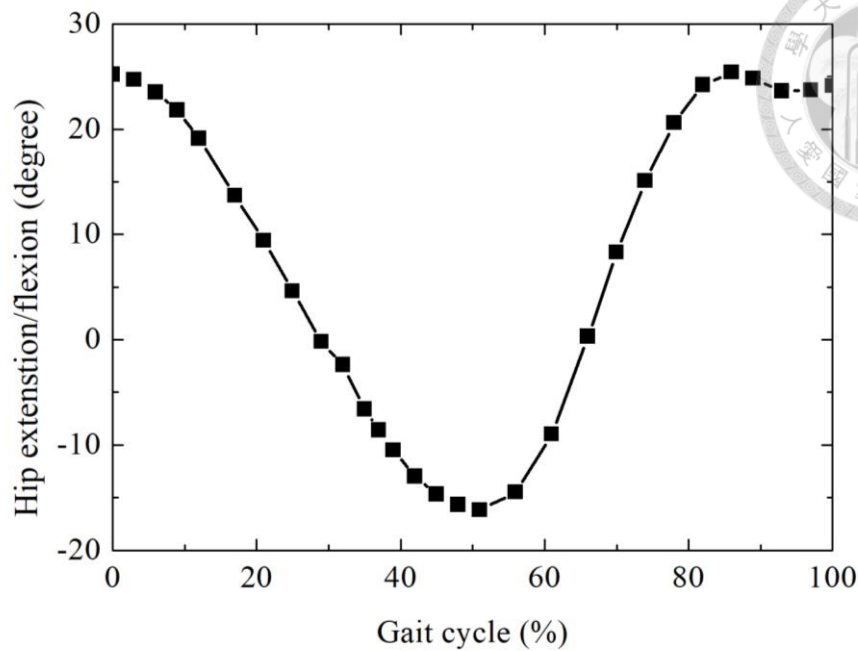
Fig. 6-1 Hip angle rotation command within a gait.

6.2 Motor position control

We should verify that our control system is safe for human to use first. Then we should verify whether the exoskeleton could assist human or not. Finally, by adding emergency stop subsystem, we can test human subject in our exoskeleton.

ESCON mode 1 is open-loop speed control. The only thing that the servo amplifier does is to stabilize voltage supply by IXR compensation. Hence, in Mode 1 the ESCON controller works as a voltage amplifier.

Shahrokhi et al. [46] have discussed the parameter modulation for PID controller. They focused on one to third order system. They sorted appropriate PID tuning method corresponding to each system. They deduced that the third order system is good to use by adopting Ziegler-Nichols method to design PID controller parameters. Because our system is also a third order system, we use Ziegler-Nichols method to design our PID control parameters [47].

First step to design PID controller is to set $T_I = \infty$ and $T_D = 0$. This step let

46

controller do just proportional control part for the whole system. Then we adjust k_p and observe system performance such as motor driving and exoskeleton rotated angle. Below we would use root locus method to help us adjust k_p. Until system reaching critical stability for appropriate k_p, we record this k_p and call it as critical gain k_u. The system at critical stability would perform oscillation. Its period is referred to as the critical period T_u.

We design appropriate T_I so that the system can oscillate with equilibrium point as our steady state value. The third step is design appropriate T_D to reduce overshoot, which is caused by oscillation, without too slow speed.

We use plant root locus diagram to find k_p candidate, then check whether k_p is appropriate or not by step response of this system. The root locus design is to find scalar gain growing situation. Considering open loop gain, we let it plus one to solve its solution with variation of scalar gain. This plus one equation is the characteristic equation from close loop transfer function. The characteristic equation can mainly influence system properties and it would change by different gain adjustments.

Root locus can influence system properties such as damping ratio and natural frequency. Damping ratio can change system overshoot percentage, which can speed up the system response or cause system to be unstable. System settling time means how long does the system reach stable value. It is changed by different damping ratio and natural frequency chosen by gain k_p.

Root locus diagram about our plant in shown Fig. 6-2. We choose appropriate k_p as value 15.69. This point on root locus is inside unit circle on Z domain. We predict this gain can help us reach critical stability for system.
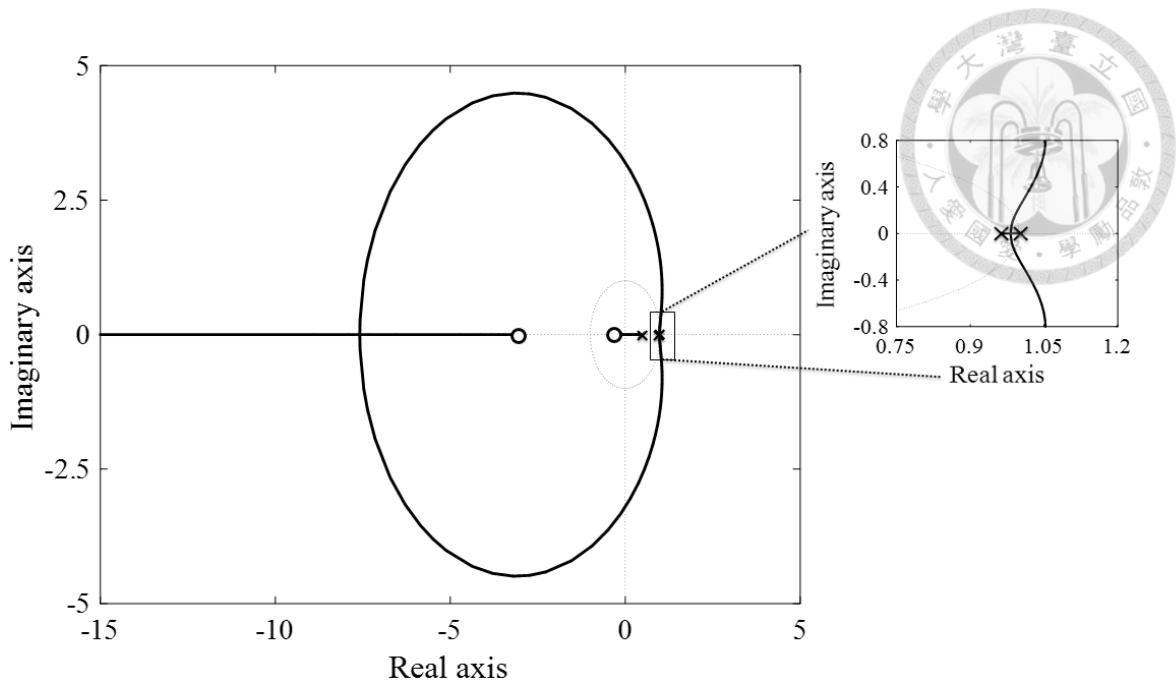
Fig. 6-2 Root locus diagram for mode1 plant.

To make sure whether this gain reach critical stability or not, we multiple this pure proportional controller with our plant. Then we conduct unit feedback to construct closed loop system. We use step signal to test this closed loop system, as shown in Fig. 6-3. We can observe the response showing large oscillation initially and its performance gradually back to level line, which value is the amplitude of testing step function. From our observation, we can induce that this system is almost reaching critical stability condition and defining our design k_p is critical gain k_u. We pick the first peak and second peak time data. After sorting them, we can get critical period T_u.
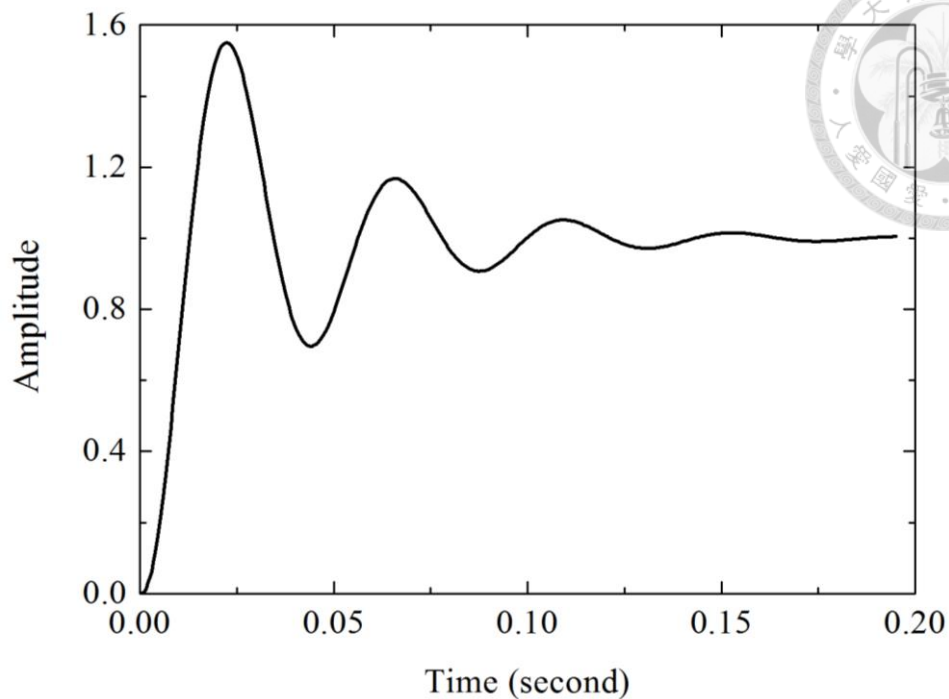
48

Fig. 6-3 Step response for P control mode 1.

We use T_u and k_u to adjust T_I and T_D. T_I can reduce steady state error, but it would enlarge oscillation. We would design T_D to reduce oscillation. We should avoid choosing too large T_D for reducing oscillation. Otherwise, the system would show very slow response. After design, we can get appropriate PID gains as k_p value is 15.69, T_I value is 0.145 sec and T_D value is 0.02457 sec.

Now, we use its step response to observe system's overshoot, rise time and steady state error. To ensure that the system would not damage the mechanism, we need overshoot not too much to trig the limit switch, which may produce mechanism stop running. The rise time need not so fast to damage human's leg. Steady state error needs to be lowered to make a precision gait cycle. The step response graph is presented in Fig. 6-4. Thanks to small overshoot so that system can reach steady state with settling time 0.022 sec. This overshoot is over one, which is the amplitude of step signal, only 0.04.

49

We believe that this small over amount is acceptable in our model because the value of the biggest angle multiple of 1.04 is still dropped into the cylinder sliding range and the limit switch would not be triggered.
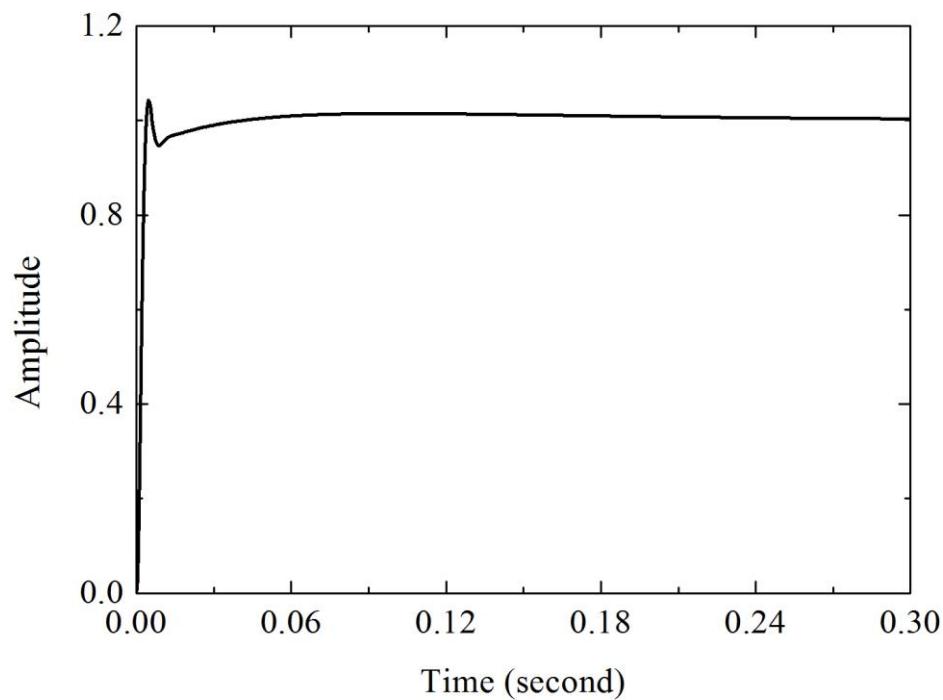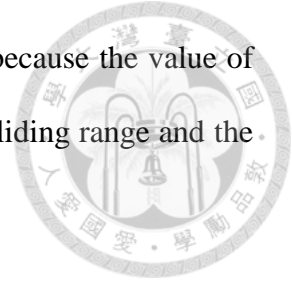

Fig. 6-4   Step response for PID control mode 1.

6.3   Position and speed closed loop control

In this section, we would design position controller parameter for ESCON mode 2. In mode2, ESCON would do PI closed loop control, which value are $k_p = 1736$ and $T_I = 13.4\text{ms}$, for speed. The parameters are determined by ESCON auto tuning. Auto tuning would rotate motor CW and CCW alternatively. This rotation can help ESCON to deduce appropriate controller parameters.

We use root locus diagram about our plant in Fig. 6-5. Because the ESCON PI controller would give us one pole and one zero, it seems more difficult to get stable

50

response than mode 1. Therefore, we choose appropriate k_p as value 3.701e-6 and 4.059e-6. This point on root locus is inside the unit circle on Z domain. Its small value can make sure that the system response is stable.
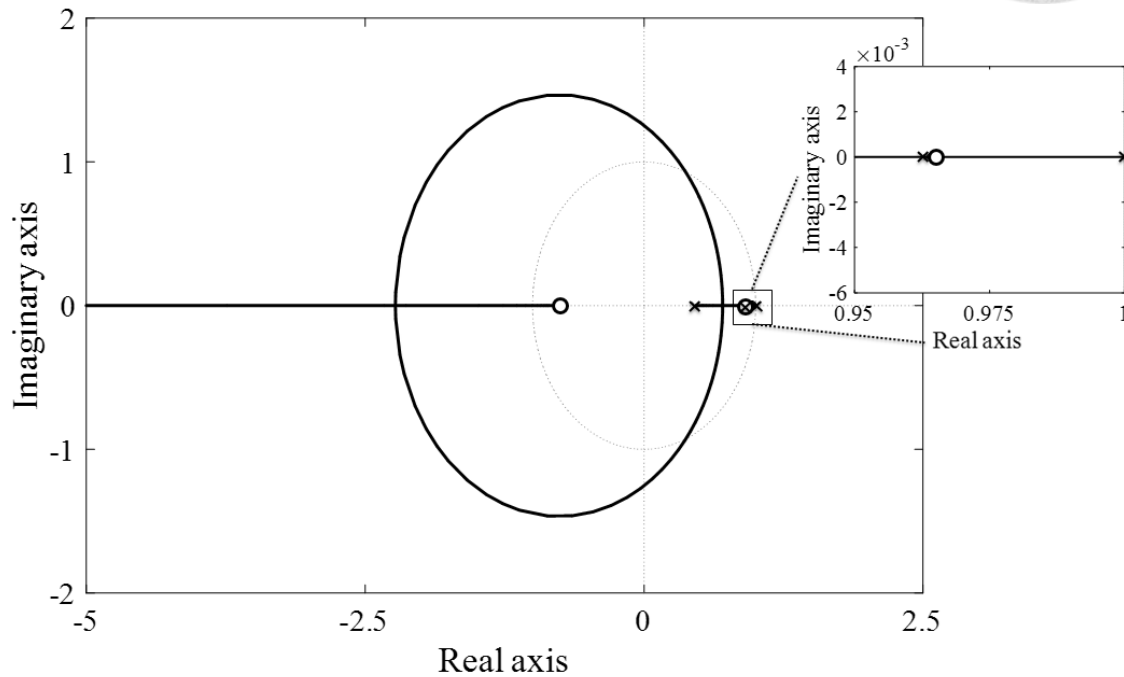

Fig. 6-5   Root locus diagram for mode 2 plant.

We multiple this pure proportional controller with our plant and conduct unit feedback to construct closed loop system. We use step signal to test this closed loop system, as shown in Figs. 6-6 and 6-7. Although this response does not have overshoot, we can make sure pure proportional control can reach steady state value with the settling time of 0.433 sec.
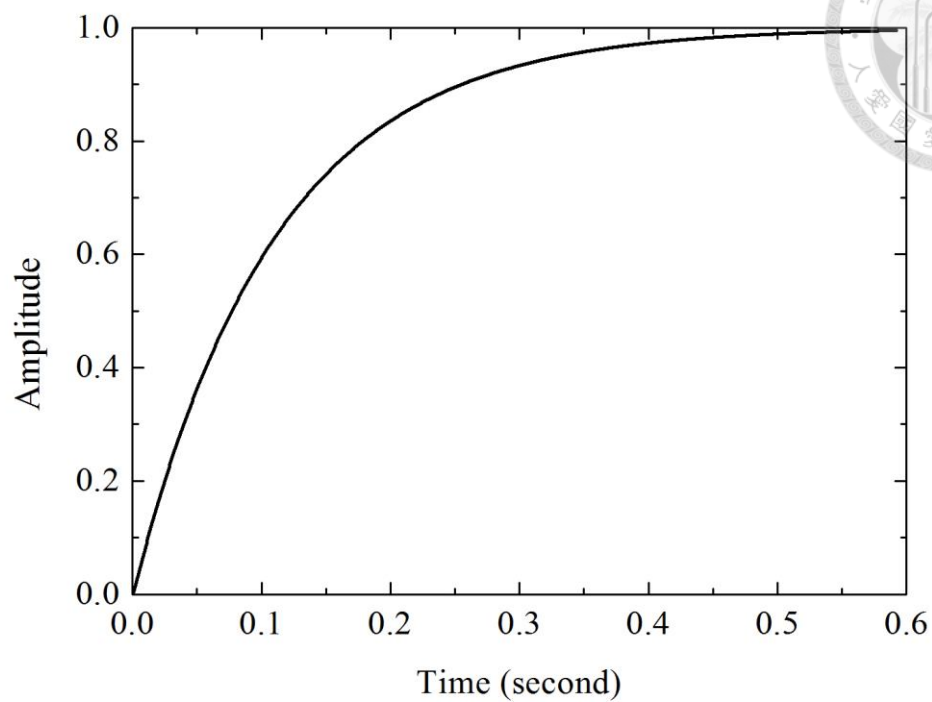
51

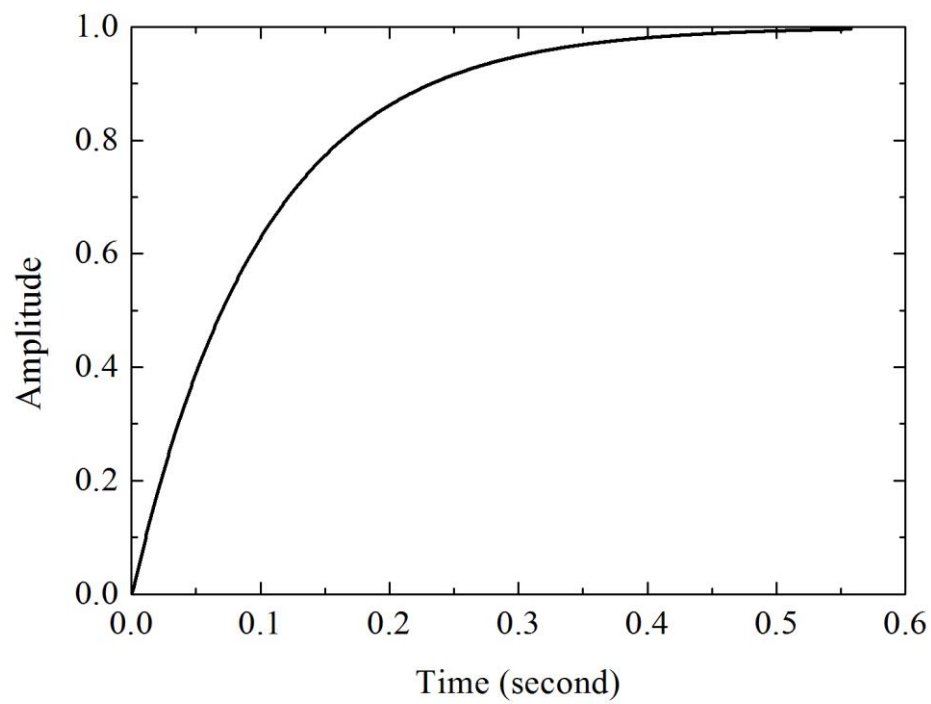Fig. 6-6   Step response for first P control mode 2.

Fig. 6-7   Step response for second P control mode 2.

52

Comparing to mode 1 settling time, mode 2 time is longer. We should use T_I to increase this time. To avoid T_I to enlarge too much oscillation for the system, we should design appropriate T_D to reduce T_I vibe. After designing T_I, whose values are 0.4171 sec and 0.3809 sec, and T_D, whose values are 9.601e-3 sec and 8.780e-3 sec, we use step response to observe system's overshoot, rising time and steady state error. Again, we need overshoot not too much to trig the limit switch. The rising time needs not to be too fast to damage human's leg. The steady state error needs to lower to make a precise gait cycle. The step response graph is presented in Fig. 6-8 and Fig. 6-9. These responses can reach steady state. Comparing to mode 1, these responses have lower rising time. This slow rising time can provide users with more comfortable wearing experience.
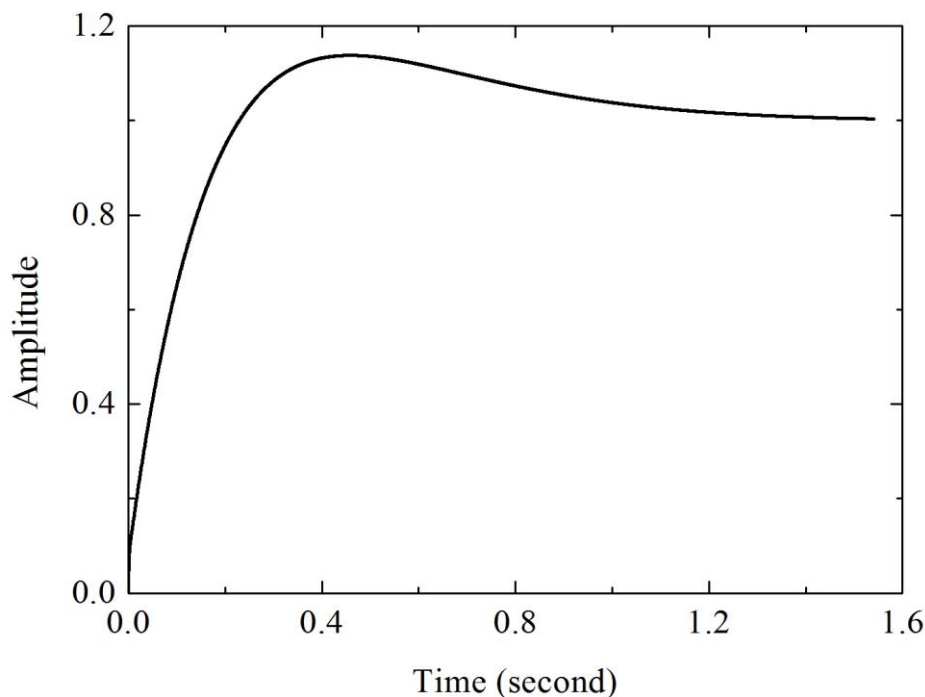

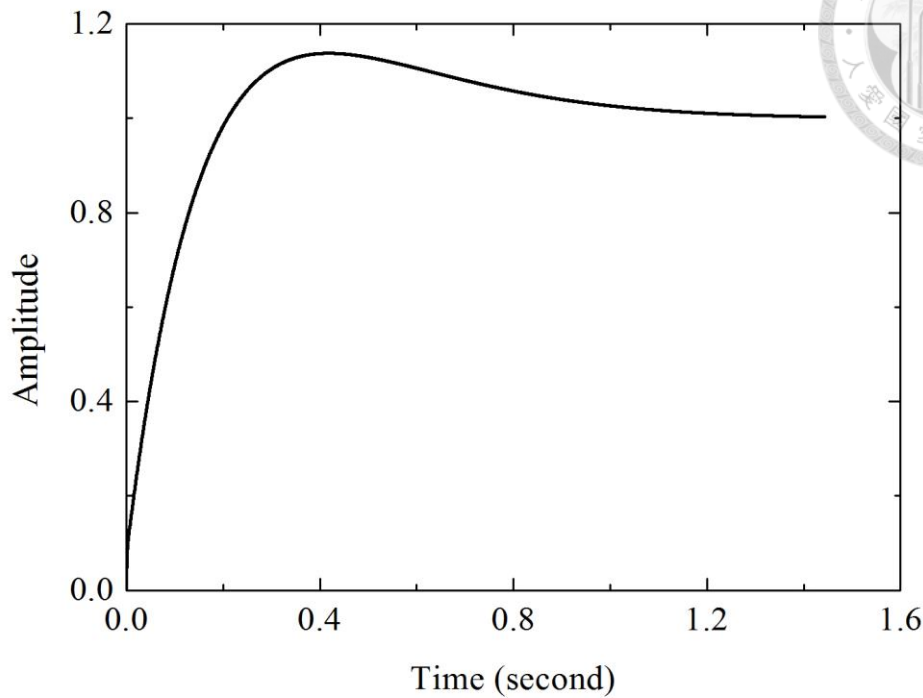Fig. 6-8 Step response for first PID control mode 2.

Fig. 6-9   Step response for second PID control mode 2.

6.4   Position and current closed loop control

In this section, we would design position controller parameter for ESCON mode 3. In mode 3, ESCON would do PI closed loop control, which value are $k_p = 117$ and $T_I = 382\mu s$, for current.

Again, we use root locus diagram about our plant in Fig. 6-10. Because ESCON PI controller would give us one pole and one zero, it seems more difficult to get stable response than mode 1. Therefore, we choose appropriate k_p as value 4.333e-6. This point on root locus is inside the unit circle on Z domain. Its small value can make sure that the system response is stable.
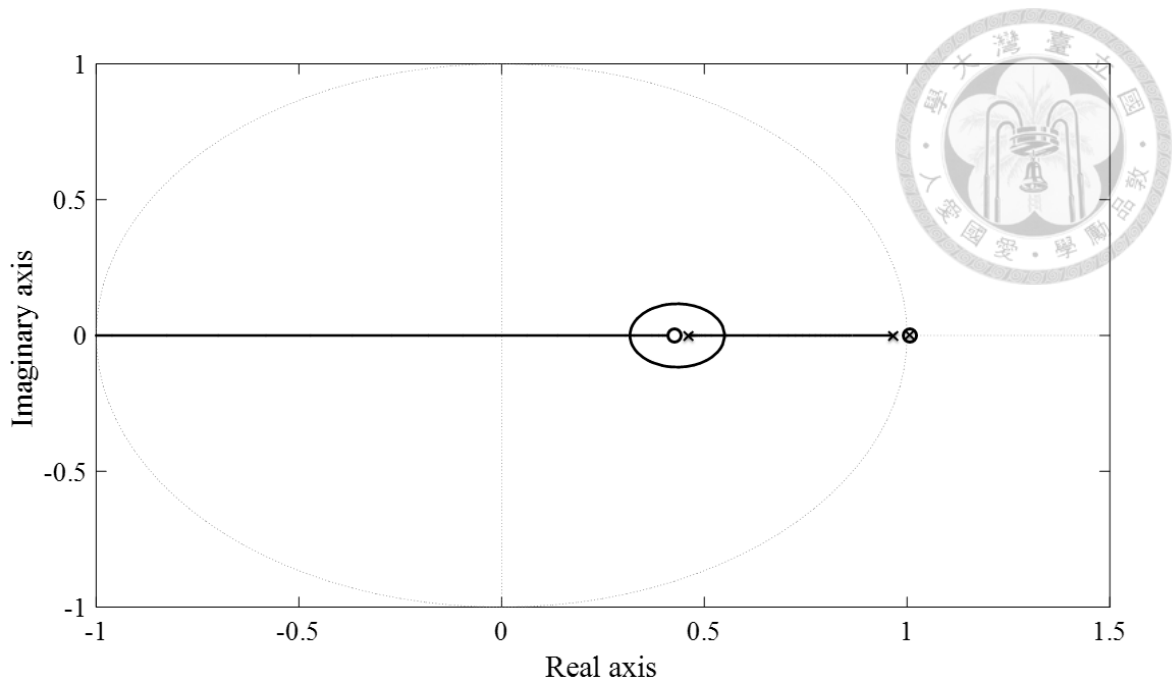
54

Fig. 6-10 Root locus diagram for mode 3 plant.

We multiple this pure proportional controller with our plant and conduct unit feedback to construct closed loop system. We use step signal to test this closed loop system, as shown in Fig. 6-11. The response show large steady state error.
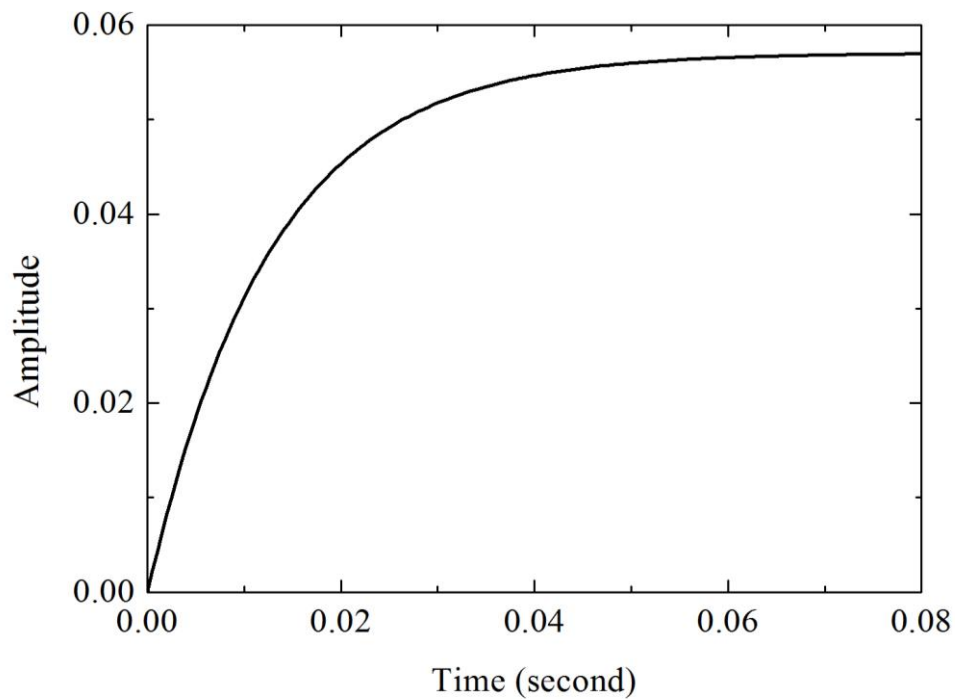

Fig. 6-11 Step response for P control mode 3.

55

We should design T_I and T_D to compensate k_p weak ability for reaching steady state. We adjust T_I to enlarge oscillation to make sure that it can oscillate with equilibrium point with steady state value, which is the amplitude of step signal. We then adjust T_D to reduce oscillation. After designing T_I, which value is 5e-4 sec, and T_D, which value is 1.25e-4, we use step response to observe system's overshoot, rising time and steady state error. Same as previously consideration, we need overshoot not too much to trig the limit switch. The rising time needs not to be too fast to damage human's leg. The steady state error needs to be lowered to make a precise gait cycle. The step response graph is presented in Fig. 6-12. The response converges to a steady state value.
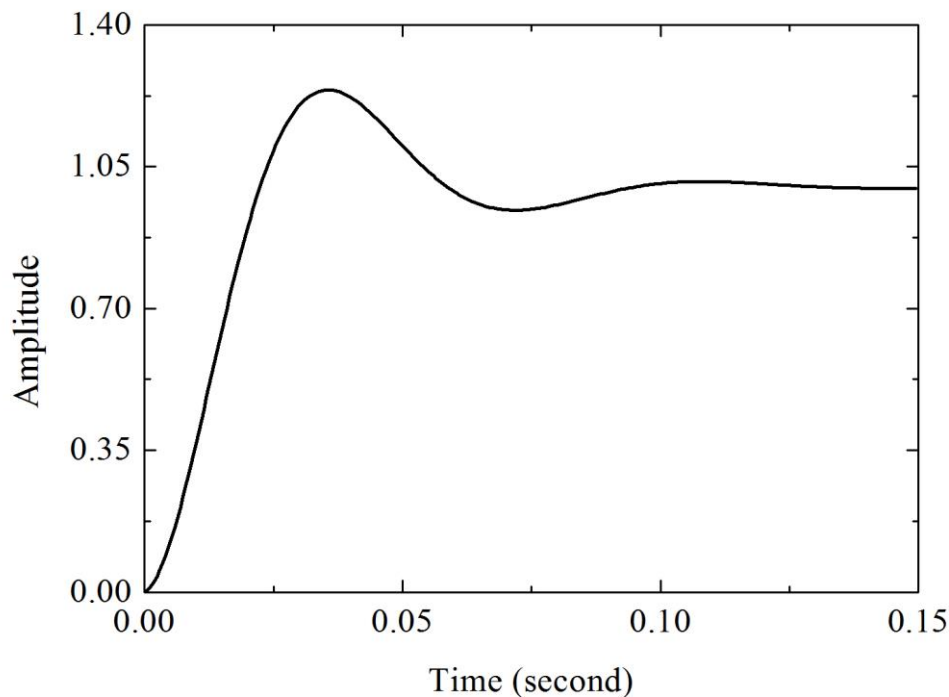

Fig. 6-12 Step response for PID control mode 3.

Chapter 7 Exoskeleton results and discussions

7.1 Implement control system

For ESCON, we define PWM relation on digital input with 5V within interval 10% to 90% and speed from 0 to 2657 rpm, which is 0 to 278 rad/s, as shown in Fig. 7-1. We design motor enabler and motor direction on the other two digital input pins. With 5 V input to both pins, ESCON would drive motor with CCW direction at appropriate speed, manipulated by PWM duty input. In addition, we set ESCON 2 analog output to read motor averaged speed and averaged current, respectively. The delay process in digital control is averaged. We sense angle by capturing A and B phase counter value from MAXON 4096 digital increment encoder to calculate rotated angle. This encoder A and B have 90-degree delay, and it is called quadric encoder.
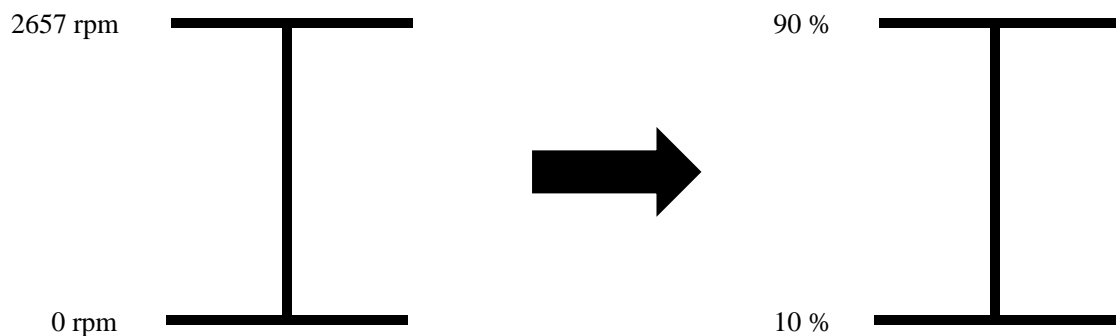

| 2657 rpm | 90 % |
| 0 rpm | 10 % |

Fig. 7-1   Motor speed and PWM duty transformation.

We wrote LABVIEW program to implement our PID control algorithm. Any machine should calibrate before operation. We design zero calibration on pre-sequence of main control sequence. Zero means human's two legs at standing phase. The button is to signal for program running. If the user does not press the button, the sequence would not start and the motor would not drive. After the user press the button, the program would detect whether the Hall sensor receive magnetic flux or not due to this signal is flag for zero calibration. If the flag is reached, the program would disable the motor

57

driving and set encoder value as zero. Then the system is prepared for doing main control sequence. Otherwise, the motor would drive with low speed to reach flag until the slot cylinder triggers the limit switch. After triggering, the motor will change direction. Then the motor keeps running at low speed to reach zero.
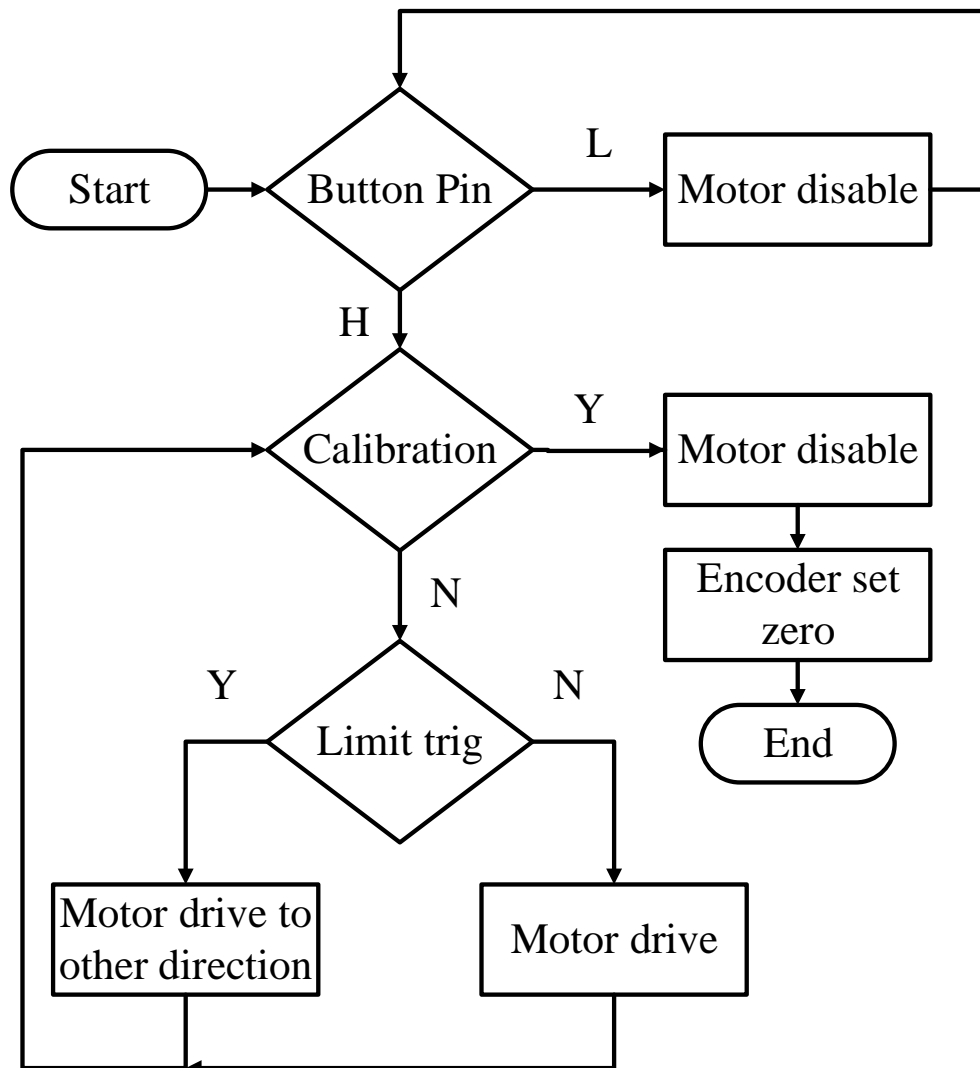

Fig. 7-2 Zero calibration flow chart.

In main control sequence, we well design stop system in many aspects. When user press user interface stop button, system will stop motor and capture data for later analysis. Slot cylinder triggers the limit switch or user press button to let button pin receive low voltage are two methods to calibrate system and stop motor driving. In

58

normal usage, user would press button to let button pin receive high voltage. Then the program would check which angle command, which we define at section 6.1, motor should drive to. Comparing to the actual angle read by encoder, the command value would minus actual angle value to get angle error. This error would become PID angle position controller input. The controller will calculate appropriate control value from -100 to 100. We classify the negative and positive value as the two cases and define their rotation direction as CCW and CW, respectively. After dealing sign convection, we define transformation on control value from 0 to 100 and PWM relation within interval 10% to 90%, as shown in Fig. 7-1. Therefore, PWM duty will tell motor how fast it should rotate. When the error is small enough, program would judge that command is tracking. Then program would continue to run to the next command.
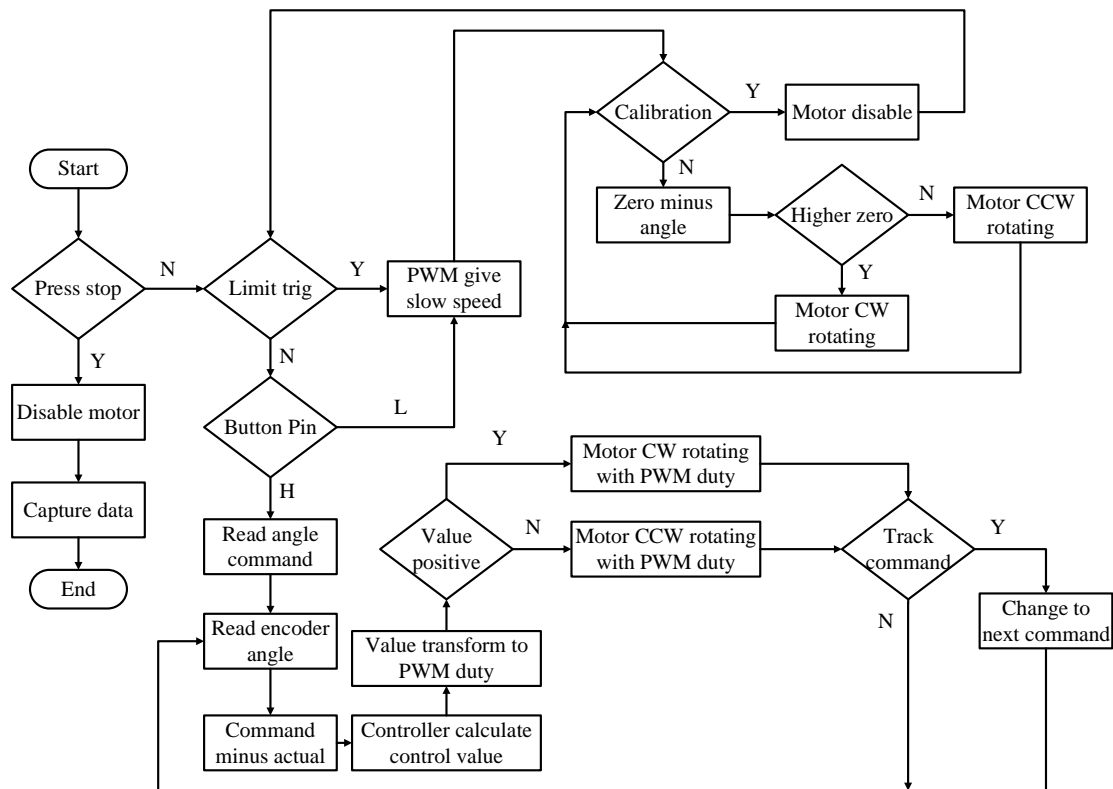

Fig. 7-3 Main program flow chart.

59

7.2   Exoskeleton position control

We key in designed PID controller parameters to Myrio program and set ESCON module as mode 1. Now the system will only do closed loop position control, and we let motor rotate exoskeleton leg. We choose different IXR compensation situation during mode 1 test. The results are shown in Figs. 7-4 and 7-5.
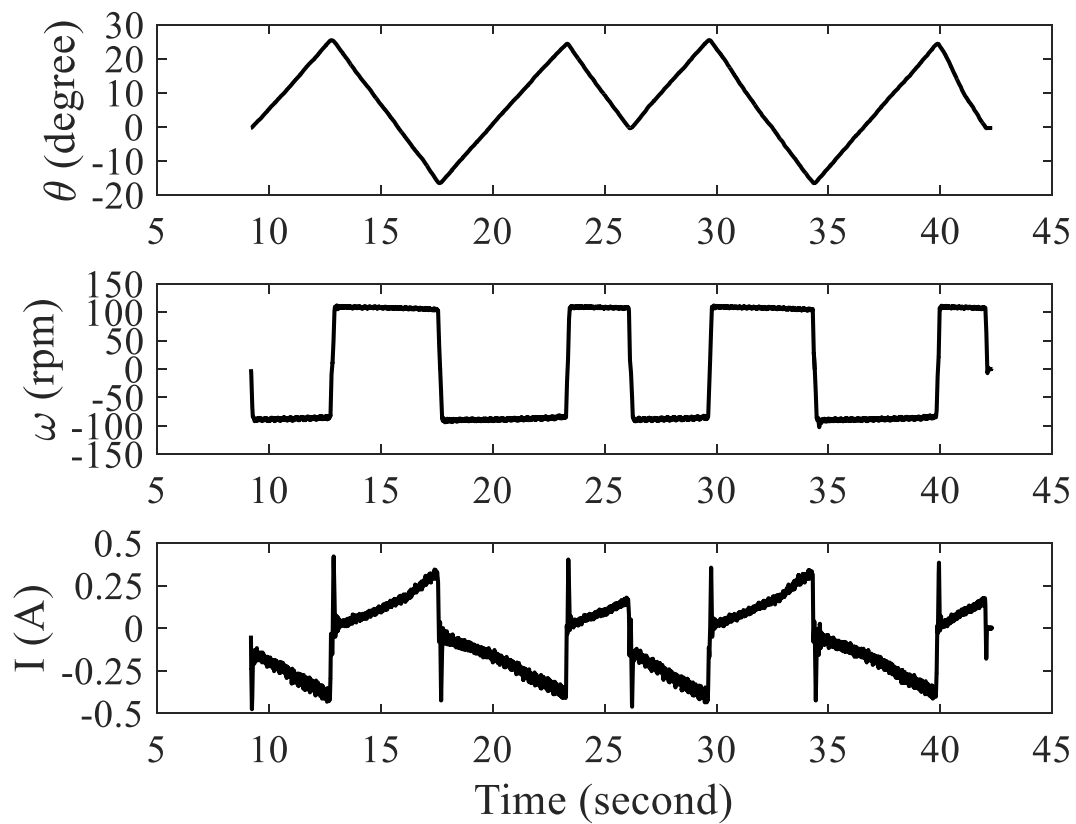

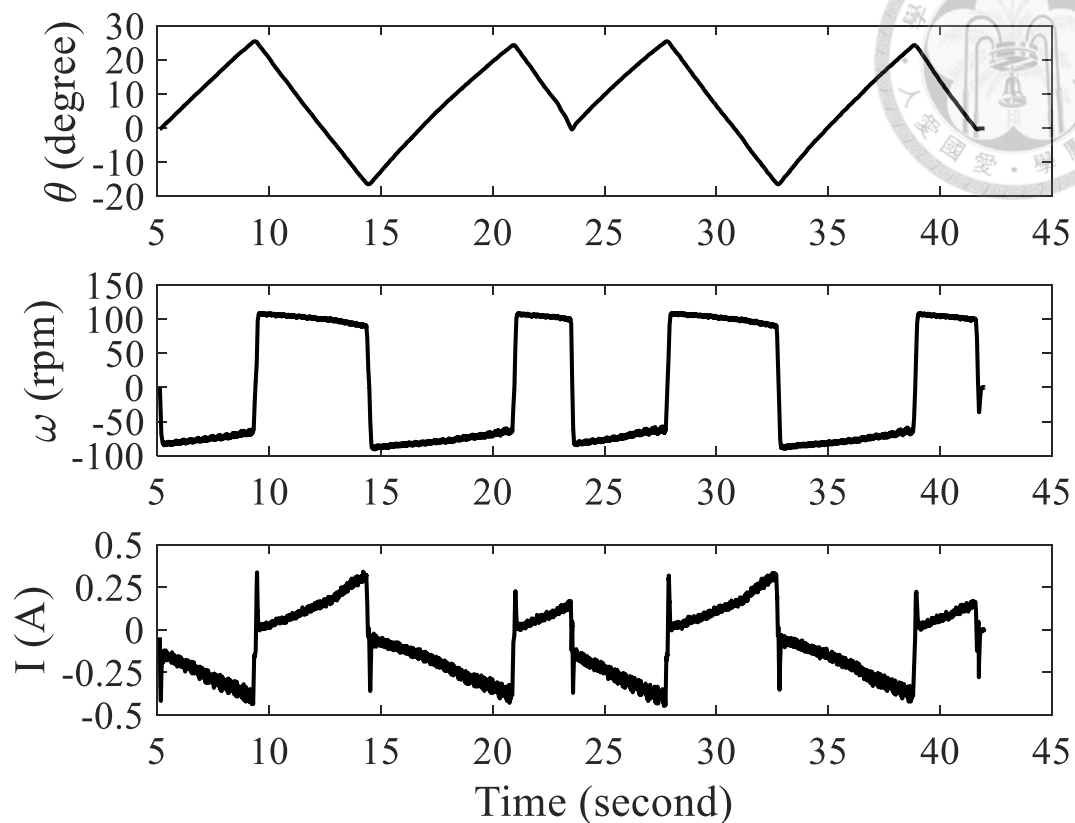Fig. 7-4   Mode 1 adaptive IXR testing result.

Fig. 7-5   Mode 1 static IXR testing result.

For both cases, we can discover that the angle correctly follow our command input. The current has little oscillation during acceleration and deceleration. For current acquiring, we could add analog electronic filter behind ESCON motherboard circuit to stabilize this little noise. The most difference between adaptive and static compensation is the speed curve. As previously written, the IXR compensation is to stabilize supply voltage, which means speed can be stabilized by adaptive IXR compensation. Adaptive IXR compensation depends on the loading situation to adjust compensation parameter, which means that it adjusts its circuit internal resistance to compensate a stable speed. In other viewpoint, static compensation have same internal resistance as ESCON setting motor parameter before we combine exoskeleton mechanism loading. As Fig. 7-4 shows, the angular speed is like horizontal rectangular shape in adaptive compensation. The angular position would be a triangle (or peak) shape with rectangular constant value

61

integrated within each sampling. In static result as Fig. 7-5 shows, the angular speed has ramp shape during exoskeleton moving bar swing whether CCW or CW, which means fixed IXR compensation parameter would have no ability to stabilize voltage during swing phase. Fortunately, our designed PID controller would modulate angular position error, which is happening when encoder read angle did not equal to the command angle, with three gains. The controller will have high duty cycle output for ESCON servo amplifier PWM input pin. After receiving high PWM duty signal, ESCON will give more voltage to motor. In physical viewpoint, we can discover angular speed rise during swing with static IXR compensation. To sum up, both cases can reach our desired angular position command.

7.3 Exoskeleton position and speed control

Exchange PID gains in Myrio program and changes ESCON module as mode 2. Mode 2 is closed loop speed control mode. The difference between mode 1 and mode 2 is that mode 1 only does voltage stabilization during motor driving. In mode 2, ESCON module acts as PI speed controller for controlled plant. ESCON module will do closed loop angular speed control, and Myrio would still do closed loop angular position control. We use two designed control parameters doing without human test as below.
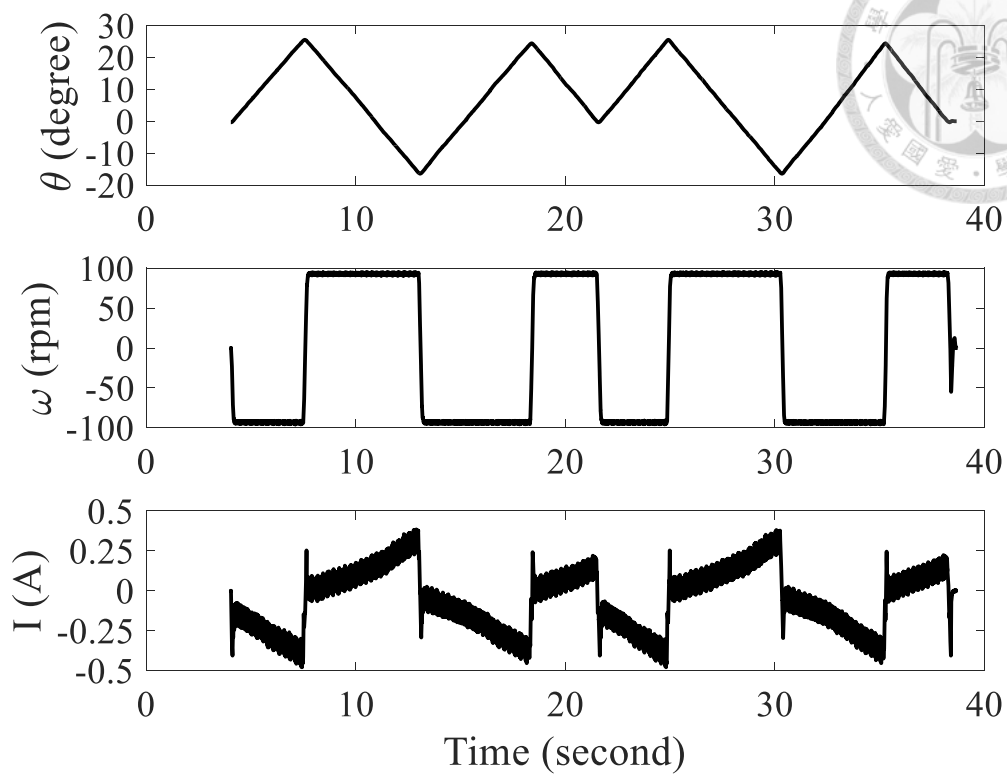
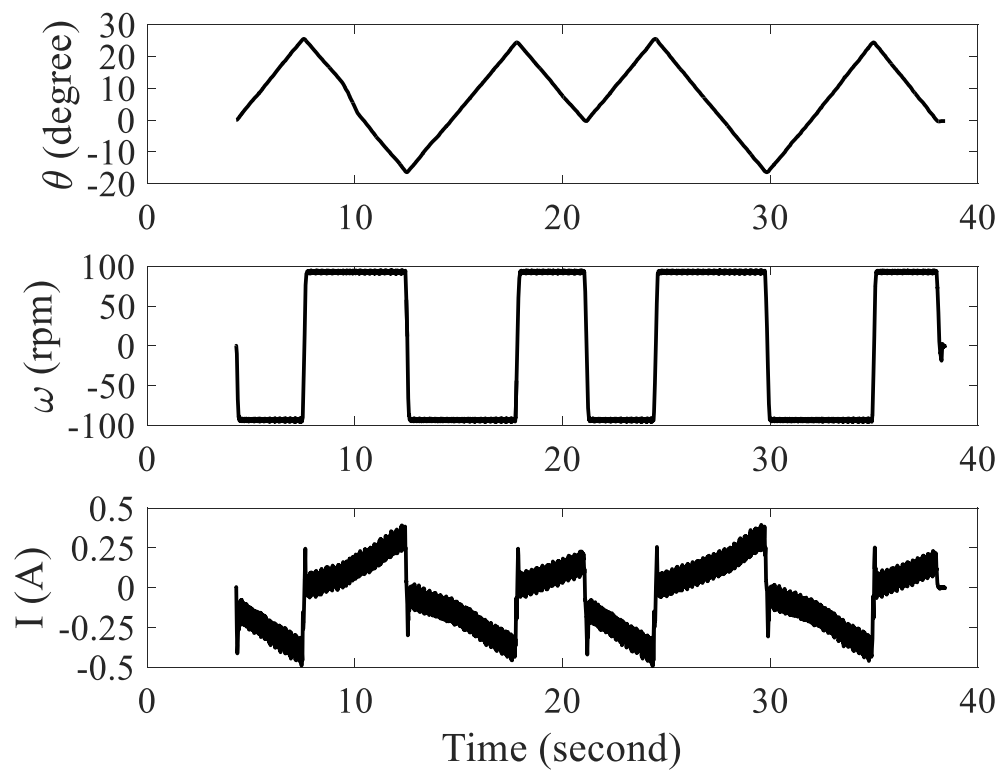Fig. 7-6   Mode 2 control parameter group A testing result.

Fig. 7-7   Mode 2 control parameter group B testing result.

63

In mode 2 test, we can discover that speed perform flat result at speed control steady state. For speed curve, we can see that the speed command does not have overshoot, which can give human comfortable wearing experience. For current acquiring, it shows very large noise. The possible reason is the noise-disturbing measurement. We should add analog filter behind ESCON motherboard to modify it. The current implies acceleration information due to Newton's law. We can see the tendency that current integration would have chance to correspond to speed information.

7.4   Exoskeleton position and torque control

We exchange PID gains in Myrio program and change ESCON module as mode 3. Mode 3 is closed loop current control mode. In mode 3, ESCON module acts as PI current controller for controlled plant. The ESCON module will do closed loop current control and Myrio will still do closed loop angular position control.
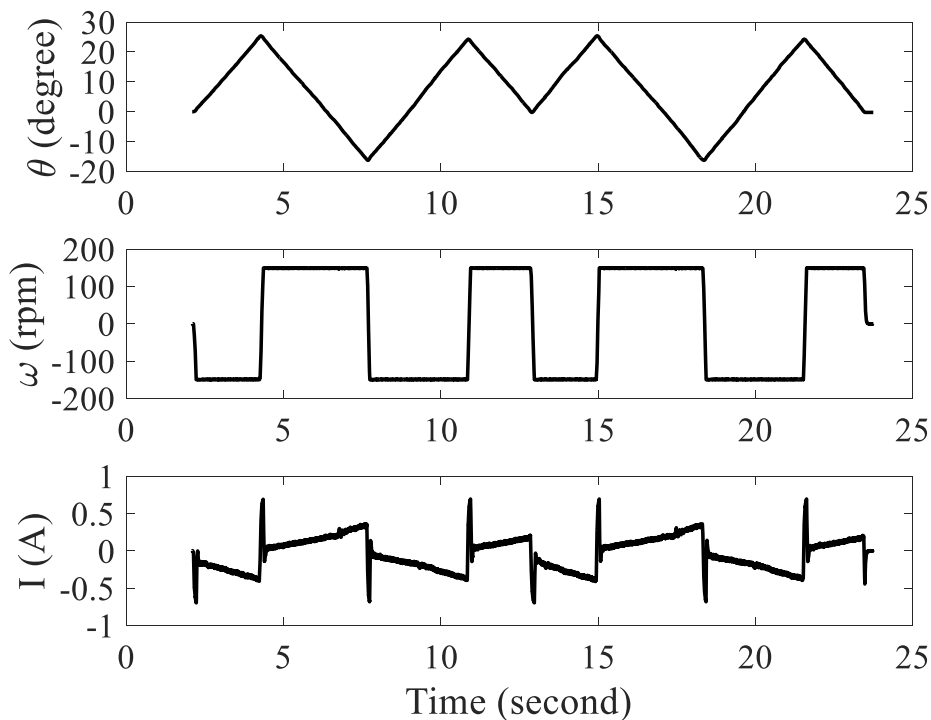

Fig. 7-8   Mode 3 testing result.

64

In mode3 test, we can discover that the current perform bigger overshoot than other modes to pursuit steady state. For current acquiring, its noise is still big. The possible reason is the noise-disturbing measurement; we should add analog filter behind ESCON motherboard to modify it. The current implies acceleration information due to Newton's law. We can see the tendency that the current integration will have chance to correspond to speed information.

In above three modes test, we can discover that mode 3 have biggest current overshoot. This overshoot is easy to rotate motor too much angle so that the limit switch would trigger to protect the mechanism. In chapter 6, we discover that mode 2 have lower rising time than mode 1. With lowered rising time, human muscle can avoid hurt with sudden motor driving. To sum up, we choose ESCON mode 2 to implement control algorithm on wearing exoskeleton on human, which is called auto walking mode in this thesis.

We want to make sure that our exoskeleton can perform enough speed to follow human natural walking speed. Before speeding up system, we should check two motors rotating consistently so that two exoskeleton legs can sweep as human walking. The testing results are shown in Figs. 7-9 and 7-10.
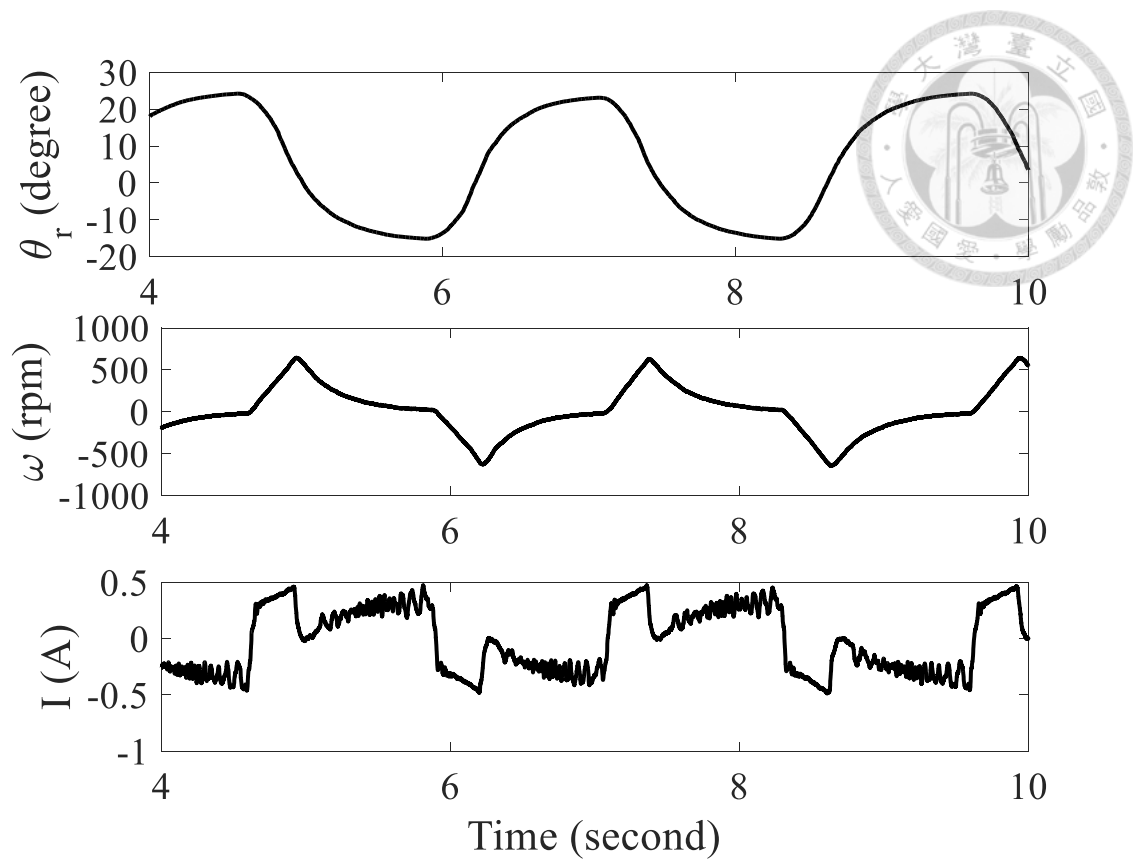
Fig. 7-9   Right leg test without human in auto walking mode.
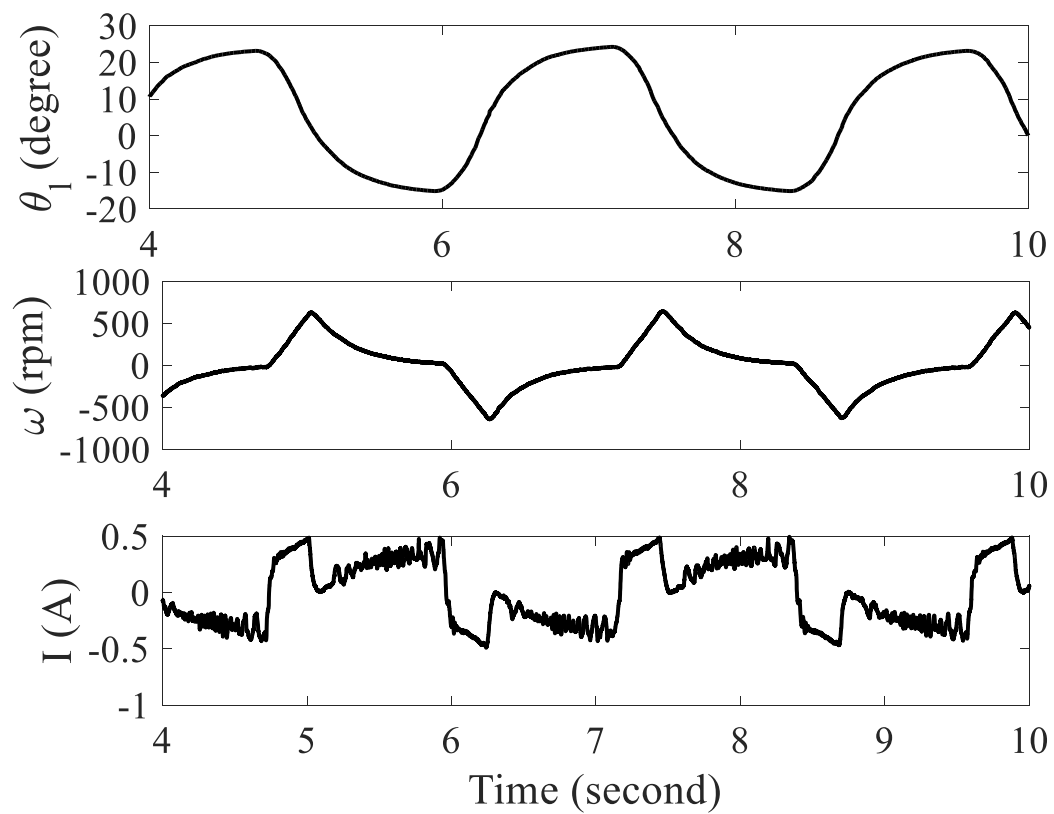

Fig. 7-10 Left leg test without human in auto walking mode.

66

For angle position coordinate, positive angle means motor rotating clockwise, which means right thumb is point to motor bottom, vice versa to negative angle. We then focus on angle peak-to-peak data, which is one gait cycle data. It seems that two legs perform the same result. Because motor axis points to different direction, the motors will perform different leg sweep situations with the same angle command.

The two-leg testing results are shown in Figs. 7-10 and 7-11. Vibe would break consistent property for two legs angle position information. This odd vibe would be explained after the speed-up test.
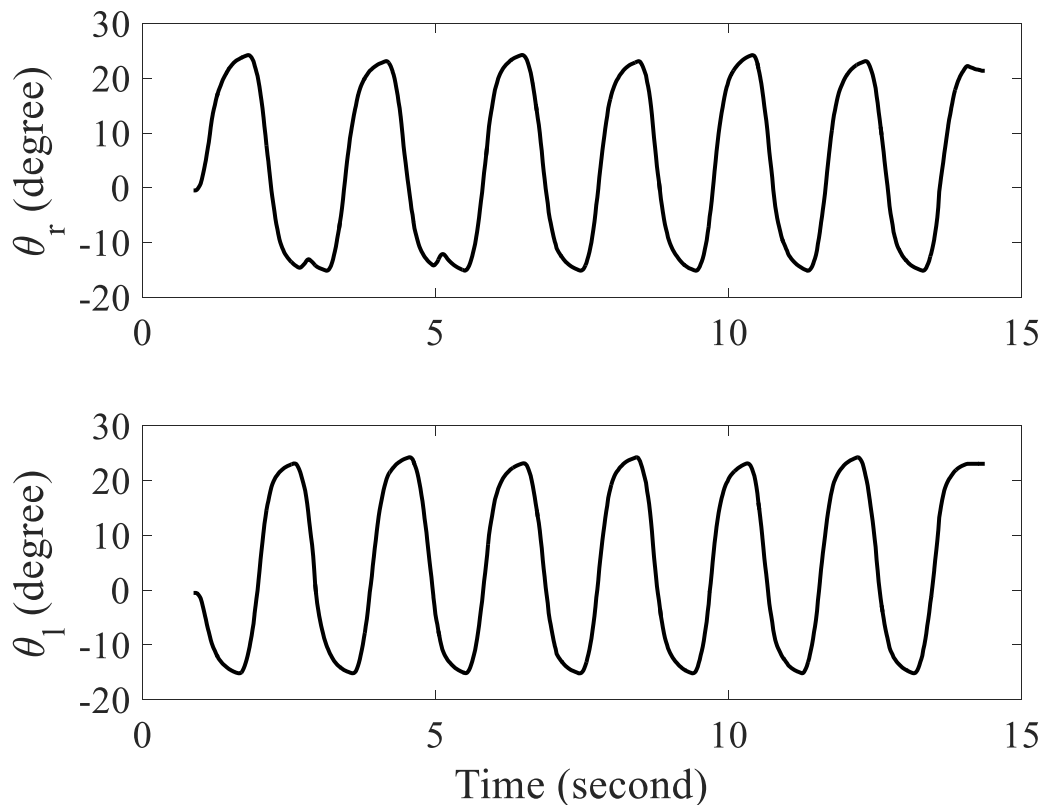

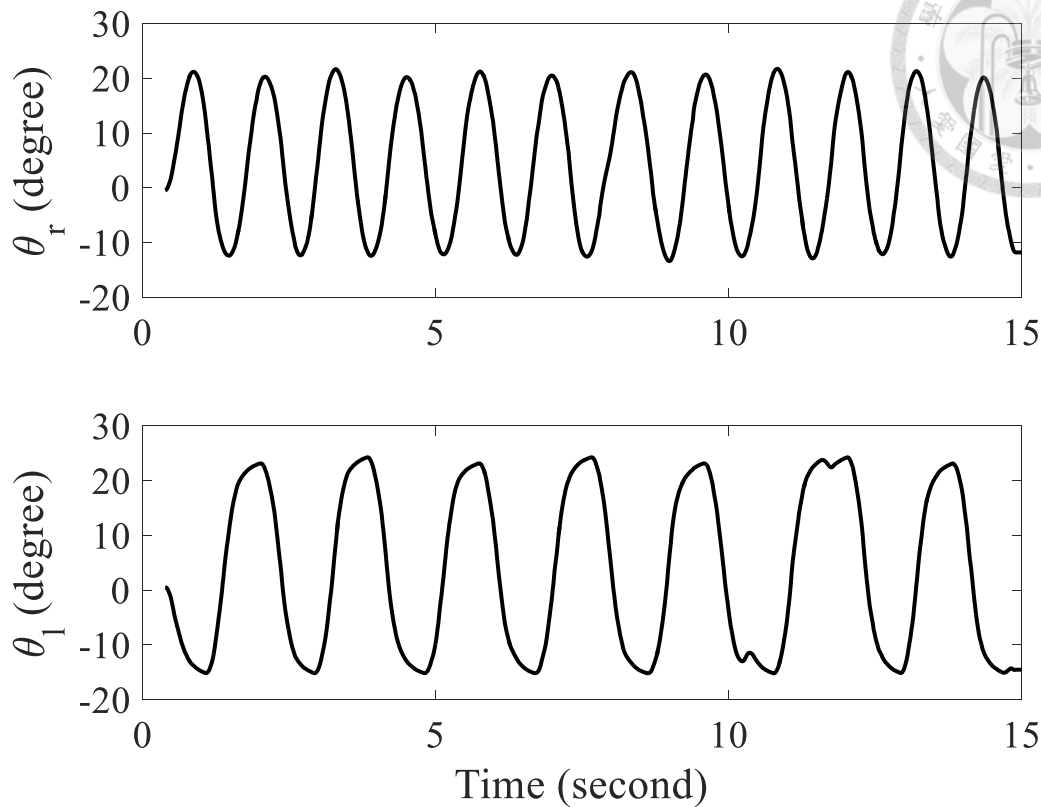Fig. 7-11 Two-leg rotation result.

67

Fig. 7-12 Speed up testing.

Considering the speed problem, there are two gait cycles distributing within 5 sec. It seems very slow, so we change the right leg program to perform faster speed. The gait cycle happens 4 times within 5 sec. We can calculate human walking speed as 0.8 Hz. We believe this frequency is fast enough for handling human walking. It happens little vibe around angle rotation limit. This vibe would cause user feel non-natural during walking. It has opportunity to fall when this vibe occurs. The reason why vibe disappears is that settling time, which is designed by control mode l, is not fast enough to handle 0.8 Hz walking speed. This result tells us that we should design new controller parameter before exoskeleton wearing.

7.5   Step response test

We focus on mode 2 to discuss system step response. Because we choose mode 2 to design speed up exoskeleton, we predict that our system can let user feel comfortable with appropriate speed control. We design new controller parameters with experimental step response. In Myrio program, we set k_p value is 1, T_I value is 1e300 and T_D value is 0 to close PID controller function. Then we use free motor, which is not loaded with exoskeleton leg, test and loading motor test with step response with twenty-five degree angle position command and minus sixteen-degree angle position command as below.
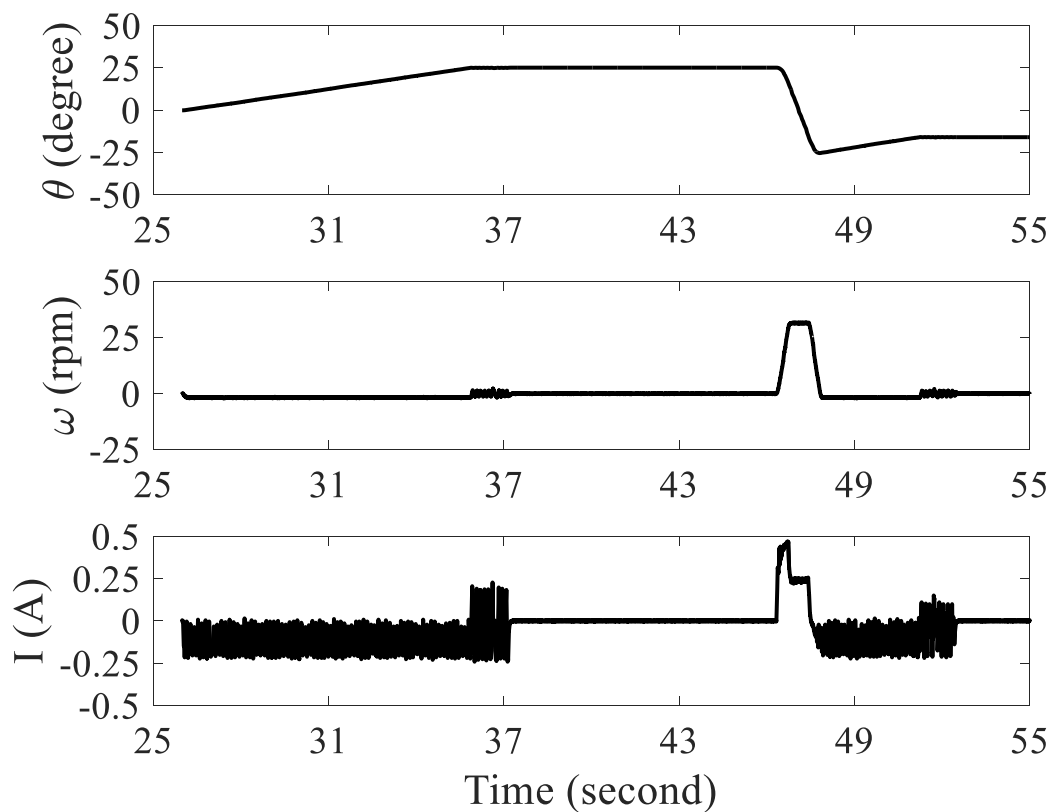

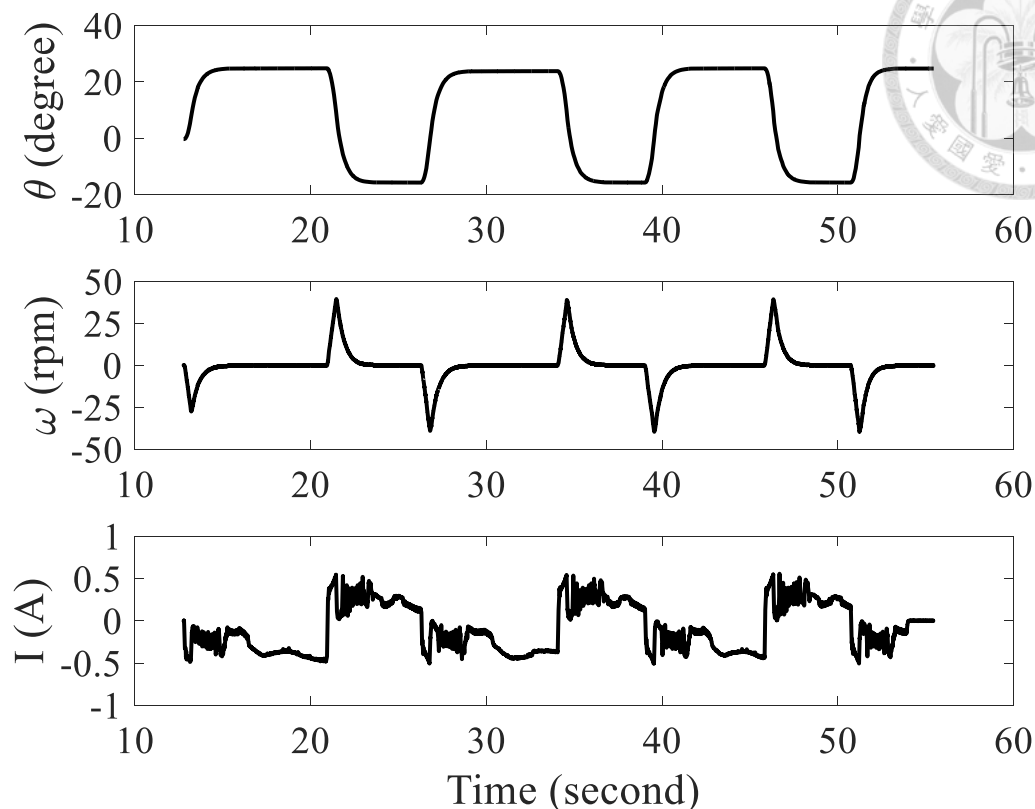Fig. 7-13 Free motor at auto walking mode.

69

Fig. 7-14 Loading test at auto walking mode.

We use step response to estimate real system model. Comparing with theoretical model so that we can know something we didn't consider such as friction and loss. From our system, we can discover that motor axis sliding and knee cylinder friction with metal slot. Because motor axis outer bearing fixed with one M3 screw, this is weak to resist big torque loading so that screw is easy to bend and causing motor sliding. This is a one reason to make friction at our system. The other reason is caused by cylinder and slot friction. Our mechanism is planer linkage on fixed bar, moving bar and knee part. Planes for these three things should parallel each other. Parallel condition is good at initially. Because motor vibration cause extra torque to bend our mechanism during driving exoskeleton, there are other direction force to put into mechanism. These forces would break parallel properties within these three things. After parallel properties broken, cylinder would not move smoothly with slot. Instead, it would produce friction

between them.

Therefore, we should estimate equivalent mechanism damper to effective system friction and loss.

$$k_t i = J\ddot{\theta} + B\dot{\theta} \tag{58}$$

After identifying system, we can get system model with friction as below:

$$G(s) = \frac{k_t}{JL} \frac{1}{s^3 + \frac{BL+JR}{JL}s^2 + \frac{BR+k_b k_t}{JL}s} \tag{59}$$

By applying Table 5-1, equation (59) becomes

$$G(z) = \frac{2.111e-4z^2 + 4.914e-4z + 6.618e-5}{z^3 - 1.659z^2 + 0.757z - 0.098} \tag{60}$$

7.6   Control strategy on wearing

After knowing damper of our plant, we should design new control parameter for wearing test. We use chapter six method design PID controller parameters as k_p value is 1, T_I value is 60 second and T_D value is 0.06 second.

We measure our exoskeleton with its encoder to compare with normal gait cycle value. Fig. 7-15 present without human rotation situation. We test exoskeleton let it rotated three gait cycles, then sorting these three gait cycle data into one cycle range. Two lines each means normal gait cycle as dash line and controller tracked average angle information, which we calculated by three gait cycle data, as solid line.
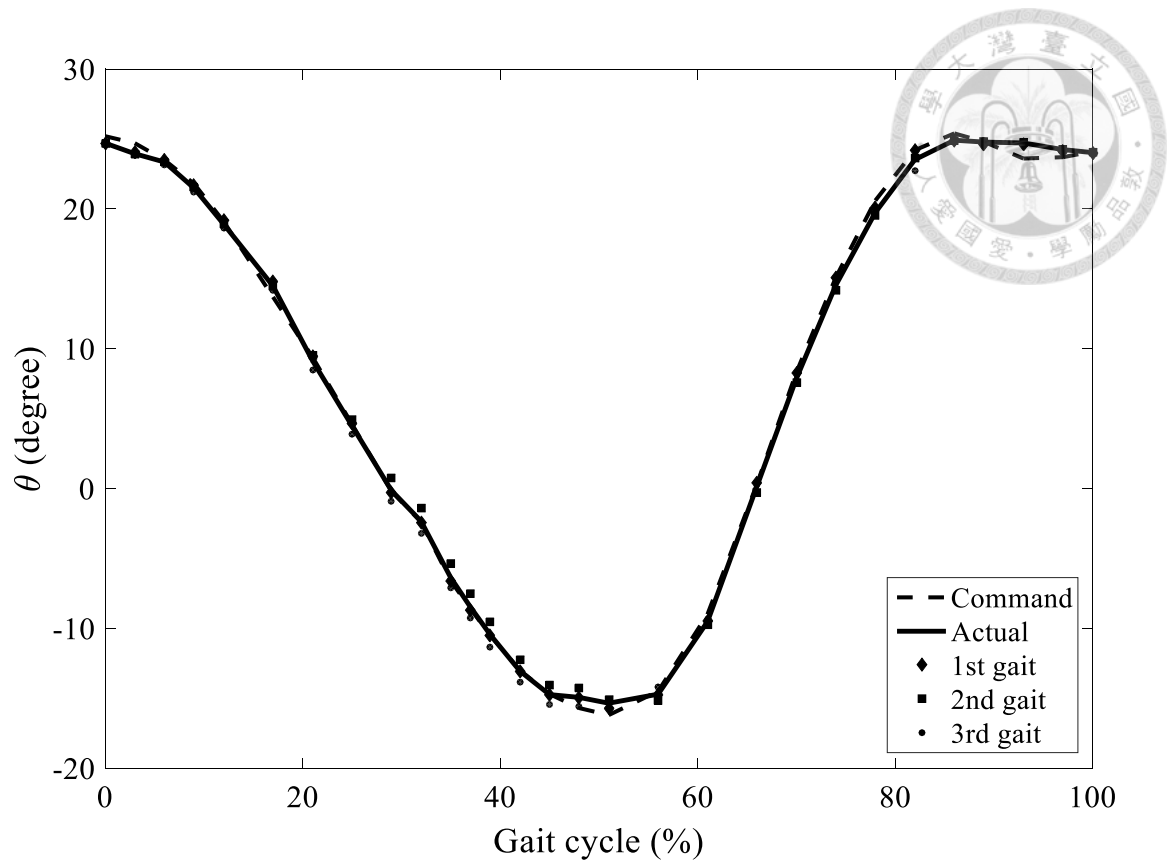
71

Fig. 7-15 Gait command tracking result.

We find that angle information is most fit to gait cycle. We compare command input gait data and encoder measured gait data, the root means square error is 0.9214. Therefore, our exoskeleton can pursuit accurate position control. Then, we can wearing it and test our exoskeleton performance.

72

Chapter 8   Wearing exoskeleton

8.1   Sorting circuit package

We add back plate package to assembly battery, controller and motor driver as Fig. 8-1. We split battery as two part. One is for controller. The other is for motor. We use 18650 battery that have 15.6 V and 8000 mAh to provide myrio power. The other is use li-po battery for motor. It provide a higher endurance and reduce some noise in sensor.
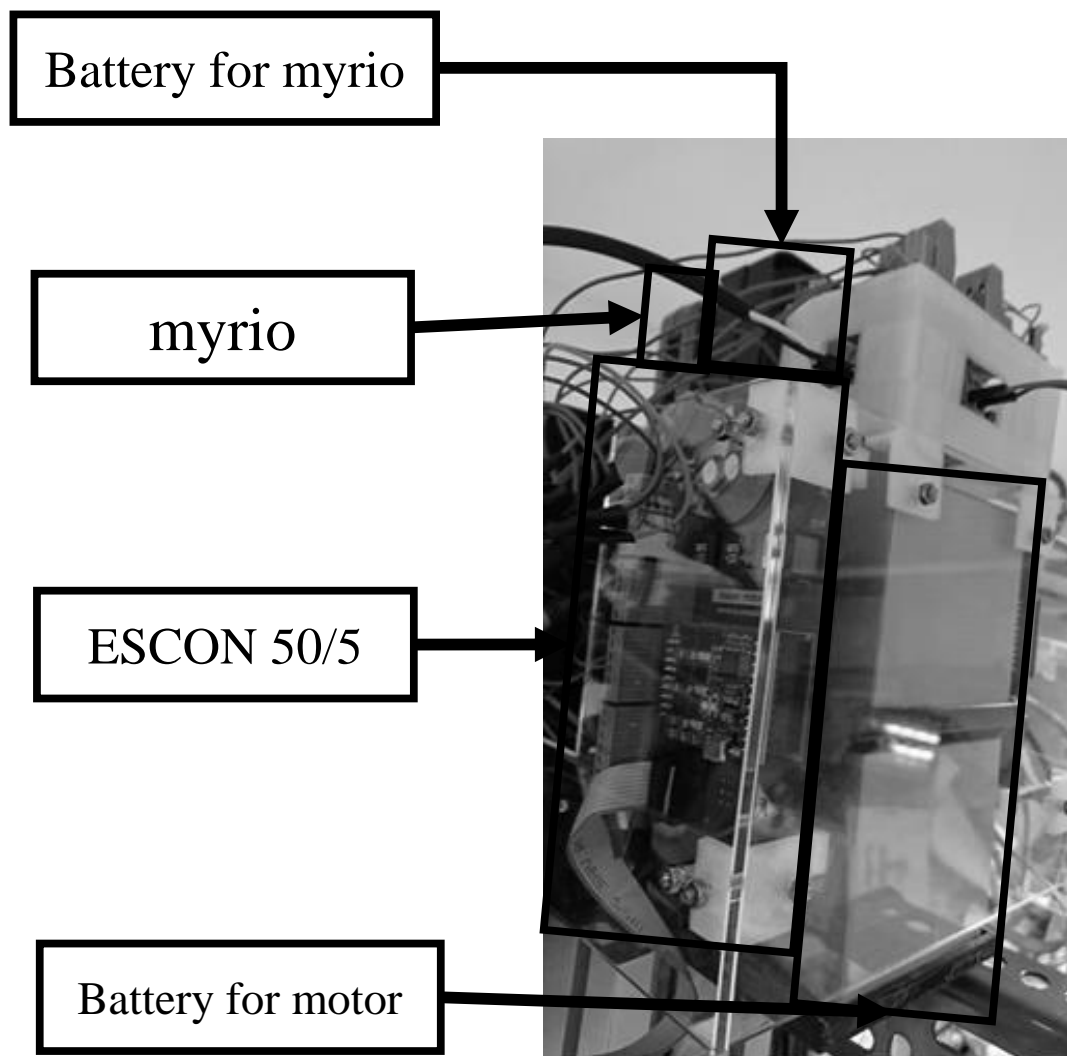

Fig. 8-1   Package at back plate.

8.2 Auto walking mode

To proof motor have ability to help human walking. We observe power, which obtain by product of driving current and driving voltage, within gait cycle as figure below. Here power is negative means current flow in different direction to let motor rotate different direction. We can discover that power would have two peaks, which happen on angle position change from upper limit to lower limit and vice versa. Peaks did not happen when angle position around limit so that we can make sure knee cylinder would not trig limit switch, which means overshoot problem would not happen during walking. In addition, motor supply enough power to support human rotate hip angle position from command max value to min value, vice versa.
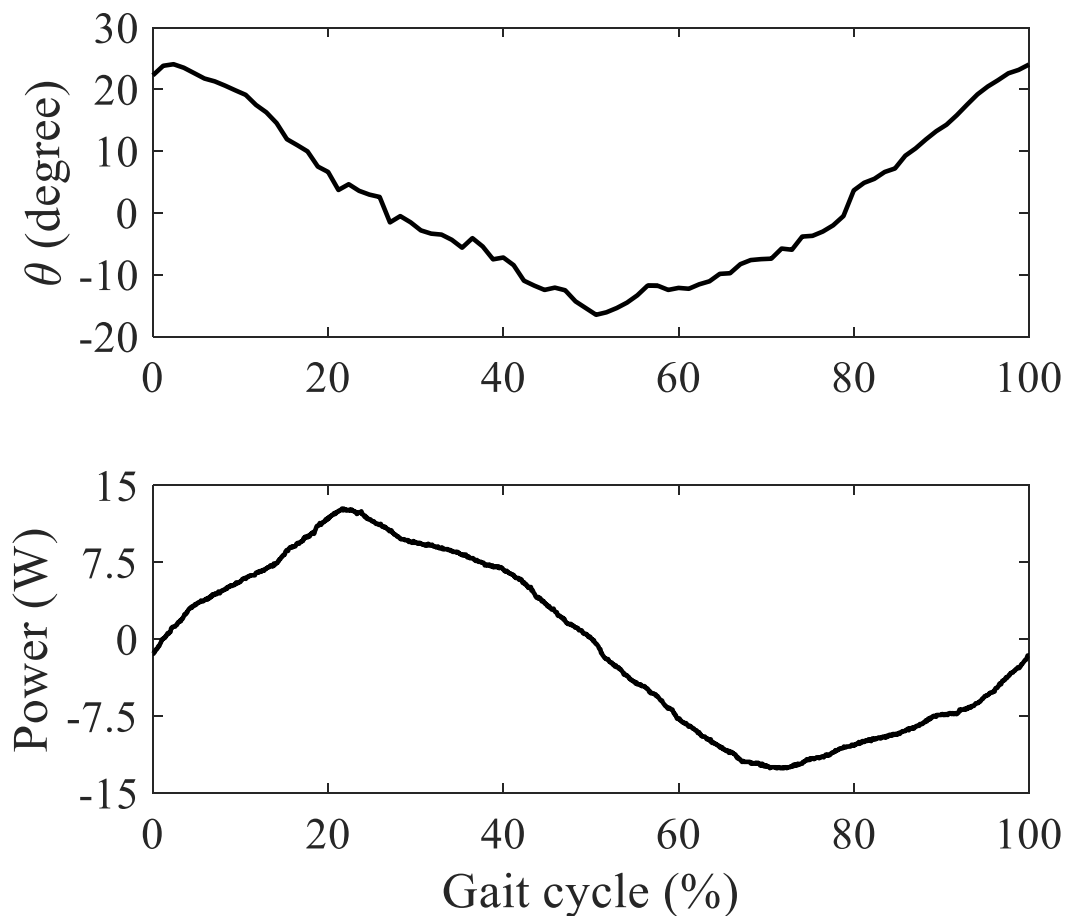

Fig. 8-2   Power consumption within gait cycle.

74

We would show result for normal human wearing exoskeleton. We use camera to capture video for human walking with exoskeleton assisting. We put three times gait cycle results for image processing. Capturing data on angle and time relation as below figure. We can observe that normal human natural walking, which is solid line result, would have higher speed than assisting with exoskeleton. With exoskeleton assisting, frequency for human walk gait cycle is 0.37Hz, which is not high enough to catch normal human walking speed, but this frequency is high enough for supporting human, whose lower limb muscle has weak ability. We would illustrate this point more clearly latter.
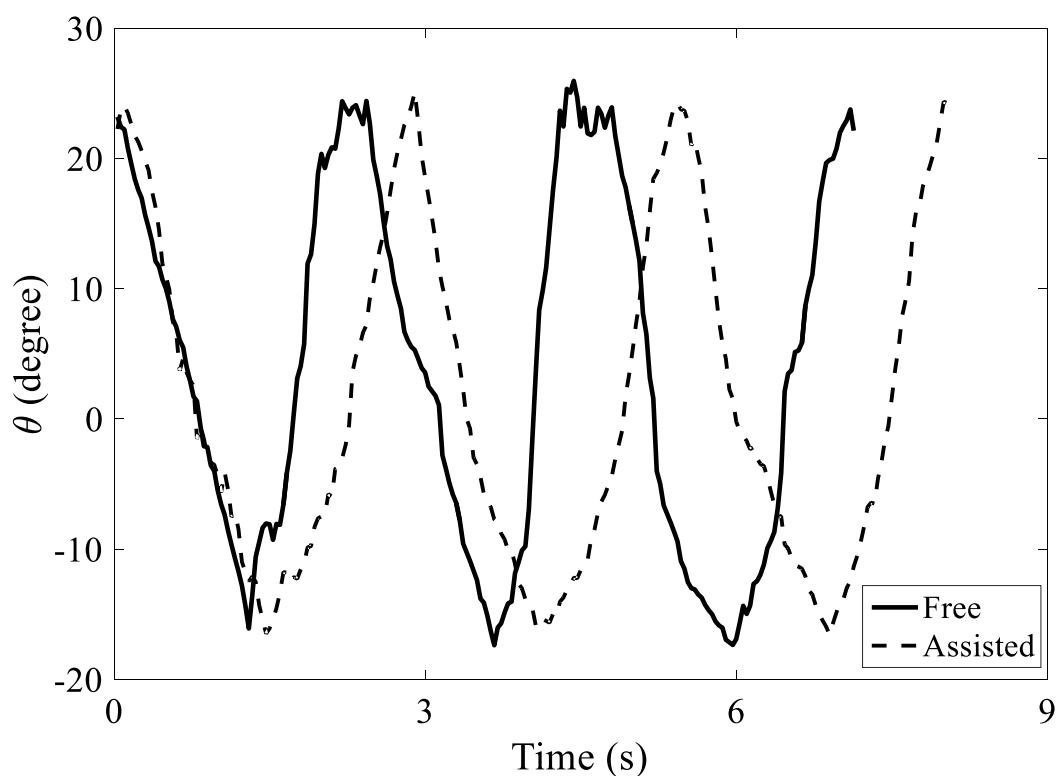

Fig. 8-3   Normal human wearing result for angle time relation.

We pick up data with each gait cycle. Putting different gait cycle data together and calculate average for these three angle rotating position data. We can get average hip rotation data, which are on free walking and assisted walking for normal human respectively.
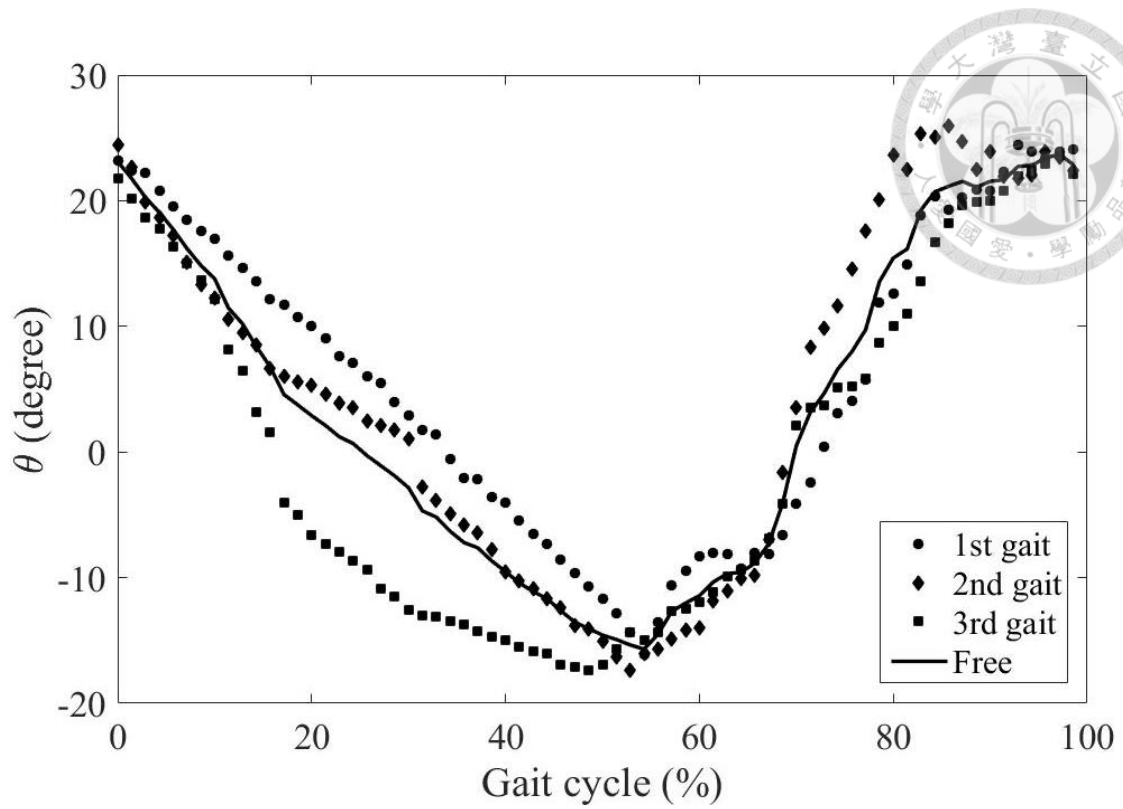
75

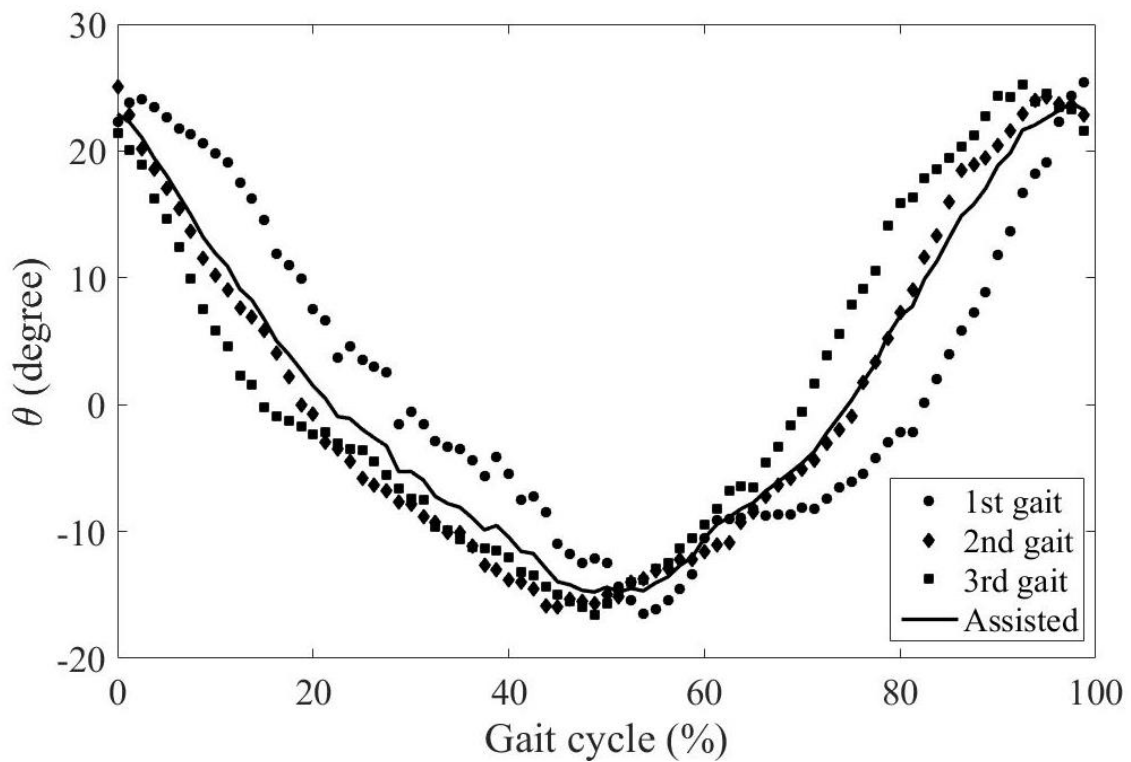Fig. 8-4   Normal human free walking gait.

Fig. 8-5   Normal human gait assisted by exoskeleton.

After getting average rotating angle data on free and assisted walking, we sort them with command as below figure. We can observe that rotating angle range would not change after assisting. With exoskeleton assisting, position control is still accurate for tracking command gait cycle. However, assisted walking would have slower speed to reach upper rotation limit at end of gait cycle than free walking. This slower speed would let normal human speed decrease than free walking.
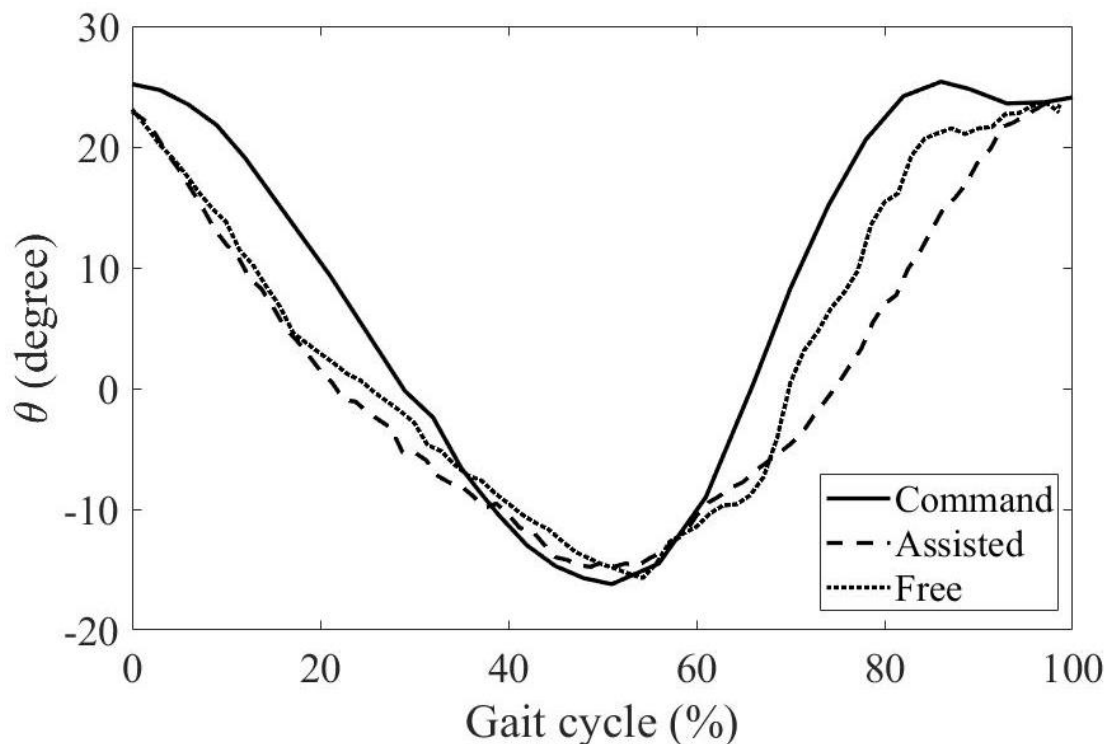
Fig. 8-6   Normal human wearing result for gait cycle representation.

We have already known that our exoskeleton have ability to assist human walk as command gait roughly. However, above testing we choose user, who has normal muscle ability. It is not enough to proof our exoskeleton has ability to assist old man or weak muscle ability human. In addition, normal human perform lower speed after assisting. Therefore, we make a wood beam barrier fixing on user leg as below figure. We define user with below figure situation as physically challenged human. Then testing exoskeleton assist effect on physically challenged human.

Fig. 8-7   Normal human with barrier.

Same as above method, we use camera to capture video for physically challenged walking with exoskeleton assisting. We put three times gait cycle results for image processing. Capturing data on angle and time relation as below figure. We can observe that first free and assisted peak would happen at same time, but assisted would lead free on second peak and latter, which means our exoskeleton can speed up physical challenge human walking unless first gait cycle. With exoskeleton assisting, frequency for human walk gait cycle is 0.39Hz. This frequency is high enough to catch general physically challenged human walking speed.
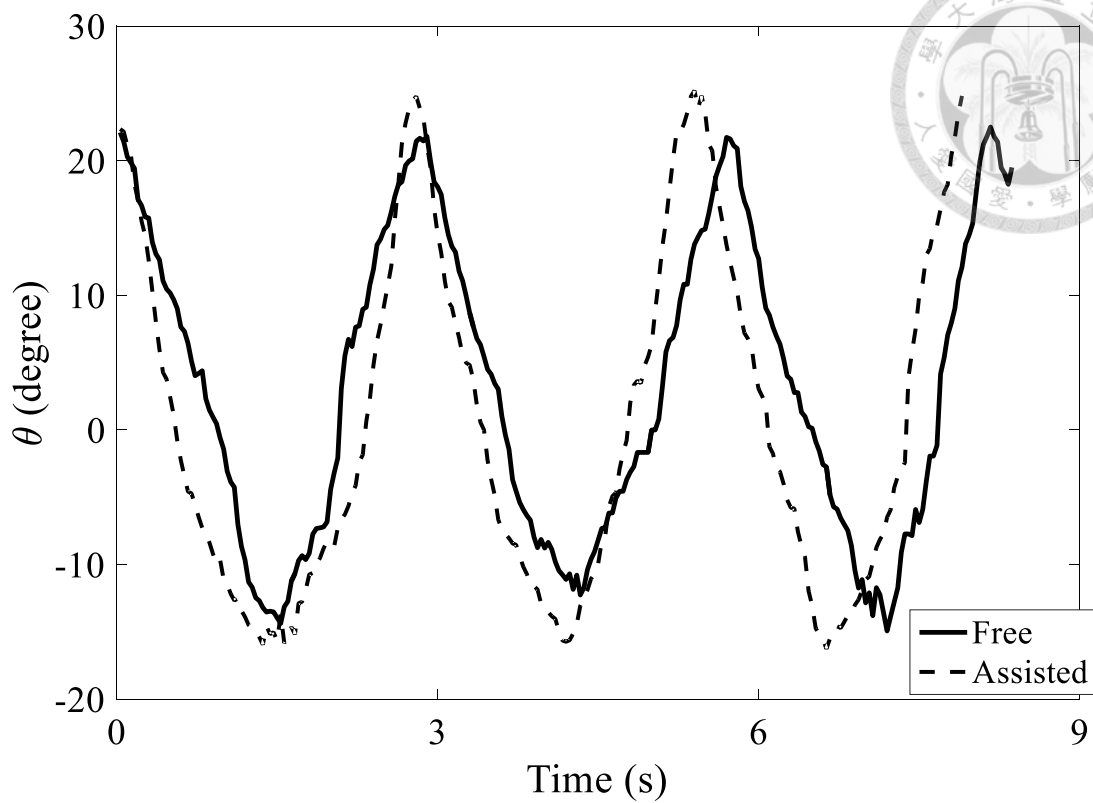
Fig. 8-8   physically challenged human wearing for angle time relation.

Again, we pick up data with each gait cycle. Putting different gait cycle data together and calculate average for these three angle rotating position data. We can get average hip rotation data, which are on free walking and assisted walking for physically challenged human respectively.

Fig. 8-9   physically challenged human free walking gait.

Fig. 8-10 physically challenged human gait assisted by exoskeleton.

80

After getting average rotating angle data on free and assisted walking, we sort them with command as below figure. We can observe tha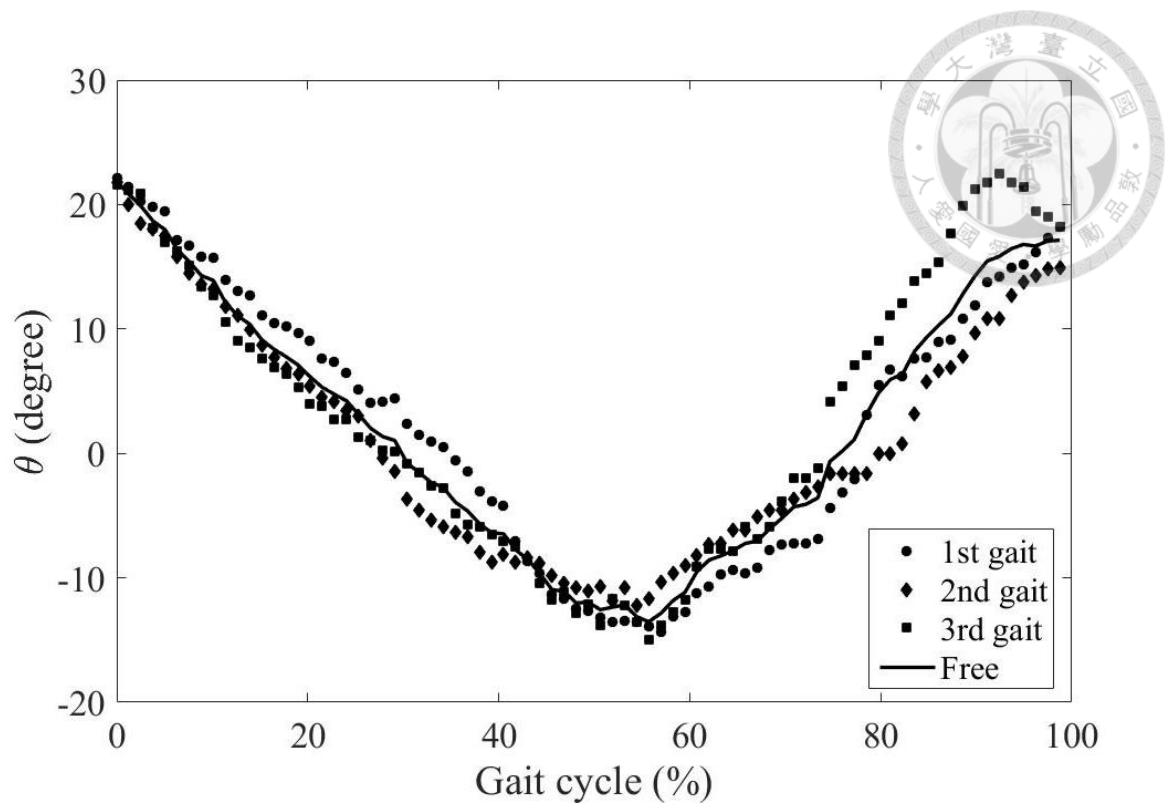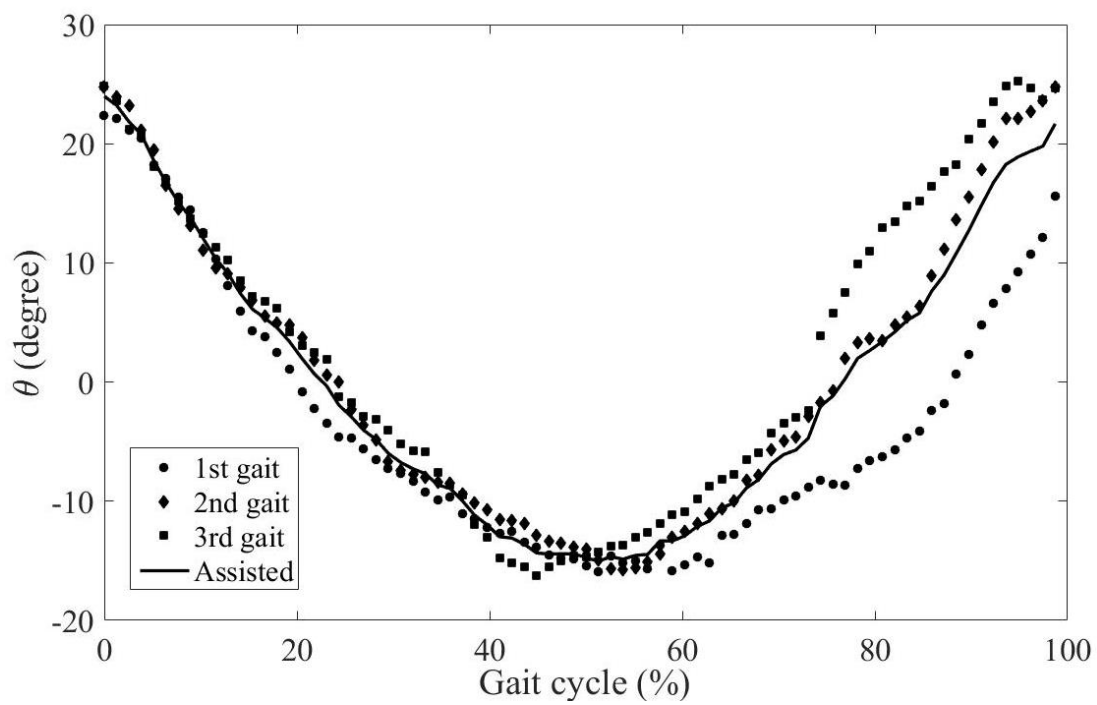t assisted rotating range would bigger than free walking, which means our exoskeleton have ability to enlarge hip rotating range for physically challenged human. This enlarge rotating range can help physically challenged human modify their gait to normal gait. In addition, we can observe that assisted rotating angle can pursuit command gait roughly as above. With exoskeleton assisting, position control is still accurate for tracking command gait cycle.
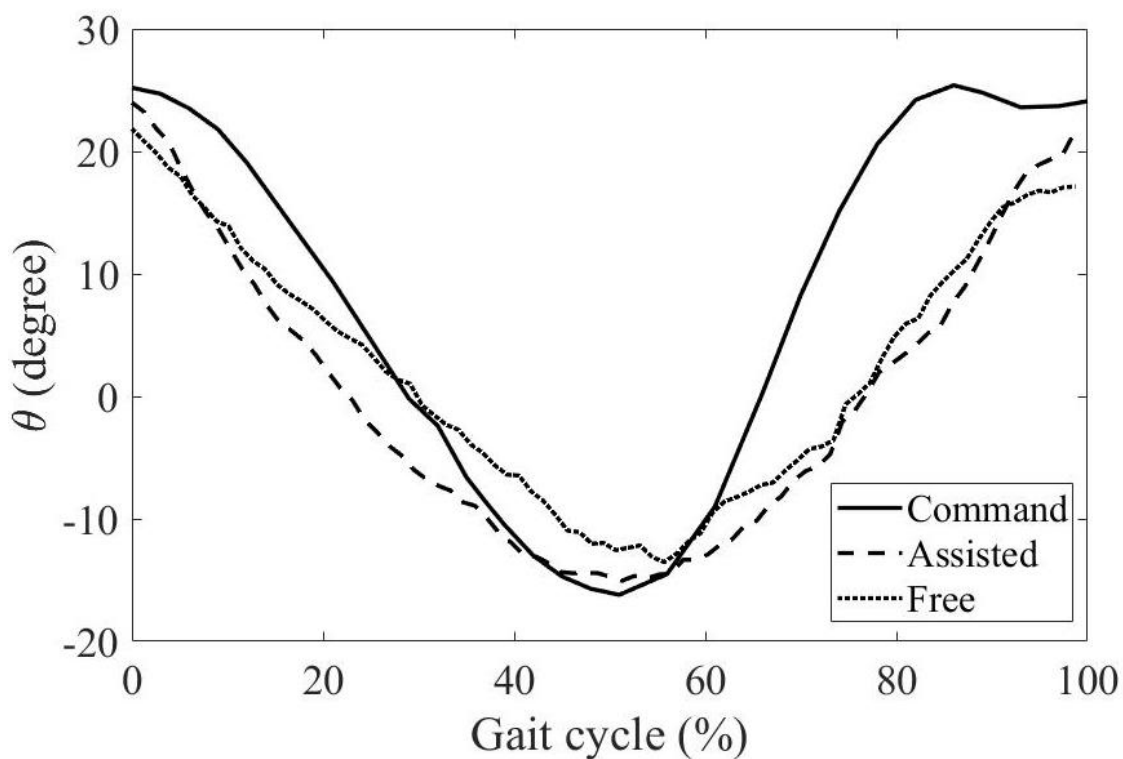
Fig. 8-11 physically challenged human wearing for gait cycle representation.

We comparing normal human free walking and physically challenged human result as below figure. Here we use solid line show normal human free walking result. Dot line and dash line is free and assisted walking on physically challenged human respectively. We can discover that assisted gait would fit normal walking more than free gait at stance phase, which is first 60% gait cycle. At swing phase, which is post 40%

81

gait cycle, assisted gait would perform higher max value than free gait, which means

rotating range enlarge would be explained again. This enlarge rotating range can help

physically challenged human modify their gait to normal gait. Sum up, physically

challenged human with our exoskeleton assisting can reach normal human free walking
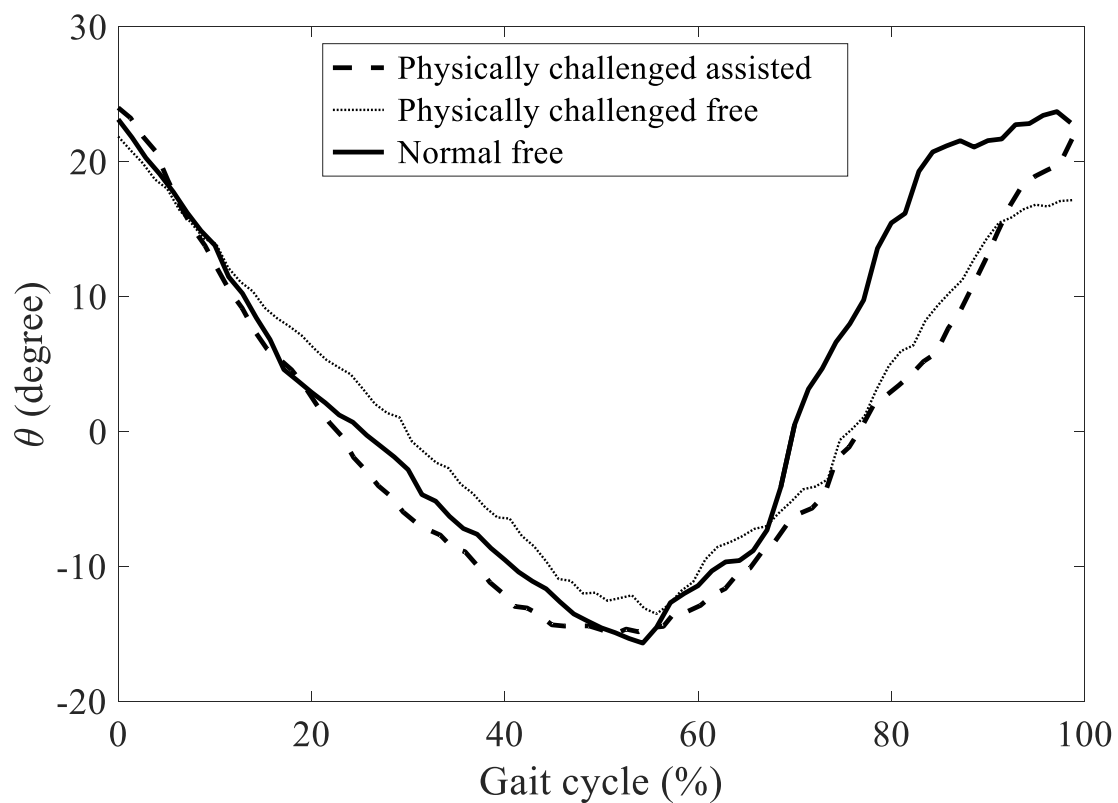
gait cycle.

Fig. 8-12 physically challenged human wearing for gait cycle comparison.

82

Chapter 9   Conclusions and future work

In this chapter, we would talk about conclusions and future work about this thesis.

9.1   Conclusions

We create a gelatin based artificial skin phantom. Phantom morphology properties is fitting to human skin such as thickness and sweat pores. In addition, mechanical properties drop in reasonable range. To calibrate EEG device with phantom assisting, we know phantom equivalent circuit model and its electronic element parameters. Also this phantom has similar impedance property with human at dry condition.

We developed a compact walking-assistive device on lower limb. We use aluminum light metal to make our mechanism structure. Structure cover human body from hip to knee, which is so called exoskeleton. Our exoskeleton design hip part two axis crosslinking to pelvic joint. This design would let user feel fit able. We design fall prevention mechanism by four bar linkage and knee part cylinder slot.

Motor we choose BLDC with gearbox to make sure high position accuracy and enough torque supply. For safety consideration, we set limit switch at the boundary of slot. We use hall sensor to determine standing phase angle as zero calibration point. We discuss three kinds of control model based on servo amplifier different mode respectively. We derive theory, design corresponding PID position controller parameters and testing control effect without human for three models.

We finally choose servo amplifier as PI closed loop speed controller (i.e. mode 2) to implement wearing control system. For follow human walking speed, we speed up system response. Then we discover vibe problem due to slow settling time. We consider step response for our system to estimate friction term. After knowing friction, we design new control parameter to test position accuracy. We get command and actual value root

83

means square error is 0.9214, which imply position control is good operating. Then we do wearing test. With exoskeleton helping, physically challenged human perform better gait data as normal human free walking and walking speed can reach 0.39 times gait per sec.

We can simply to say, our exoskeleton is ready to use.

9.2   Future work

There are many develop directions can view as future work.

We have already known that SU-8 thin film is brittle. If we want to simulate head phantom with EEG device, our phantom would break while bending. We should deal this problem at future work. For simulating human sweating condition, this phantom should add artificial cell part to handle absorbing water part so that impedance would be similar with human skin wet condition.

For plant moment of inertia, we can add human thigh moment of inertia to pursuit more accurate control system. Mechanism would probably have different resist torque for different angle. Therefore, we can estimate effective moment of inertia as function of rotated angle. In addition, we can estimate moment of inertia as function of rotated angle on thigh so that position control can more accurate during wearing.

In mechanism part, we should modify friction problem as section 7.5 said. For motor axis sliding, we should design new coupling to fix axis with multidirectional force. For knee cylinder friction with metal slot, we should change C buckle fixing way. To assist human better, we should new design knee-ankle-foot part exoskeleton. Therefore, exoskeleton can assist human lower limb completely.

In control part, we can derive state space formulation to optimize control model. In

84

advanced, we can develop to robust control. By gathering large wearing experience, we can use machine learning to know using habits. Construct these habits as fuzzy logic rule base. Control system can auto select correspond mode to user. We can combine mode 3 function with force sensor by sensing user muscle force, then establishing a muscle training system.

REFERENCE
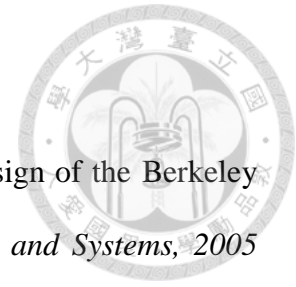
[1] A Zoss, H Kazerooni, and A Chu 2005 On the mechanical design of the Berkeley lower extremity exoskeleton (BLEEX). In: *Intelligent Robots and Systems, 2005 IEEE/RSJ International Conference*, pp 3132-9.

[2] Thomas J Collier, David B Kynor, Jerry Bieszczad, William E Audette, Erik J Kobylarz and Solomon Gilbert Diamond 2012 Creation of a human head phantom for testing of electroencephalography equipment and techniques *IEEE Trans. Biomed. Eng.* **59** 2628-34.

[3] Dabrowska A K, Rotaru G M, Derler S, Spano F, Camenzind M, Annaheim S, Stampfli R, Schmid M and Rossi R M 2016 Materials used to simulate physical properties of human skin *Skin Res. Technol.* **22** 3-14.

[4] Grosse Perdekamp M, Pollak S, Thierauf A, Strassburger E, Hunzinger M and Vennemann B 2009 Experimental simulation of reentry shots using a skin-gelatine composite model *Int. J. Legal Med.* **123** 419-25.

[5] Gabriel C 2007 Tissue equivalent material for hand phantoms *Phys. Med. Biol.* **52** 4205-10.

[6] http://www.robaid.com/bionics/cyberdyne-hal-5-exoskeleton-robot/

[7] Yi Long, Zhijiang Du, Lin Cong, Weidong Wang, Zhiming Zhang and Wei Dong 2017 Active disturbance rejection control based human gait tracking for lower extremity rehabilitation exoskeleton *ISA Trans.* **67** 389-97.

[8] Gabriel Aguirre Ollinger, Umashankar Nagarajan and Ambarish Goswami 2016 An admittance shaping controller for exoskeleton assistance of the lower extremities *Auton. Robot* **40** 701-28.

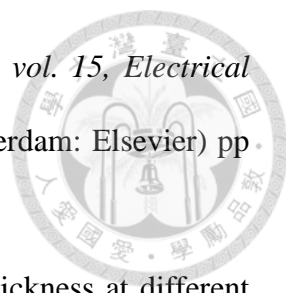[9] Umashankar Nagarajan, Gabriel Aguirre Ollinger and Ambarish Goswami 2016

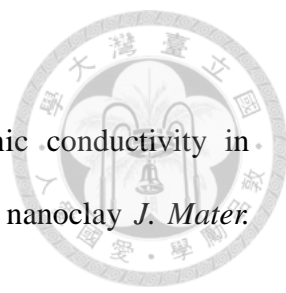Integral admittance shaping: A unified framework for active exoskeleton control *Robot. Auton. Syst.* **75** 310-24.
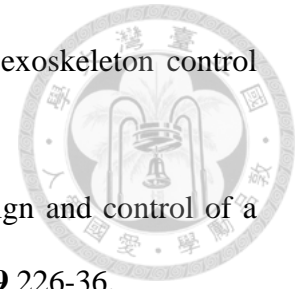
[10] Lin Liu, Steffen Leonhardt and Berno J E Misgeld 2016 Design and control of a mechanical rotary variable impedance actuator *Mechatronics* **39** 226-36.

[11] Gong Chen, Peng Qi, Zhao Guo and Haoyong Yu 2016 Mechanical design and evaluation of a compact portable knee–ankle–foot robot for gait rehabilitation *Mech. Mach. Theory* **103** 51-64.

[12] Sehoon Oh, Eunyoung Baek, Seok-ki Song, Samer Mohammed, Doyoung Jeon and Kyoungchul Kong 2015 A generalized control framework of assistive controllers and its application to lower limb exoskeletons *Robot. Auton. Syst.* **73** 68-77.

[13] B Achili, T Madani, B Daachi and K Djouani 2016 Adaptive observer based on MLPNN and sliding mode for wearable robots: Application to an active joint orthosis *Neurocomputing* **197** 69–77.

[14] Francesco Giovacchini, Federica Vannetti, Matteo Fantozzi, Marco Cempinia, Mario Cortese, Andrea Parri, Tingfang Yan, Dirk Lefeber and Nicola Vitiello 2015 A light-weight active orthosis for hip movement assistance *Robot. Auton. Syst.* **73** 123–34.

[15] Alan T Asbeck, Kai Schmidt and Conor J Walsh 2015 Soft exosuit for hip assistance *Robot. Auton. Syst.* **73** 102–10.

[16] Xiaoping Ouyang, Shuo Ding, Boqian Fan, Perry Y Li and Huayong Yang 2016 Development of a novel compact hydraulic power unit for the exoskeleton robot *Mechatronics* **38** 68–75.

[17] Jessica C Selinger and J Maxwell Donelan 2016 Myoelectric control for adaptable biomechanical energy harvesting *IEEE Trans. Neural Syst. Rehabil. Eng.* **24**

364-73.

[18] Shahid Hussain, Prashant K Jamwal, Mergen H Ghayesh and Sheng Q Xie 2017 Assist-as-needed control of an intrinsically compliant robotic gait training orthosis *IEEE Trans. Ind. Electron.* **64** 1675-85.

[19] Tristan Vouga, Katie Z Zhuang, Jeremy Olivier, Mikhail A Lebedev, Miguel A L Nicolelis, Mohamed Bouri and Hannes Bleuler 2017 EXiO—A Brain-Controlled Lower Limb Exoskeleton for Rhesus Macaques *IEEE Trans. Neural Syst. Rehabil. Eng.* **25** 131-40.

[20] Chao Zhang, Gangfeng Liu, Changle Li, Jie Zhao, Hongying Yu and Yanhe Zhu 2016 Development of a lower limb rehabilitation exoskeleton based on real-time gait detection and gait tracking *Adv. Mech. Eng.* **8(1)** 1–9.

[21] Xinglai Jin, Shiqiang Zhu, Xiaocong Zhu, Qingcheng Chen and Xuequn Zhang 2017 Single-input adaptive fuzzy sliding mode control of the lower extremity exoskeleton based on human–robot interaction *Adv. Mech. Eng.* **9(2)** 1–9.

[22] Shiqiang Zhu, Xinglai Jin, Bin Yao, Qingcheng Chen, Xiang Pei and Zhongqiang Pan 2016 Non-linear sliding mode control of the lower extremity exoskeleton based on human–robot cooperation *Int. J. Adv. Robot. Syst.* **13** 1-10.

[23] Yi Long, Zhi-jiang Du, Weidong Wang and Wei Dong 2016 Development of a wearable exoskeleton rehabilitation system based on hybrid control mode *Int. J. Adv. Robot. Syst.* **13** 1-10.

[24] Jun Zhu, Yu Wang, Jinlin Jiang, Bo Sun and Heng Cao 2017 Unidirectional variable stiffness hydraulic actuator for load-carrying knee exoskeleton *Int. J. Adv. Robot. Syst.* **14** 1-12.

[25] Grimnes S and Martinsen Ø G 2008 *Bioimpedance and Bioelectricity Basics*, 2nd ed (New York: Academic Press) pp 93-137.

[26] B A Simpson 2003 *Pain Research and Clinical Management, vol. 15, Electrical Stimulation and the Relief of pain*, 1st ed. B A Simpson (Amsterdam: Elsevier) pp 17-36.

[27] Sandby-Moller J, Poulsen T and Wulf H C 2003 Epidermal thickness at different body sites: relationship to age, gender, pigmentation, blood content, skin type and smoking habits *Acta Derm. Venereol.* **83** 410-3.

[28] Agache P G, Monneur C, Leveque J L and De Rigal J 1980 Mechanical properties and Young's modulus of human skin in vivo *Arch. Dermatol. Res*., **269** 221-32.

[29] Manschot J F and Brakkee A J 1986 The measurement and modelling of the mechanical properties of human skin in vivo - II. The model *J. Biomech.* **19** 517-21.

[30] Diridollou S, Patat F, Gens F, Vaillant L, Black D, Lagarde J M, Gall Y and Berson M 2000 In vivo model of the mechanical properties of the human skin under suction *Skin Res. Technol.* **6** 214-21.

[31] Wilke K, Martin A, Terstegen L and Biel S S 2007 A short history of sweat gland biology *Int. J. Cosmetic Sci.* **29** 169-79.

[32] Zhang Y, Zhang X, Fang J, Jiang S, Zhang Y, Gu D, Nelson R D and LaRue J C 2010 Application of SU-8 as the insulator toward a novel planar microelectrode array for extracellular neural recording. In: *Nano/Micro Engineered and Molecular Systems (NEMS), 2010 5th IEEE International Conference*, pp 395-8.

[33] http://www.microchem.com.

[34] Vieira D F, Avellaneda C O and Pawlicka A 2007 Conductivity study of a gelatin-based polymer electrolyte *Electrochimica Acta* **53** 1404-8.

[35] Landi G, Sorrentino A, Iannace S and Neitzert H C 2015 Electrical Characterization and Modeling of a Gelatin/Graphene System *Adv. Cond. Matter.*

Phys. **2015** 5.

[36] Ghadami A, Taheri Qazvini N and Nikfarjam N 2014 Ionic conductivity in gelatin-based hybrid solid electrolytes: The non-trivial role of nanoclay *J. Mater. Sci. Technol.* **30** 1096-102.

[37] Yen-An Chen 2016 Development of a gelatin-based artificial skin phantom for electrical treatments M.S. thesis, Dept. Mech. Eng., National Taiwan Univ., Taiwan.

[38] Nwe N, Furuike T and Tamura H 2010 Selection of a biopolymer based on attachment, morphology and proliferation of fibroblast NIH/3T3 cells for the development of a biodegradable tissue regeneration template: Alginate, bacterial cellulose and gelatin *Proc. Biochem.* **45** 457-66.

[39] Allenby A C, Fletcher J, Schock C and Tees T F S 1969 The effect of heat, pH and organic solvents on the electrical impedance and permeability of excesed human skin *Brit. J. Dermatol.* **81** 31-9.

[40] Dorgan S J and Reilly R B 1999 A model for human skin impedance during surface functional neuromuscular stimulation *IEEE Trans. Rehabil. Eng.* **7** 341-8.

[41] Heng-Chia Hsu 2015 Design of walking assistive device on lower limb with fall preventing mechanism M.S. thesis, Dept. Mech. Eng., National Taiwan Univ., Taiwan.

[42] http://www.maxonmotor.ch/maxon/view/content/index.

[43] http://sine.ni.com/nips/cds/view/p/lang/zht/nid/211694.

[44] Charles L Phillips and H Troy Nagle 1998 *Digital control system analysis and design*, 3rd ed (New Jersey: Pearson Education) pp 27-88.

[45] Gabriele Bovi, Marco Rabuffetti, Paolo Mazzoleni and Maurizio Ferrarin 2011 A multiple-task gait analysis approach: Kinematic, kinetic and EMG reference data

for healthy young and adult subjects *Gait Posture* **33** 6–13.

[46] M Shahrokhi and A Zmorrodi Comparison of PID controller tuning methods

[47] Shao-An Tung 2016 Integration of control system strategy for a powered wheelchair driven by rim motors M.S. thesis, Dept. Mech. Eng., National Taiwan Univ., Taiwan.
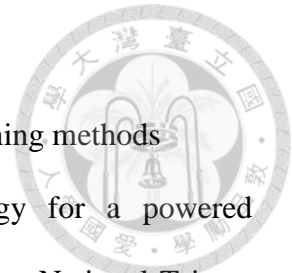
APPENDIX

1.1 Literature review on brain computer interface

1.2 EEG detection

1.3 EEG test

1.4 Brain wave results and discussions

1.5 Brain controlled system

1.6 Brain controlled method

1.7 Status determination of EEG